FACULDADE DE ENGENHARIA DA UNIVERSIDADE DO PORTO

Distributed batteryless end-node sensing device for realworld long life applications

Leonor Carneiro Pinto Branco Carvalho

Mestrado em Engenharia Eletrotécnica e de Computadores

Supervisor: Prof. Vítor Manuel Grade Tavares

November 5, 2025

© Leonor Carneiro Pinto Branco Carvalho, 2024

Resumo

Esta dissertação aborda os impactos ambientais e os desafios de manutenção associados ao uso de baterias descartáveis em dispositivos da Internet das Coisas (IoT). Como alternativa, propõe-se o desenvolvimento de um dispositivo de monitorização totalmente autónomo em termos energéticos e sem qualquer recurso a baterias, concebido para funcionamento em ambientes interiores através da colheita de energia do meio envolvente.

Foram avaliadas diferentes fontes de energia ambiental, nomeadamente solar, térmica, cinética e radiofrequência (RF). Entre estas, a energia solar através de painéis de silício amorfo demonstrou maior consistência sob iluminação interior, sendo integrada com supercondensadores e um circuito de gestão de energia de elevada eficiência, assegurando fornecimento energético suficiente mesmo durante períodos de luminosidade reduzida.

No que respeita ao processamento, compararam-se duas plataformas distintas. A placa Riotee revelou-se pouco adequada para ambientes interiores devido ao seu consumo contínuo, enquanto o *System-on-Chip* IN100 NanoBeacon, combinado com um temporizador externo, apresentou um consumo energético bastante reduzido o que permitiu ciclos de funcionamento regulares mesmo com capacidades de armazenamento bastante limitadas.

O protótipo final consiste num nó modular, uma solução de colheita de energia, processamento de ultrabaixo consumo e sensor ambiental de temperatura e humidade, incluindo ainda um sistema de comutação de antena para flexibilidade de utilização. Testes extensivos em ambiente real validaram a fiabilidade da operação e permitiram definir as melhores configurações de transmissão e de instalação.

Os resultados demonstram que este nó é capaz de funcionar de forma previsível e estável, atingindo taxas de sucesso superiores a 99% mesmo em períodos de escuridão prolongada. Esta contribuição evidencia o potencial de dispositivos IoT sustentáveis e sem manutenção, relevantes para aplicações em infraestruturas inteligentes, saúde e monitorização ambiental.

Abstract

This dissertation examines the environmental impacts and maintenance challenges associated with disposable batteries in Internet of Things (IoT) devices. As an alternative, it proposes the development of a fully energy-autonomous monitoring device, designed for indoor environments and operating without batteries by relying exclusively on ambient energy harvesting.

Several ambient energy sources were evaluated, namely solar, thermal, kinetic, and radiofrequency (RF). Among these, solar energy using amorphous silicon panels proved to be the most consistent under indoor lighting conditions. This solution was integrated with supercapacitors and a high-efficiency energy management circuit, ensuring reliable power supply even during extended periods of reduced illumination.

For processing, two platforms were compared. The Riotee board was found unsuitable for indoor environments due to its continuous consumption, whereas the IN100 NanoBeacon System-on-Chip, combined with an external timer, demonstrated extremely low energy usage, enabling regular operation cycles even with limited storage capacity.

The final prototype consists of a modular node that integrates indoor energy harvesting, ultra-low-power processing, and a temperature and humidity environmental sensor. It also incorporates an antenna-switching system for increased flexibility. Extensive real-world testing validated the system's reliability and guided the selection of optimal transmission and deployment configurations.

The results demonstrate that this node can operate predictably and stably, achieving success rates above 99% even during prolonged periods of darkness. This work highlights the potential of sustainable, maintenance-free IoT devices for applications in smart infrastructures, healthcare, and environmental monitoring.

UN Sustainable Development Goals

The Sustainable Development Goals (SDGs) of the United Nations provide a global framework to pursue a better and more sustainable future at all levels [43]. These 17 interconnected goals address critical challenges related to energy sustainability, climate change, innovation, environmental degradation, and more. This dissertation is associated with specific SDGs, demonstrating how batteryless Internet of Things (IoT) technology is capable of contributing to sustainable development by making innovative energy solutions, utilizing resources efficiently, and enduring environmental resilience in the long term.

Batteryless IoT devices, which use energy harvested from ambient sources such as solar, thermal, kinetic, and radio frequency (RF)[13, 17], do not need a conventional battery. This facilitates the development of scalable, long-lasting and environmentally friendly sensing networks, directly contributing to the following SDGs:

SDG 7 Ensure access to affordable, reliable, sustainable and modern energy for all [43].

SDG 8 Promote sustained, inclusive, and sustainable economic growth, full and productive employment and decent work for all [43].

SDG 9 Build resilient infrastructure, promote inclusive and sustainable industrialization and foster innovation [43].

SDG 12 Ensure sustainable consumption and production patterns [43].

This dissertation aligns with all the SDGs mentioned in Table 1, contributing to a more sustainable and innovative future. The proposed batteryless IoT devices represent very practical solutions to reduce environmental impact, improve energy efficiency, and promote economic growth. Applications in health care, environmental monitoring, and infrastructure show their transformative potential in diverse industries, supporting global efforts toward sustainability and resilience [43].

Table 1: Contribution of Batteryless IoT Devices to UN Sustainable Development Goals.

SDG	**Target**	**Contribution**	**Performance Indicators and Metrics**
7	7.1	Development of batteryless IoT devices powered by energy harvesting supports access to clean and reliable energy, ensuring efficient use of available resources even in remote and underserved areas [2].	Percentage of IoT devices deployed that can operate without disposable batteries in remote locations.
	7.2	Integration of supercapacitors and advanced energy management techniques improves the efficiency and reliability of renewable energy-powered IoT systems [13].	Increase in renewable energy efficiency with advanced IoT infrastructure.
	7.a	Advancing research in batteryless IoT enables the development of innovative solutions for energy storage management, reducing reliance on disposable chemical batteries and minimizing electronic waste [17].	Reduction in battery waste and number of devices deployed with long-lasting storage solutions.
8	8.1	Batteryless IoT promotes innovation and sustainability in economic activities by enabling low-maintenance and cost-effective sensing systems [19].	Adoption of batteryless devices in industrial and environmental monitoring deployments.
	8.4	Encourages resource efficiency by leveraging intermittent and ultra-low-power operation in IoT systems, reducing energy waste and maintenance costs [18].	Number of systems implemented with batteryless IoT to reduce operational waste and expense.
9	9.4	Supports sustainable and resilient IoT infrastructure development through energy harvesting and reduced maintenance requirements [17].	Number of IoT networks deployed with batteryless end-nodes in infrastructure monitoring.
	9.5	Demonstrates innovative applications by exploring advanced energy-harvesting and management techniques for IoT systems [19].	Research outputs and technology demonstrations in batteryless IoT.
12	12.4	Reduces environmental impact by avoiding disposable batteries in IoT devices, lowering the associated electronic waste [18].	Reduction in the rate of battery disposal across IoT deployments.
	12.5	Promotes sustainable production practices by replacing disposable batteries with reusable, long-lasting energy storage systems [13].	Reduction in the manufacturing and usage of disposable batteries.

Acknowledgements

I would like to express my sincere gratitude to my supervisor, Professor Vítor Grade Tavares, for his continuous support, valuable guidance, and encouragement throughout the development of this dissertation.

A special thank you to Miguel Roque and Diogo Gonçalves, both from Fraunhofer Portugal, for their crucial role in this work. Miguel provided insightful advice and technical direction as my advisor, while Diogo's development of the LIGHTED testbed formed the foundation for this project. I am especially thankful for his close follow-up and support during the entire process.

I would also like to extend my appreciation to all my colleagues at Fraunhofer Portugal for the stimulating environment, collaboration, and shared experiences during this journey.

Finally, I am deeply grateful to my family and friends for their unwavering support, patience, and encouragement in every moment. This achievement would not have been possible without them.

Leonor Carvalho

Contents

1 Introduction **1**
- 1.1 Context and Topic of the Work . . . 2
- 1.2 Motivation and Relevance . . . 3
- 1.3 Problem Statement and Challenges . . . 4
- 1.4 Objectives . . . 4
- 1.5 Contributions . . . 5
- 1.6 Structure of the Dissertation . . . 6

2 Background and State of the Art **7**
- 2.1 Introduction to Batteryless IoT Systems . . . 7
- 2.2 Energy Harvesting Techniques for Batterryless Systems . . . 8
  - 2.2.1 Solar Energy . . . 9
  - 2.2.2 Thermal Energy . . . 9
  - 2.2.3 Kinetic Energy . . . 10
  - 2.2.4 Radio Frequency Energy . . . 11
  - 2.2.5 Hybrid Energy Harvesting Systems . . . 12
- 2.3 Energy Storage and Regulation . . . 14
- 2.4 Architectures for Intermittent Power Systems . . . 15
  - 2.4.1 Checkpointing and State Preservation . . . 15
  - 2.4.2 Task Scheduling and Energy Awareness . . . 15
  - 2.4.3 Fault Tolerance Mechanisms . . . 15
  - 2.4.4 Integrated Hybrid Architectures . . . 16
- 2.5 Benchmarking Methodologies for Batteryless Systems . . . 16
- 2.6 Applications of Batteryless IoT Systems . . . 16
- 2.7 Sustainability and Environmental Impact . . . 17
- 2.8 Research Gaps and Dissertation Positioning . . . 18

3 Testing Methodology and Energy Source Evaluation **19**
- 3.1 Workflow . . . 19
- 3.2 Familiarization with Fraunhofer AICOS Testbed and Test Setup . . . 20
  - 3.2.1 Testbed and Capacitor Configurations . . . 20
  - 3.2.2 Environment and Equipment . . . 21
- 3.3 Energy Harvesting Sources and Modules . . . 22
  - 3.3.1 Solar Energy . . . 23
  - 3.3.2 Thermal Energy . . . 23
  - 3.3.3 Kinetic Energy . . . 23
  - 3.3.4 RF Energy . . . 23
- 3.4 Experimental Setup and Results . . . 23

3.4.1 Initial Tests . . . 24
3.4.2 Controlled Environment Tests . . . 26
3.4.3 Extended Duration Testing . . . 37
3.5 Performance Interpretation and Comparative Analysis . . . 46
3.5.1 Initial Testing Observations . . . 47
3.5.2 Controlled Testing Insights . . . 47
3.5.3 Long-Term Energy Accumulation . . . 48
3.5.4 Comparative Analysis and Summary . . . 48

4 Platform Development and Evaluation 49
4.1 Experimental Bench . . . 49
4.2 Riotee Platform . . . 50
4.2.1 Hardware and Firmware Architecture . . . 50
4.2.2 Step-by-Step Energy Consumption . . . 50
4.2.3 Single-Cycle Energy . . . 53
4.2.4 Discussion . . . 55
4.3 IN100 Platform . . . 55
4.3.1 Hardware Architecture . . . 55
4.3.2 Cycle-Level Measurements . . . 55
4.3.3 Twenty-Four-Hour Autonomy . . . 57
4.3.4 Discussion . . . 58
4.4 Comparative Assessment . . . 58
4.4.1 Timer Evaluation . . . 58
4.4.2 Sensor Evaluation . . . 59
4.5 Prototype Node Validation and Range Testing . . . 61
4.5.1 Test Setup and Environments . . . 62
4.5.2 Long-Duration Autonomy Results . . . 63
4.5.3 Control Test – Discharging . . . 66
4.5.4 BLE Range and Connectivity . . . 67
4.5.5 Summary and Impact . . . 68

5 Final Implementation and Results 69
5.1 Luxor Node: Final Design and Architecture . . . 69
5.1.1 Operatinal Logic and Flowcharts . . . 76
5.2 Preliminary Communication Testing . . . 79
5.2.1 RSSI-Based Range Tests . . . 80
5.2.2 Impact of Simultaneous Scanning on Packet Reception . . . 81
5.2.3 First Real Node Evaluation: Energy-Harvesting Test with Solar Panel . . . 82
5.3 Deployment and Final Testing . . . 86
5.4 Summary and Observations . . . 91

6 Conclusions and Future Work 93
6.1 Contributions . . . 93
6.2 Identified Limitations . . . 94
6.3 Future Development Opportunities . . . 94

A LIGHTED Schematic 97

B Step-by-Step Current Profiling of the Riotee Platform 111

C Current Profiling of the IN100 Platform **113**

D Antenna Simulation Figures **115**

E Node Schematic **123**

F Sensor Module Schematic **127**

G RSSI Heatmap Tables **129**

References **133**

List of Figures

1.1 Intermittent Execution Pattern for Batteryless IoT Systems 2
1.2 Applications of batteryless IoT sensors 3

2.1 Sensor Deployment Layout at Mithræum 8
2.2 Thin-film solar cell for IoT devices 9
2.3 TEG Installation at Mithræum Site 10
2.4 Piezoelectric Kinetic Harvesting Mechanism 11
2.5 ZenseTag Differential Sensing 12
2.6 Architecture of the LIGHTED multi-energy harvesting testbed, integrating solar, thermal, and kinetic energy sources [15]. 13
2.7 Supercapacitor Charging Performance 15

3.1 Overview of the Fraunhofer AICOS energy harvesting testbed 21
3.2 Layout of Fraunhofer AICOS First Floor 22
3.3 Fraunhofer AICOS test locations 22
3.4 Initial harvesting test setups 25
3.5 Solar Test Setup 26
3.6 SW-0.4M Performance 27
3.7 Indoor Solar Results 28
3.8 Indoor Solar Setup 29
3.9 Thermal Setup 29
3.10 Thermal - Resistive Heating 30
3.11 Thermal - Hot Air 31
3.12 Piezo Tests 32
3.13 Kinetic Setup 33
3.14 LTC3588-1 Setup 33
3.15 LTC3588-1 Tests 34
3.16 RF 915 MHz Results 35
3.17 RF Setup 36
3.18 RF 2.45 GHz Setup 36
3.19 2.45 GHz RF Charging Results 37
3.20 labsetup 39
3.21 24H Lab Solar Indoor 40
3.22 24H Lab Solar Indoor 2 41
3.23 openspacesetup 42
3.24 24H Open Space Solar Indoor 43
3.25 24H Open Space Solar Indoor 2 44
3.26 salasetup 45

3.27 24H Meeting Room Solar Indoor 46

4.1 Riotee 49
4.2 Riotee Power Routing 50
4.3 Riotee Measurement Setup 51
4.4 Riotee Bench Setup 51
4.5 Riotee Consumption Chart 52
4.6 Riotee Measurement Cycle 53
4.7 Single-Cycle Input Power 54
4.8 Single-Cycle Capacitor Voltage 54
4.9 IN100 Test Setup 56
4.10 Open Space 24h 57
4.11 Prototype Node Block Diagram 61
4.12 Prototype Node in Open Space 62
4.13 BLE Dongle Receiver Setup 63
4.14 Capacitor Voltage – Open Space 64
4.15 Input Power and Lux – Open Space 64
4.16 Capacitor Voltage – Meeting Room 65
4.17 Input Power and Lux – Meeting Room 66
4.18 No-Solar Control Case 66

5.1 Different views of the Luxor node showing the main hardware blocks highlighted in color (yellow – PMIC, white – BLE SoC, red – timer, blue – antenna, pink – sensor interface, green – VIN/GND to connect the solar panel, orange – supercapacitor, purple - SHTC3 sensor). 70
5.2 AEM10941 harvester schematic: PV input, MPPT configuration, capacitor bank, and regulated HV output. 72
5.3 IN100 BLE SoC section with antenna interface, decoupling capacitors, and power control MOSFETs. 73
5.4 TPL5110 timer circuit for duty cycling and power gating of the mainboard. . . . 73
5.5 Sensor module schematic featuring the SHTC3 temperature and humidity sensor. 74
5.6 8-pin connector linking the mainboard to the modular sensor board. 74
5.7 USB-C programmer used for firmware upload and debugging of the IN100 BLE SoC. 75
5.8 Different views of the Luxor node with modular design (missing the supercapacitor). 76
5.9 Final Luxor node prototype. 76
5.10 IN100 firmware execution flow during a single active cycle. 77
5.11 Overall flowchart of the batteryless node including energy harvester, timer, IN100, and sensor logic. 78
5.12 Flowchart of the BLE scanning receiver, responsible for decoding and forwarding Luxor node data. 79
5.13 RSSI testing with external and internal antenna: various indoor scenarios. 80
5.14 Simultaneous scanning setup in the laboratory. The transmitting node is circled in **red**, while the scanning devices are highlighted in **yellow**. 81
5.15 Node 1 during initial deployment with solar panel attached. 84
5.16 Node 2 operating without solar panel after the initial harvesting phase (same node used in charging/discharging tests). 84
5.17 Luxor charging test: Capacitor bank voltage and estimated battery percentage under ambient light with solar panel connected. 85

5.18 Luxor discharging test: Capacitor bank voltage and estimated battery percentage after disconnecting the solar panel. 85
5.19 Close-up of USB dongles used for multi-node scanning. 87
5.20 Fraunhofer office floor plan with Luxor node positions: Node 1 (red), Node 2 (green), Node 3 (brown), Node 4 (orange), Node 5 (pink). 87
5.21 Final deployment locations of the five Luxor nodes across the Fraunhofer office. . 88
5.22 Example of the Luxor monitoring dashboard (Node 4), developed in Home Assistant by Diogo Gonçalves at Fraunhofer. The interface displays sensor data, energy status, and communication metrics in real time. 90

B.1 Riotee Current Profiling Results 112

C.1 IN100 Current Profiling Results 114

D.1 Simulated return loss (S11) showing resonance near 2.48 GHz. 116
D.2 Smith Chart of simulated input impedance showing impedance approaching 50 Ω at resonance. 117
D.3 Real part of the terminal Z-parameter across frequency. 118
D.4 Imaginary part of the terminal Z-parameter across frequency. 119
D.5 Simulated 3D antenna gain pattern. 120
D.6 Alternate 3D antenna gain view showing secondary lobes. 121
D.7 Alternate 3D antenna gain perspective highlighting directional lobes. 122

G.1 RSSI values for the Luxor node using an external antenna across different locations and transmission powers. 130
G.2 RSSI values for the Luxor node using an internal antenna across different locations and transmission powers. 131

List of Tables

1 Contribution of Batteryless IoT Devices to UN Sustainable Development Goals. . vi

2.1 Comparison of Energy Harvesting Techniques. 13

4.1 Riotee Current Profile 52
4.2 Representative current profiling results for IN100 platform (averaged over 11 cycles, excluding first measurement because of Timer initialization). 56
4.3 Riotee vs IN100 58
4.4 Comparison between TPL5110 and TPL5111 [41, 42]. 59
4.5 Comparison of Humidity and Temperature Sensors [23, 35, 36, 40]. 60
4.6 Message transmission results (Prototype Node – Open Space). 67
4.7 Message transmission results (Prototype Node – Room 1.11). 68

5.1 Message transmission results (Luxor 1 test). 83
5.2 Extended message transmission and detection results over several days for both nodes. 83
5.3 Final deployment configuration for multi-node test. 86
5.4 Extended message transmission and detection results over several days for the five deployed nodes. 91

List of Acronyms

ADC	Analog-to-Digital Converter
AEM	Ambient Energy Manager (e-Peas PMIC family)
AICOS	Assistive Information and Communication Solutions
BLE	Bluetooth Low Energy
CPU	Central Processing Unit
ESR	Equivalent Series Resistance
GUI	Graphical User Interface
IoT	Internet of Things
IIoT	Industrial Internet of Things
IV	Current–Voltage characteristic curve
LED	Light-Emitting Diode
LFXTAL	Low-Frequency Crystal Oscillator
MCU	Microcontroller Unit
MPPT	Maximum Power-Point Tracking
OTP	One-Time Programmable
PCB	Printed-Circuit Board
PIFA	Planar Inverted-F Antenna
PMIC	Power-Management Integrated Circuit
PPK2	Nordic Power Profiler Kit II
PV	Photovoltaic
RF	Radio Frequency
RFID	Radio Frequency Identification
RSSI	Received Signal Strength Indicator
S11	Reflection coefficient / return loss
SDK	Software Development Kit
SDGs	Sustainable Development Goals
SoC	System-on-Chip
TaDA	Task Decoupling Architecture
TEG	Thermoelectric Generator
UART	Universal Asynchronous Receiver–Transmitter
U.FL	Ultra Miniature Coaxial Connector
UN	United Nations
USB	Universal Serial Bus

Chapter 1

Introduction

The Internet of Things (IoT) has significantly revolutionized many industries enabling real-time data collection, automation and monitoring in various applications such as health care, agriculture, environmental monitoring, and industrial automation. In addition to all of these advantages, most IoT devices continue to rely on batteries as their primary power supply. Throughout this dissertation, the term battery specifically refers to chemical batteries, since in engineering terminology any discrete energy storage element (including capacitors or supercapacitors) could technically be considered a battery. Chemical batteries are expensive, large, environmentally hazardous and require regular replacement and maintenance. These limitations make it challenging to scale and sustain IoT systems, especially in inaccessible or sensitive applications, such as medical implants or remote monitoring stations [13, 45].

This dissertation addresses these challenges through research on batteryless sensing technology, enabling energy harvesting mechanisms to support autonomous devices during operation. Most systems use natural ambient sources of energy such as solar, kinetic, thermal energy, and RF towards the removal of conventional batteries that introduce major environmental and logistical drawbacks. This integration comprises the different mechanisms of energy harvesting with an appropriate energy storage system, such as capacitor banks, optimized about a set of energy profiles and requirements of use [15]. In particular, while capacitor banks may offer fast charge/discharge cycles with extended lifetime, their suitability heavily depends on both the capacitance requested by an application and the intermittency of available sources, which leads to intermittent execution patterns as illustrated in Figure 1.1. The thoughtful design of the products for reliability and efficiency in continuous operation at minimal environmental impact and maintenance costs enables IoT deployments in previously inaccessible or challenging environments, like remote monitoring sites or industrial automation settings where traditional battery replacement is impractical [17, 19].

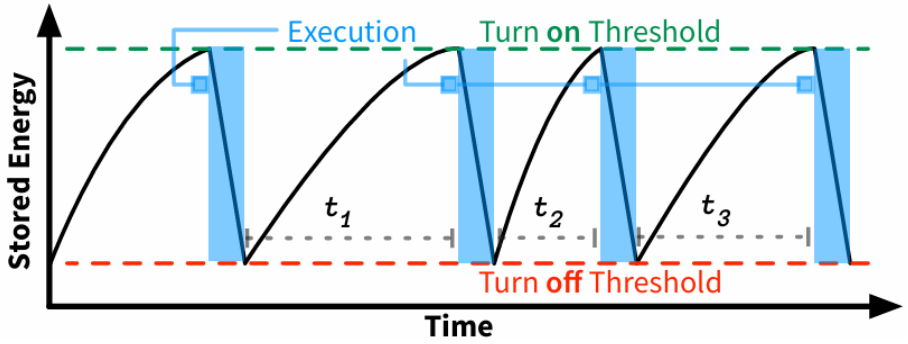

Figure 1.1: Intermittent Execution Pattern for Batteryless IoT Systems [17].

1.1 Context and Topic of the Work

The Internet of Things (IoT) environment, as defined by the Ambient IoT initiative [3], envisions a globally connected infrastructure where everyday objects become part of a pervasive digital ecosystem through seamless sensing, communication, and computation. Within this context, the work of this dissertation contributes to advancing sustainable IoT by addressing the limitations of conventional battery-powered devices.

This work is positioned within the wider context of sustainable IoT development and targets the design, implementation, and validation of batteryless IoT devices. In this dissertation, the notion of batteryless sensorization refers to ensuring that a device, without any dependence on chemical batteries, can still maintain its fundamental sensing and communication tasks by harvesting ambient energy. This capability eliminates the need for external intervention (such as battery replacement or recharging), allowing devices to operate autonomously and indefinitely. At the same time, such architectures introduce important constraints: harvested energy is often scarce and intermittent, which requires careful optimization of sensing frequency, communication overhead, and storage design.

The proposed devices were therefore designed to scavenge energy from the environment and buffer it in supercapacitor-based storage banks, enabling continuous or predictable operation even under variable lighting and intermittent power conditions. In that respect, this work addresses both the technical and operational challenges of batteryless systems, aiming for scalable and low-maintenance IoT deployments that align with the increasing demand for greener and longer-lasting sensing technologies [2, 17].

Applications of batteryless IoT range from medical implants and wearables to large-scale environmental monitoring networks and industrial IoT infrastructure. These applications span diverse domains, from industrial monitoring to environmental sensing and even wildlife tracking, as illustrated in Figure 1.2.

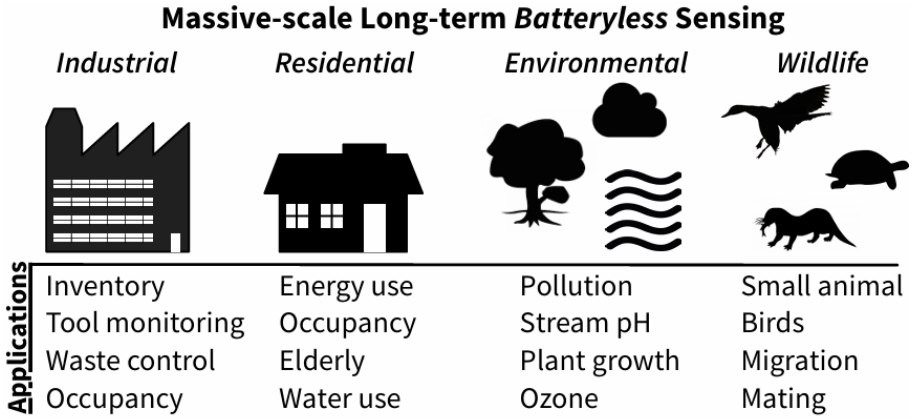

Figure 1.2: Applications of batteryless IoT sensors across different domains [2].

1.2 Motivation and Relevance

The work in this dissertation is inspired by the need for resilient self-sustaining IoT systems which can survive by their own in scenarios where maintenance is not easy or economically viable. Battery-driven state-of-the-art IoT deployments are often costly, especially at scale or in hard-to-reach or sensitive locations, and pose significant logistical challenges. Such great dependency on batteries severely limits scalability and sustainability for IoT technology because, in most of these environments, frequent replacements or maintenance tasks are highly impractical or impossible to perform. For example, battery replacement or recharging in remote environmental monitoring stations or medical implants is impossible. Therefore, the technical necessity of developing batteryless IoT systems that can harvest ambient energy and operate reliably under intermittent power conditions goes on to become a step toward achieving more sustainable and scalable IoT solutions.

On the other hand, batteryless IoT devices have some exciting economic and environmental benefits. It will significantly reduce electronic waste since systems will not use either disposable or rechargeable batteries, which have been among the main contributors to electronic waste globally. Besides, they reduce operational costs since there is no longer a need for periodic replacements of batteries or installation of recharging infrastructure, especially in remote or inaccessible areas. Benefits such as these make batteryless IoT devices the cornerstone for greener IoT technologies. With IoT being integrated into various everyday applications-from health to environmental monitoring and industrial automation-the ability to overcome the need for batteries will play an important role in the deployment of scalable, reliable, and viable solutions. Addressing such challenges, the road to long-term, low-maintenance IoT solutions is paved by batteryless systems to meet global sustainability goals. [2, 13].

This work is also motivated by the growing convergence between technological development and global sustainability programs. The batteryless IoT system, by providing autonomous operation due to energy harvesting, has a positive impact on electronic waste reduction and responsible

consumption of resources. This directly addresses objectives outlined in the United Nations Sustainable Development Goals (SDGs) [43].

1.3 Problem Statement and Challenges

This dissertation mainly deals with the perpetual operation of batteryless IoT devices, irrespective of any traditional means of supplying power. To realize such an objective, many technical and design issues need to be tackled, not restricted to but perhaps including the following:

- **Intermittent Energy Sources**: Ambient energy sources including solar, thermal, and kinetic energies exhibit stochastic availability and intensity, making them difficult to rely on for steady power supply.
- **Energy Harvesting Optimization**: Devices shall be flexible in such deployment conditions that can capture the maximum possible energy from the surroundings. This involves customizing the available energy harvesting techniques with what is available at each particular place.
- **Efficient Energy Storage and Regulation**: The storage solutions should provide the right balance between capacity and leakage, retaining power for longer periods. Energy regulation front-ends should have optimal conversion rates to facilitate proper utilization [38].
- **Self-Awareness and Decision-Making**: Self-aware capabilities in devices will enable them to monitor their energy levels and make runtime decisions on task feasibility. This feature is highly desired for performance and lifetime enhancement in networks.
- **Scalability and Network Integration**: Large-scale deployment of distributed networks of batteryless IoT devices calls for innovative architectures and communication strategies with a focus on energy efficiency while maintaining scalability.

These are particularly critical in applications related to remote monitoring, healthcare, and smart infrastructure, where reliable longevity is an unbending requirement. Balancing energy harvesting, storage, and consumption in such uncertain and dynamic conditions is the key focus area in this work [2, 13]. This work shows that even with changing indoor illumination, reliable, consistent-schedule operation is attainable, using a 30-minute advertising interval with more than 99% message detection efficiency, as demonstrated in Chapter 5.

1.4 Objectives

The overall goal of this research study is the design and development of self-autonomous batteryless IoT devices, validated through a multi-node real-world deployment. While not addressing large-scale scalability, this work establishes the technical foundations required for future expansion of such systems. Achieving this objective required overcoming critical challenges in energy harvesting, storage, and management to ensure reliable and continuous operation.

In this respect, the following specific objectives are identified and elaborated in this work:

- **Optimizing Energy Harvesting Mechanisms**: Evaluate and compare multiple ambient energy sources, including solar, thermal, kinetic, and radio frequency, under realistic indoor conditions. Based on experimental analysis, define the type of energy harvesting that is the most consistent and practical option to ensure reliable operation in fluctuating or intermittent environments.
- **Designing Energy-Efficient Architectures**: Propose innovative architectures at the system level that can achieve minimum energy consumption with high performance such that devices can operate autonomously without the use of conventional power sources. The focus is on lightweight, hardware-assisted strategies that minimize the need for complex runtime energy-awareness, while still ensuring that sensing and communication tasks are reliably executed under constrained energy conditions.
- **Supporting Deterministic Scheduling Without Firmware Overhead**: Attain reliable periodic task scheduling through ultra-low-power hardware timers, avoiding the reliance on software-based runtime energy management and guaranteeing timely data transmission even in energy-constrained environments.
- **Practical Validation and Deployment**: Conduct rigorous testing and validation of the proposed solutions in real-world scenarios. This includes in-situ validation to identify the most efficient energy sources for specific deployment conditions, optimizing energy availability and system performance.

Addressing these objectives will enable this dissertation to make worthwhile contributions toward advancing sustainable IoT technologies and setting the ground for further research and large-scale deployment.

1.5 Contributions

This dissertation advances the development of IoT technologies by addressing key design and deployment gaps in batteryless systems. The main contributions are as follows:

- **Development of a Novel Architecture**: A comprehensive architecture for batteryless IoT devices has been designed that integrates the latest energy harvesting techniques, efficient storage solutions such as Capacitor Banks, and self-aware energy management strategies. This architecture will ensure reliable and autonomous operation under intermittent power conditions.
- **Innovation in Energy Harvesting Techniques**: New techniques have been proposed to adapt energy harvesting techniques to particular deployment scenarios. Innovations improve the autonomy and reliability of devices by adapting energy harvesting systems to environmental conditions and application-specific energy requirements.

- **Fundamental Building Blocks for System Integration**: The key elements and strategies were developed to facilitate the integration of batteryless IoT devices in distributed sensing networks. Not an entirely full-fledged framework, these fundamental building blocks optimize communication protocols and resource utilization, enabling scalable and seamless operation in various IoT ecosystems.
- **Experimental Validation in Real-World Settings**: It has been subjected to extensive experimental validation under real-world conditions that prove the proposed system is long-term sustainable and reliable. Results show that this is an ideal application of batteryless IoT devices for resource-scarce and hostile environments.
- **Guidelines for Practical Deployment**: Thorough RSSI and packet loss measurements in various locations were crucial in guiding the optimal positioning of receivers, transmission power settings, and antenna configurations for reliable indoor deployments.

By addressing these issues, this dissertation provides a strong foundation for innovation in sustainable IoT systems, making these deployments energy-efficient and maintenance-free.

1.6 Structure of the Dissertation

This document is organised as follows:

- **Chapter 1 – Introduction**
  Presents the motivation, problem statement, objectives and main contributions of the work.
- **Chapter 2 – Background and State of the Art**
  Combines the theoretical foundations of energy harvesting and intermittent computing with a critical survey of recent advances in batteryless IoT, highlighting the research gaps addressed in this dissertation.
- **Chapter 3 – Testing Methodology and Energy Source Evaluation**
  Describes the Fraunhofer AICOS testbed - LIGHTED, the controlled experiments on solar, thermal, kinetic and RF harvesting, and the criteria used to select the primary power source.
- **Chapter 4 – Platform Development and Evaluation**
  Compares the Riotee and IN100 processing engines through current profiling, 24-hour autonomy tests and a quantitative energy budget.
- **Chapter 5 – Final Implementation and Results**
  Details the design of the modular, batteryless sensor node, presents range tests, multi-day deployments inside the office and overall system performance.
- **Chapter 6 – Conclusions and Future Work**
  Summarises the main findings, discusses limitations and outlines directions for future research.

Chapter 2

Background and State of the Art

The Internet of Things (IoT) has completely revolutionized data collection, processing, and automation in disparate domains, from healthcare to industrial systems and environmental monitoring. Traditional IoT systems are severely limited by their reliance on batteries, which must be periodically maintained, have a limited lifetime, and pose environmental challenges. Energy harvesting and intermittent computation enable a new generation of batteryless IoT systems that open new perspectives toward sustainable and autonomous operation. This evolution has sparked active research on various fronts, from energy harvesting techniques and robust system designs to practical applications in resource-limited environments. This chapter outlines the fundamental aspects of batteryless IoT systems, provides a comprehensive literature analysis, highlights significant contributions and existing challenges, and positions this dissertation within the wider context of current advancements [45].

2.1 Introduction to Batteryless IoT Systems

Batteryless IoT systems harvest ambient energy from sources such as light, thermal gradients, radio frequency signals, and mechanical vibrations, and use this energy to sustain their operation. By removing the dependency on conventional batteries, these systems overcome one of the most significant barriers to scalable and sustainable IoT deployments. The reliance on batteries introduces environmental hazards, frequent replacement requirements, and limited lifespans, all of which restrict the feasibility of deploying devices in hard-to-reach or mission-critical scenarios. Batteryless technologies are particularly relevant for implantable medical devices, where replacing or recharging a battery is not only impractical but can also pose serious health risks [13]. In remote monitoring stations and expansive sensor networks, battery replacement quickly becomes logistically unmanageable and economically unsustainable, positioning energy harvesting as a key enabler for long-term, autonomous sensing [17].

A notable real-world example of this approach is the deployment at the Mithræum archaeological site, where researchers demonstrated how batteryless sensors could provide continuous

monitoring in a historically sensitive environment. In this deployment, sensors powered by thermal and kinetic energy successfully enabled long-term tracking of environmental conditions, such as humidity and temperature, without the need for invasive maintenance or disruptive battery replacement.

Figure 2.1 illustrates the sensor deployment layout across the archaeological site. Two types of devices were installed: I/A devices (brown circles), which combined temperature, humidity, inclination, and acceleration sensing, and T/H devices (blue triangles), which measured temperature and humidity. Their placement was carefully optimized to balance two key requirements: (i) ensuring adequate coverage of the most critical areas of the site for environmental monitoring, and (ii) positioning devices in locations where sufficient ambient energy could be harvested to sustain their operation. For instance, I/A devices were positioned in regions with higher visitor flow or illumination to maximize available energy, while T/H devices were more widely distributed to capture spatial variations in environmental conditions. This deployment highlights how energy availability and monitoring needs must be co-optimized in practice to achieve reliable, maintenance-free operation of batteryless IoT systems in sensitive and hard-to-access environments.

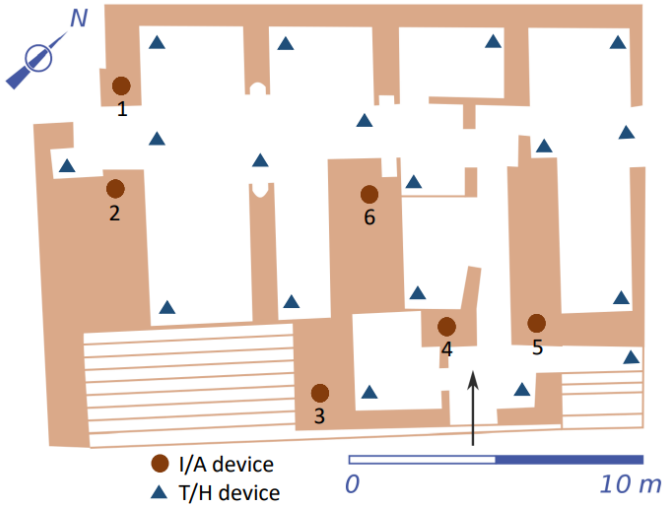

Figure 2.1: Sensor Deployment Layout at Mithræum, optimized for energy harvesting and long-term monitoring [2].

2.2 Energy Harvesting Techniques for Batterryless Systems

Energy harvesting represents the cornerstone and vital backbone of batteryless IoT systems, enabling devices to operate independently by converting ambient energy into electrical power in usable form. Several works have looked into different energy sources, their efficiency, and integration challenges. The following section highlights various key energy harvesting techniques, their operational principles, and their practical applicability in real-world scenarios. For clarity, a comparative overview of their energy densities, application domains, and limitations is provided later in Table 2.1.

2.2.1 Solar Energy

Solar energy harvesting requires photovoltaic (PV) cells to generate electrical energy from sunlight. The output power can be approximated as:

$$P_{\text{out}} \approx \eta_{\text{pv}} A E_e, \tag{2.1}$$

where η_{pv} is the PV conversion efficiency, A is the illuminated cell area, and E_e is the irradiance (W/m^2). Under indoor conditions, the irradiance may be related to illuminance (E_v, lux) by a luminous efficacy factor [16, 28].

It has long been a reliable source for powering IoT devices, especially in outdoor applications. Recently, thin-film solar cells have emerged as a promising technology that offers both physical flexibility and improved efficiency. These advances have made it feasible to integrate solar energy harvesting into IoT devices without significant design trade-offs [46]. In addition, the development and optimization of PV materials have resulted in better performance even under indoor low-light conditions, which previously remained a challenge for using solar energy indoors. For instance, the study on PV badges in attendance tracking exhibited efficient energy harvesting in low-light conditions, extending practical usages of solar energy harvesting to indoor applications [15]. Furthermore, studies on multi-source energy harvesting show how solar power can be effectively combined with other sources to achieve the best possible energy utilization [15]. An example of a compact thin-film solar panel used in such IoT applications is shown in Figure 2.2.

Figure 2.2: Example of a thin-film photovoltaic (PV) cell (KXOB141K06F) commonly used for energy harvesting in low-power IoT applications [5].

2.2.2 Thermal Energy

Energy harvesting from heat uses temperature gradients and converts them into electrical energy using thermoelectric generators (TEGs). The open-circuit voltage of a TEG is given by:

$$V_{\text{oc}} = NS\Delta T, \tag{2.2}$$

where N is the number of thermocouples, S the Seebeck coefficient, and ΔT the temperature difference. The maximum output power occurs at matched load and is approximated as:

$$P_{\max} = \frac{(NS\Delta T)^2}{4R_i}, \tag{2.3}$$

with R_i the internal resistance of the device [34].

These generators show high efficiency in the cases of large temperature gradients. They have been successfully tested on subterranean archaeological sites, where the heat source is constant and the possibility for long-term operation is realistic [2]. New emerging materials and designs have resulted in higher performance in TEGs, increasing their applicability in environments that have a medium thermal gradient. Research on compact systems for waste heat recovery has also increased their use in industrial and biomedical domains [13, 45]. Figure 2.3 shows a real-world deployment of a TEG-based harvesting system at the archaeological site of Mithræum, where the temperature gradient between ambient air and underground concrete is used for long-term detection.

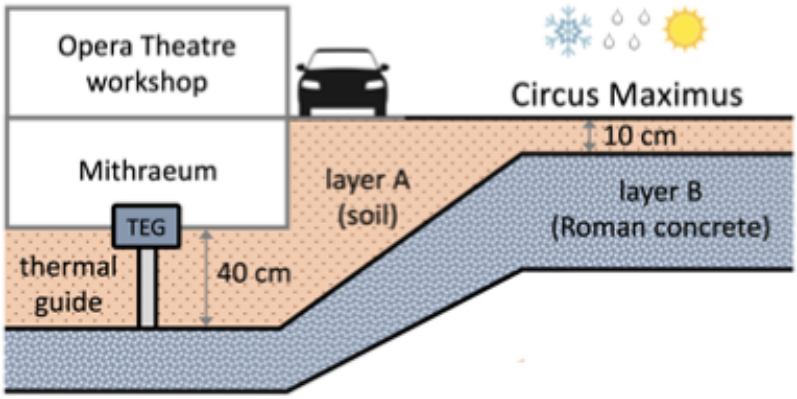

Figure 2.3: TEG harvester installation at the Mithræum of Circus Maximus, exploiting temperature gradients between indoor air and underground Roman concrete layers to enable continuous thermal energy harvesting [2].

2.2.3 Kinetic Energy

Kinetic energy harvesting is the process by which mechanical energy from vibrations or motion is converted into electrical power. A simplified piezoelectric harvester power model indicates that the generated power is proportional to the square of displacement amplitude and excitation frequency:

$$P \propto d_{31}^2 Y x^2 f, \tag{2.4}$$

where d_{31} is the piezoelectric coupling coefficient, Y the Young's modulus, x the displacement, and f the vibration frequency [31].

This mechanisms have been used with much success in wearable applications or environments where continuous mechanical activity takes place, such as industrial machinery. It finds a wide

number of applications in dynamic environments, like wearable devices or industrial machinery, where there is continuous mechanical activity. Other recent developments exhibit new methods of vibration energy harvesting in batteryless IoT systems, such as the hybrid generator used in visible light communication (VLC) systems [37]. Figure 2.4 represents a typical mechanism of piezoelectric-based kinetic energy harvesting that captures energy from motions in an effective way.

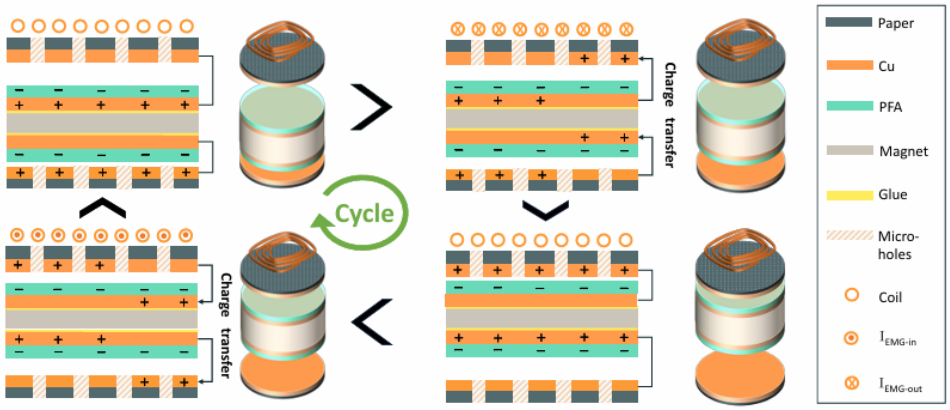

Figure 2.4: Piezoelectric-based kinetic energy harvesting mechanism [37].

2.2.4 Radio Frequency Energy

RF energy harvesting captures ambient electromagnetic waves broadcast by communication devices and converts them into electrical energy. The incident power on the antenna is:

$$P_{\text{in}} = SA_{\text{eff}}, \qquad A_{\text{eff}} = \frac{\lambda^2 G}{4\pi}, \tag{2.5}$$

where S is the power density (W/m^2), λ the wavelength, and G the antenna gain. The harvested DC output is then:

$$P_{\text{out}} = \eta_{\text{rf}} P_{\text{in}}, \tag{2.6}$$

with η_{rf} the rectifier efficiency [6, 44].

This is quite effective in urban areas, where there is a high density of RF signals, which enables the operation of low-power IoT devices. In this context, RF energy harvesting collects electromagnetic waves from ambient sources that could be communication devices or networks to power low-energy IoT devices. This allows the deployment of RFID-assisted sensor interfaces in the urban environment [7]. Figure 2.5 illustrates how the ZenseTag system leverages differential analog modulation and a twin-tag single-antenna interface to achieve robust sensing by mitigating the phase corruption effects that occur with co-located dual tags. Recent innovations involve systems that combine RF harvesting with other energy sources, showing potential for more efficient use of energy utilization [7, 14]. Furthermore, the efficiency and reliability of RF energy are enhanced by using them in combination with other sources [37].

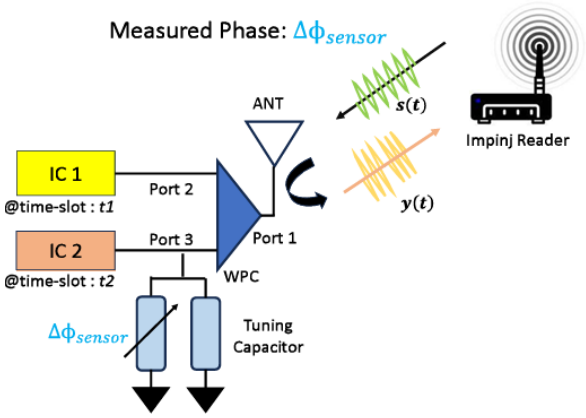

(a) Differential sensing – ZenseTag

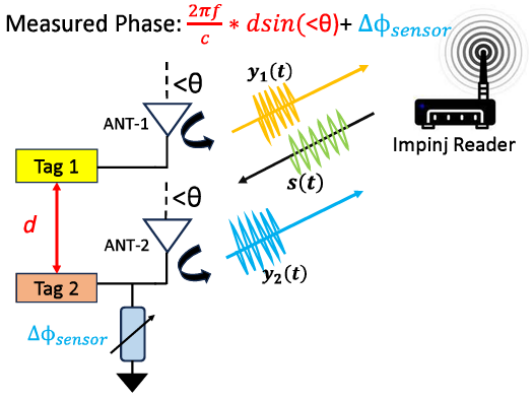

(b) Differential sensing – dual tags

Figure 2.5: Comparison of ZenseTag's twin-tag single-antenna interface with conventional co-located dual tags. ZenseTag achieves robust RF sensing by avoiding phase corruption issues present in dual-tag designs [7].

2.2.5 Hybrid Energy Harvesting Systems

These harvesters merge various energy sources such as solar, thermal, and kinetic energies that enhance energy availability, hence reliable operation under variant and dynamic environments. Recent works have also proposed hybrid energy harvesting systems, where the sources are combined: solar, RF and kinetic energy [15]. This will make energy availability maximum, with ensured system reliability for variable environmental conditions [15, 37]. By exploiting the complementary strengths of the individual sources, these systems can handle issues with individual sources such as irregular sunlight, low thermal gradient, or infrequent motion [15]. This makes hybrid systems particularly effective in situations where environmental conditions are not predictable or are highly variable.

Figure 2.6 illustrates the architecture of the LIGHTED testbed, the state-of-the-art testbed that features multi-energy harvesting. It integrates various energy sources in such a way that transitions to other modes of energy harvesting may be performed seamlessly depending on environmental

conditions. The LIGHTED testbed allows for energy harvesting from more than one source simultaneously, but experimental studies on the testbed recommend operating the testbed with one source of energy and a capacitor bank at any given time for efficiency and stability in the energy supply. [15].

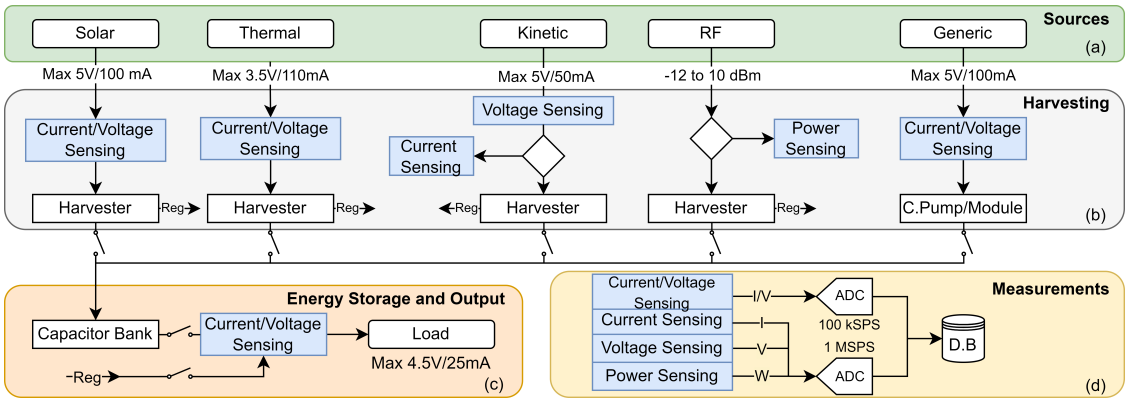

Figure 2.6: Architecture of the LIGHTED multi-energy harvesting testbed, integrating solar, thermal, and kinetic energy sources [15].

In summary, Table 2.1 makes a comparison of some of the most commonly used energy harvesting techniques concerning energy density, optimal environmental conditions, applications, and challenges.

Table 2.1: Comparison of Energy Harvesting Techniques.

Technique	**Energy Density**	**Optimal Conditions**	**Applications**	**Challenges**
Solar Energy	High (100–200 mW/cm²) [46]	Direct sunlight or well-lit indoor settings	Outdoor IoT, smart agriculture	Poor performance in low-light environments
Thermal Energy	Moderate (50 mW/cm²) [13]	Constant heat sources or thermal gradients	Wearables, industrial monitoring, biomedical implants	Limited availability in low thermal gradients
Kinetic Energy	Low to Medium (1–10 mW/cm²) [37]	Continuous motion or vibrations	Wearables, industrial machinery, vehicular sensors	Dependence on motion frequency and amplitude
RF Energy	Very Low (0.01–0.1 mW/cm²) [14]	High RF signal density, urban areas	Low-power sensors, urban IoT	Low conversion efficiency, dependence on RF availability
Hybrid Systems	Variable [15]	Combined sources, dynamic environments	Remote monitoring, hostile environments	Complexity of integration and energy conditioning

2.3 Energy Storage and Regulation

Energy storage and regulation mechanisms will be highly instrumental in the design of a consistent batteryless IoT system, assuming energy may arrive intermittently. There exist various storage technologies; however, capacitor banks are preferred due to their superior capability for rapid charging and discharging, operational life, and the assurance of high-power bursts in operation. These make them ideal for energy harvesting systems where stability and reliability are paramount.

Energy storage devices like capacitor banks thus serve a twofold purpose: they dampen the fluctuations in energy supply and ensure reliable operation when the harvesting is low or intermittent. Certain specific examples of batteryless systems, such as the LIGHTED testbed and similar platforms, point to supercapacitor-based architectures as key for consistent energy delivery and regulation [15, 19]. The choice of capacitance directly impacts charging and discharging times, creating a trade-off between fast charging for quick start-up and larger storage for extended operation.

The relationship between capacitance and charge time follows the exponential law of capacitor charging and discharging:

$$V(t) = V_C\left(1 - e^{-t/\tau}\right), \tag{2.7}$$

where $V(t)$ is the capacitor voltage at time t, V_C is the maximum supply voltage, and $\tau = RC$ is the time constant. This formulation explains the trends observed in practice: smaller capacitors charge more quickly to the minimum operational voltage, while larger capacitors take longer but allow for extended energy availability.

Figure 2.7 illustrates this relationship by showing the charging curves of supercapacitors with different capacitance values. Smaller capacitors reach the minimum operational voltage more quickly, while larger capacitors take longer to charge but can sustain operation for longer periods [37].

Moreover, research illustrates how implantable medical devices can leverage capacitor banks to achieve energy buffering and reliable operation by harvesting energy from various sources [13]. Similarly, in the recent past, low-power circuit advancements have further improved the possibility of regulating and adapting energy usage in batteryless IoT systems [19, 38, 47]. In this context, energy management ICs and low-power regulators play a crucial role, ensuring efficient transfer of harvested energy to the load, protecting storage elements from over-voltage, and stabilizing supply for sensitive components [4, 10].

Such challenges due to intermittent energy availability have been addressed by advanced techniques such as "Dynamic Frequency Switching" [33] and "Task Scheduling for Energy-efficient Operation" [19]. These ensure that the energy harvested is used efficiently to reduce losses during regulation processes.

Finally, efficient capacitor-based storage solutions combined with advanced regulation strategies ensure maximum energy utilization toward reliable and long-term autonomous operations of batteryless IoT systems.

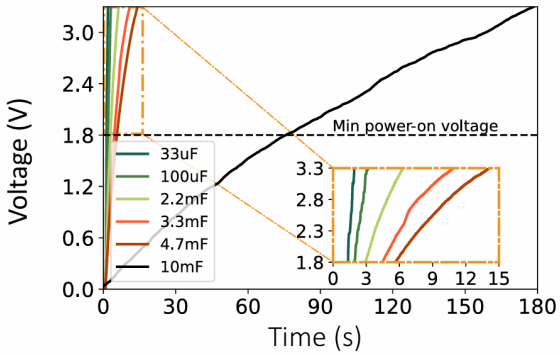

Figure 2.7: Charging curves of supercapacitors with different capacitance values, showing how larger capacitors require longer charging times but enable greater storage capacity and longer device operation [37].

2.4 Architectures for Intermittent Power Systems

The intermittent nature of power availability remains one of the major challenges for batteryless IoT systems. Several architectural strategies and innovations have been proposed to address this challenge:

2.4.1 Checkpointing and State Preservation

Checkpointing techniques allow devices to save their operational states periodically and resume operation seamlessly upon power interruptions. Rollback mechanisms ensure data integrity by reverting to the most recent stable state [18]. These techniques are particularly useful in real-time processing of data in critical applications, such as environmental monitoring and healthcare [48].

2.4.2 Task Scheduling and Energy Awareness

Task scheduling improves resource allocation by prioritizing vital tasks and delaying less critical ones. This approach ensures system reliability while maximizing efficiency by tailoring operations to the available energy budget. Energy-aware task scheduling techniques determine the optimal distribution of resources based on energy availability. These methods achieve higher efficiency and robustness by considering critical operations and postponing non-vital tasks. Additionally, advanced scheduling techniques, such as TaDA (Task Decoupling Architecture), decouple processing pipelines for improved workload distribution [19, 38, 48].

2.4.3 Fault Tolerance Mechanisms

Fault tolerance mechanisms ensure system stability under conditions with high energy uncertainty. Redundant data storage, adaptive algorithms, and selective data protection minimize losses of critical information and enhance the resilience of the system [22, 33]. These methods are very important for applications where a high level of reliability is required, like medical monitoring or critical

infrastructure. Fault tolerance strategies also ensure that the system remains stable even under unexpected energy conditions. For example, strategies like EXTREMIS use frequency switching to adapt dynamically to energy levels for increased resilience in low-power conditions [22, 33].

2.4.4 Integrated Hybrid Architectures

Hybrid architectures, combining checkpointing, task scheduling, and fault tolerance, provide robust solutions for intermittent systems. These architectures are especially useful in distributed sensor networks, where scalability and energy efficiency are key [15].

2.5 Benchmarking Methodologies for Batteryless Systems

Evaluating batteryless IoT systems requires novel benchmarking methodologies due to their intermittent nature. Traditional benchmarking metrics fall short in capturing metrics such as time-to-first-sample, energy cost per task, or recovery time after power failures.

Standardized benchmarking tools such as the LIGHTED testbed [15] allow controlled and reproducible evaluation of energy harvesting behaviors. The platform supports switching between solar, thermal, RF, and kinetic sources and enables comparison across energy profiles. Repeatability is ensured by simulating real-world lighting and motion patterns.

Profiling energy availability and consumption patterns in such environments is crucial for system design decisions. It allows engineers to identify performance bottlenecks, calibrate storage sizes, and develop energy-aware task schedulers. Design-time tuning using platforms like LIGHTED contributes to a more robust and predictable deployment of batteryless systems.

2.6 Applications of Batteryless IoT Systems

Batteryless IoT systems have shown huge potential in different fields to address the limitations of battery-dependent solutions and enable new applications. These systems are suitable for use in environments where frequent battery maintenance is difficult or infeasible. Their applications extend from office-based scenarios to more limited or essential settings. Notable applications include:

- **Healthcare and Medical Applications**: Body heat and motion-powered batteryless devices can support continuous and non-invasive monitoring of vital parameters. Wearables for office workers can track posture or stress levels and provide workplace health insights without ever having to recharge. In medical contexts, implantable systems combining capacitor banks with thermoelectric generators have demonstrated reliability in low-maintenance, long-term operation [13].

- **Environmental Monitoring**: Batteryless systems deployed in offices can monitor environmental parameters such as temperature, humidity, and light to optimize energy consumption

and comfort. On the other hand, in remote or harsh environments, batteryless IoT devices can also provide critical data on temperature, humidity, and air quality. However, traditional air quality sensors typically require batteries, since components like heating elements and fans are needed for CO_2 and particulate measurements. These designs are difficult to adapt for batteryless operation, whereas simpler systems for measuring key metrics like temperature and humidity remain fully viable [2].

- **Industrial IoT and Smart Infrastructure**: In both office and industrial environments, batteryless sensors can enable attendance tracking, meeting room usage analysis, predictive maintenance and energy-efficient lighting control. In particular, photovoltaic-powered beacons have been demonstrated for resource utilization tracking, reducing operational costs and supporting sustainability initiatives [46]. In manufacturing and Industrial Internet of Things (IIoT) contexts, batteryless sensing also enables predictive maintenance and structural health monitoring, where vibration and temperature anomalies can be detected early without relying on batteries [20].

- **Localization and Tracking Systems**: Without the use of batteries, IoT systems operating using ambient RF or cellular signals enable low-power, high-accuracy localization and navigation. These solutions are applicable to both logistics and office environments, supporting applications like asset tracking, location sharing of common equipment and ensuring the location of critical devices like defibrillators [14]. In logistics, batteryless RF-powered tags have been highlighted as enablers for warehouse automation and real-time asset visibility [20].

The Fraunhofer Institute represents a relevant deployment site for batteryless IoT systems, particularly in office environments. Pilot projects focus on smart offices, healthcare monitoring, and environmental sensing, where integrating batteryless solutions can improve sustainability and reduce maintenance needs. These initiatives provide a concrete scenario to demonstrate the high potential of batteryless IoT in real-world applications [15].

2.7 Sustainability and Environmental Impact

Transitioning to batteryless IoT systems drastically reduces electronic waste that is associated with the use of disposable batteries. As research has pointed out, there is a huge cost-effective scalability of such systems in IoT deployments [2, 13].

Moreover, industry analyses indicate that energy harvesting can significantly extend the operational lifetime of IoT and IIoT deployments, reducing battery waste while lowering maintenance costs in large-scale sensor networks [20]. Such approaches leverage ambient sources like indoor light, thermal gradients, and RF signals to ensure reliable long-term autonomy without the environmental footprint of conventional batteries.

Besides, the systems are in line with the United Nations Sustainable Development Goals (SDGs), particularly SDG 7 (Affordable and Clean Energy) and SDG 12 (Responsible Consumption and Production) [43]. Batteryless IoT systems ensure a greener and more eco-friendly technological ecosystem owing to energy harvesting mechanisms along with advanced computational frameworks.

2.8 Research Gaps and Dissertation Positioning

Despite these advances, several research gaps remain unaddressed:

- **Scalability**: The vast majority of state-of-the-art works consider a stand-alone device or just a small-scale number of nodes. Scalable solutions that can keep proper performance in any environment remain highly in demand. From a system perspective, practical IoT applications bring extra load due to energy harvesting, which still is the most critical challenge toward uninterrupted operation support [2, 17].
- **Energy Source Optimization and Selection**: Hybrid energy harvesting systems are very promising; however, additional research effort is needed to integrate them into compact, cost-effective designs. The selection of the most suitable energy source for a particular deployment scenario is still considered an open challenge. Therefore, this dissertation emphasizes that it is not only important to optimize energy harvesting techniques but also to select the most appropriate energy source based on the deployment context. For example, taking advantage of the Fraunhofer AICOS testbed enables customized testing of various energy sources in comparison with a wide range of realistic conditions to be able to select the best energy source for and variety of IoT applications [15, 46]. It can be used to research PV, kinetic, and hybrid energy sources toward batteryless IoT systems [14, 37].
- **Real-Time Processing**: It is still an open challenge to provide robust computations during intermittent power, especially in applications requiring real-time data acquisition and processing. Intermittent computing systems are critical in maintaining continuous operation in the presence of fluctuating power and their fault tolerance under low-power conditions is a subject of further study [18, 19].

In addressing these challenges, this dissertation presents the design of a fully autonomous, batteryless, and scalable IoT end-node system. It will integrate state-of-the-art energy harvesting techniques with efficient energy management strategies and robust architectures to ensure reliable operation in dynamic and resource-constrained environments. With an important focus on the selection of energy sources and scalability regarding real-time performance, this work hopefully can make significant contributions towards sustainable advances in IoT technologies by closing some of the identified gaps in research [45, 47].

Chapter 3

Testing Methodology and Energy Source Evaluation

This chapter outlines the test plan, experimental methods, equipment setup, and measured results used to evaluate and compare the different energy harvesting sources considered to power the desired batteryless sensor node. The main goal is to evaluate which ambient energy sources, solar, thermal, kinetic and RF, can provide sufficient energy for the autonomous operation of each sensor node with a certain advertising interval.

The chapter starts by detailing the general work plan and the familiarization steps with LIGHTED, the Fraunhofer AICOS testbed, followed by an extensive explanation of the experimental arrangement, which encompasses the environment, tools, and methods. The approach combines brief, controlled laboratory tests and long-duration measurements in real-world environmental settings, allowing for a comprehensive comparison of various harvesting techniques.

This research validates the most appropriate energy harvesting options for reliable, long-term, batteryless sensing applications by systematically assessing the energy output of each source and evaluating its stability, efficiency, and suitability for practical implementations.

3.1 Workflow

The experimental study of candidate energy sources was planned to occur from early February to mid-April 2025. The project workflow consists of five intentionally overlapping phases to allow simultaneous advancement in hardware measurements, firmware prototyping, and data analysis. This simultaneous method aims to enhance efficiency and facilitate iterative improvement using initial results.

Below is presented a summary of the tasks for each phase of the workflow.

Phase 1 – Initial Exploration. Perform quick, qualitative “sanity-check" assessments on the solar, thermal, kinetic and RF energy harvesters. The capacitor pre-charge remains uncontrolled throughout this phase, which is mainly for initial qualitative familiarization with the LIGHTED testbed and dashboard.

Phase 2 – Enhanced Sweeps. Repeat the same type of tests but in stricter conditions and ensuring the energy storage bank is completely discharged ($< 50\,\text{mV}$) and the lamp used is stabilized. These measurements will provide the first charge-versus-capacitance graphs, useful to start understanding which one of the energy harvesters will be more suitable for this application.

Phase 3 – Characterization of Ideal Stimulus. Operate each energy harvester under strictly controlled laboratory conditions: constant ambient temperature, humidity, illuminance and thermal gradient. Simultaneously, the Riotee firmware is tailored so that platform-specific behaviour is captured during the measurements.

Phase 4 – Extended Duration Validation. Perform continuous 24h data collection with the LL200-2.4-75 indoor solar panel and the 2.45 GHz RF rectifier in three representative indoor settings (Laboratory, Open-Space, Meeting Room 1.11). In early April, the evaluation of the consumption of the Riotee solution starts, followed immediately by comparative tests of the IN100.

Phase 5 – Data Minimization and Evaluation. Compare the solutions studied, based on their current consumption and elaborate plots and statistical overviews. An important milestone for this phase is confirming if indoor solar alone can fulfill the energy needs of the IN100 beacon system.

Phase 6 - System Prototyping, Testing, and Deployment. PCB design began in early May. Tests for beacon range and power were performed with prototype IN100 boards during May and the first half of June. Fabrication data was completed in June, allowing the PCBs to arrive in early July. Network deployment across the Fraunhofer layout was finalized and dissertation writing occurred throughout the remainder of July.

3.2 Familiarization with Fraunhofer AICOS Testbed and Test Setup

3.2.1 Testbed and Capacitor Configurations

The familiarization period focused on building a hands-on comprehension of the Fraunhofer AICOS energy harvesting testbed - LIGHTED [15]. This phase combined practical investigation with structured testing and established the basis for all later experiments. The testbed connects to a Raspberry Pi equipped with Wi-Fi capabilities, enabling real-time interaction through an integrated interface and remote database access via InfluxDB. The interface enables users to start and stop measurements, switch between harvesting and measuring modes, and adjust system configurations, including data acquisition frequency. The capacitor bank size is also adjustable directly on the testbed PCB. The database allows users to access stored measurement information and examine long-term trends for each energy harvesting method over selected time intervals.

During this stage, the emphasis was on exploring the electrical setup of the testbed, understanding the functions of its various regulators, and testing multiple energy harvesting sources,

including solar, thermal, RF, and kinetic. Experiments were made with various capacitor bank setups, using two supercapacitors (0.47 F or 1.0 F) along with eight ceramic capacitors between 22 µF and 220 µF (976 µF in total).

3.2.2 Environment and Equipment

The main experiments were carried out using the Fraunhofer AICOS energy harvesting testbed under controlled conditions. The surrounding environment was maintained at almost constant temperature and humidity. Illumination at the testbed location was monitored using an mobile application and later a BH1750 lux sensor placed close to the solar panels, while RF field strength inside the semi-anechoic enclosure was confirmed with a Rohde & Schwarz NRP-Z81 power sensor [32]. In case of the thermal tests, the temperature was measured with an InfiRay thermal camera.

The testbed, displayed in Figure 3.1, incorporates solar, thermal, kinetic, and RF energy harvesting modules within a common measurement framework. It is connected to a Raspberry Pi with Wi-Fi, enabling remote configuration and data acquisition via a dashboard interface.

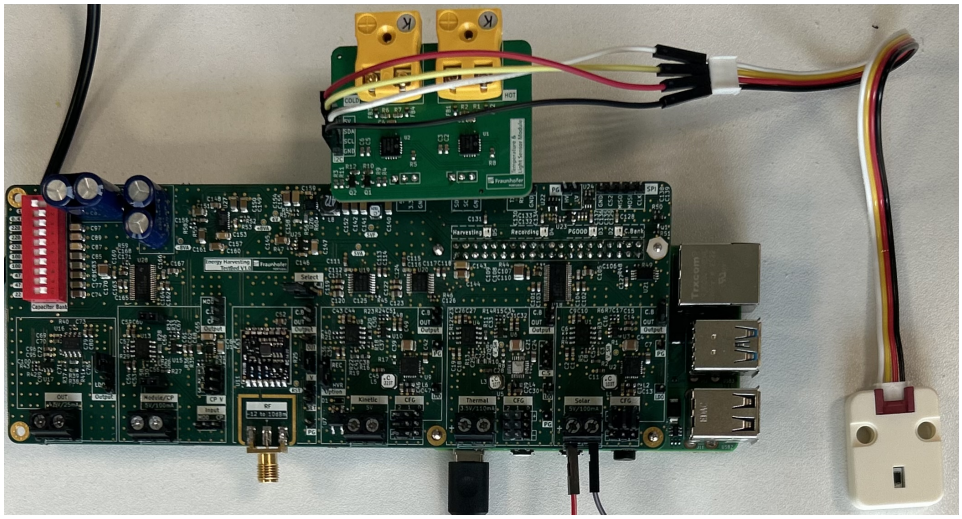

Figure 3.1: Overview of the Fraunhofer AICOS energy harvesting testbed with solar, thermal, kinetic, and RF modules connected to shared measurement board connected to a Raspberry Pi and USB data acquisition interfaces.

The energy storage solution was developed using a configurable capacitor bank, allowing tests with only ceramic capacitors (976 µF in total), only supercapacitors (0.47 F or 1.0 F), and a combination of both, in order to compare their performance and evaluate which configuration yielded the best results. Moreover, every AEM harvester module contained an internal output capacitor (typically 150 µF) which has to be considered and added into all energy calculations [10–12].

Testing took place in multiple areas of the Fraunhofer AICOS building, which layout is illustrated in the floor plan in Figure 3.2. The spatial diversity enabled characterization of each energy harvesting source in different environmental conditions.

Figure 3.2: Floor layout of the Fraunhofer AICOS building. The yellow square on the left highlights the open space area, while the green lines on the right correspond to the laboratory.

Figures 3.3a to 3.3c are real images of some parts of the Fraunhofer AICOS office, which correspond to the real test environments employed during all the tests of this work. Open-plan offices (Figure 3.3a) offered varied ambient lighting, benefitial for realistic low-intensity scenarios. Meeting rooms (Figure 3.3b) allowed more constant lighting setups, whereas the electronics laboratory (Figure 3.3c) was used for example for device flashing, capacitor discharging, proto boards testing and controlled ambient experiments.

(a) (b) (c)

Figure 3.3: Photographic overview of different test locations inside Fraunhofer AICOS used for harvesting trials, illustrating the diversity of lighting and spatial configurations.

3.3 Energy Harvesting Sources and Modules

This section provides a description of the energy harvesting modules of the Fraunhofer AICOS testbed. These modules are designed to harvest energy from four main environmental sources: solar, thermal, kinetic, and radio-frequency (RF). Each harvester is presented with an overview of its architecture and main characteristics, while detailed schematics can be found in the complete LIGHTED system schematic provided in Appendix A and in related publications [15].

3.3.1 Solar Energy

The solar energy harvesting module is based on the **AEM10941** energy management IC, designed to efficiently capture ambient light from both indoor and outdoor PV panels. It integrates a boost converter, low-dropout (LDO) regulators, and a maximum power point tracking (MPPT) controller. The MPPT can be tuned to track around 70–80% of the open-circuit voltage of the PV cell, ensuring optimal efficiency under varying light conditions [10]. External capacitor banks can be attached to provide energy buffering and support for extended operation.

3.3.2 Thermal Energy

Thermal energy harvesting relies on thermoelectric generators (TEGs) exploiting the Seebeck effect. The system employs commercial modules managed by the **AEM20940** IC [8, 9]. The MPPT controller is tuned for high-impedance sources, typically operating at around 50–70% of the open-circuit voltage to ensure efficient energy extraction. Supercapacitors are used as storage elements to smooth intermittent gradients in thermal conditions.

3.3.3 Kinetic Energy

The kinetic harvesting module leverages piezoelectric materials to generate energy from vibrations, paired with an **AEM30940** IC for power management. A secondary implementation uses the LTC3588-1 module [4], which integrates a rectifier and buck converter for improved efficiency. Due to the low and sporadic energy from vibration sources, the harvested power is typically stored in a supercapacitor for short bursts of operation.

3.3.4 RF Energy

RF energy harvesting is achieved with the **P2110B** IC [29] and **AEM-30940** EVK [12], which capture electromagnetic waves (915 MHz and 2.45 GHz respectively). The harvester integrates impedance matching, rectification, and storage, enabling low-power IoT nodes to operate from surrounding RF fields. While efficiency decreases significantly with distance, capacitor-based storage ensures that short bursts of computation and communication remain possible.

3.4 Experimental Setup and Results

This section outlines the procedures and protocols used to evaluate the performance of the energy harvesting modules described previously. The experiments were structured in three main phases. First, initial tests were conducted to ensure safe operating conditions and to validate the functionality of the measurement circuits. Then, each energy harvesting modality was systematically tested in a controlled laboratory environment to assess charging dynamics, energy conversion behavior, and storage performance under standardized stimuli. Finally, a subset of the best-performing harvesters, specifically the 2.45 GHz RF and solar modules, was selected for extended duration

testing to evaluate long-term energy accumulation and stability under realistic ambient conditions. Results from these campaigns form the basis for comparing the suitability of the harvesters for batteryless sensing applications [2, 17, 45].

3.4.1 Initial Tests

The initial experimental phase was exploratory, aimed at helping with the familiarization with the testbed hardware, interface, and harvesters. Tests were performed informally, without rigorous control of variables such as capacitor discharge or environment. Capacitor voltages were not recorded directly, observations were made through the real-time dashboard interface provided with the system.

The goal was to assess how each harvester responded to different inputs and to identify the most promising source (solar, thermal, kinetic, or RF) for future batteryless nodes. At this stage, various capacitor bank configurations were evaluated. The testbed allowed combinations of two supercapacitors (0.47 F and 1.0 F) and eight ceramic capacitors (ranging from 22 µF to 220 µF), resulting in a maximum external storage capacity of 1.47 F + 976 µF. Additionally, each harvester contributed its own internal output capacitor (typically 150 µF), which was factored into total energy storage considerations [15]. The hybrid choice of supercapacitors and ceramic capacitors was motivated by their complementary properties: while supercapacitors provide large bulk storage, ceramics offer low equivalent series resistance (ESR) and faster transient response, helping stabilize the voltage under rapid load changes.

Solar harvesting was initially tested with two outdoor-oriented PV panels (*Iseum 7065* and *IXOLAR KX0B141K06F R3.5*) under both sunlight and artificial illumination using laboratory lamps. The system was configured with the MPPT set to approximately 80% of the open-circuit voltage. This value was chosen because it provides a practical trade-off between tracking efficiency and usable voltage level for storage: PV cells exhibit nonlinear I-V characteristics, and the MPPT ensures operation close to the maximum power point by matching source and load impedances. The 80% setting was empirically tuned for the panels used, which typically present lower effective impedance under laboratory illumination. The panels were positioned in various locations including corridor windows, workbenches, and central laboratory areas, with and without direct light. Performance was visually monitored on the dashboard interface and positioning improvements were found to influence capacitor charging rates substantially.

Thermal energy tests used thermoelectric generators (TEGs), specifically the Marlow TG12-4-01L and GM300-126-11-12-C modules, heated using a hot air gun set to approximately 150 °C at 50% airflow [8, 9]. The MPPT was configured to operate at about 50-70% of the open-circuit voltage, a range that better matches the high source impedance of TEGs. This configuration maximizes power transfer by adapting to the TEGs' weak current delivery capability. To overcome cold-start limitations, the `CS` pin was manually connected to the storage rail. While power peaks near 5 mW were observed, the system was unable to fully charge large capacitor banks during short test windows.

Kinetic harvesting was evaluated using a piezoelectric sensor (MCFT-27T-4.2AL-127) tapped manually or with a small hammer [4]. Tests were performed with only the harvester's internal 150 µF capacitor connected. Mechanical excitation included finger taps and hammer strikes at 1–2 Hz from a drop height of approximately 2 cm. Although voltage spikes up to 4 V were detected, energy transfer was insufficient to charge larger capacitors, confirming the inefficiency of bare piezo setups under low-excitation conditions. This aligns with the intrinsic characteristics of piezoelectric harvesters, where the harvested power strongly depends on resonance tuning and sustained vibration rather than isolated impacts.

RF harvesting used the integrated 915 MHz testbed module, exposed to a 20 dBm RF signal, which after amplification by 14 dB resulted in an effective transmit power of approximately 34 dBm. In the first test, the harvester output was set to 2.5 V (by resistor selection), and only the internal capacitor was used to accelerate charging. In a second test, the 976 µF ceramic bank was connected. The harvester was operated in both harvesting and measurement modes, RF performance was highly sensitive to the distance and orientation between the antenna and transmitter. At the test distance used, energy collection was observed at received power levels around –5.8 dBm [29]. The results highlight how antenna gain, polarization, and placement strongly affect the energy budget of RF-powered nodes.

A second wave of exploratory testing revisited the four modalities under more realistic deployment scenarios, such as indoor lighting and window placement for solar panels. These trials confirmed the strong performance of solar harvesting while underscoring the limitations of kinetic and RF sources without advanced regulation or specialized hardware.

Although loosely structured, these initial tests were instrumental in revealing practical constraints and optimization opportunities across the testbed subsystems. They informed decisions regarding source selection, component matching, and storage sizing for subsequent controlled experiments detailed in Section 3.4.2 [18, 19].

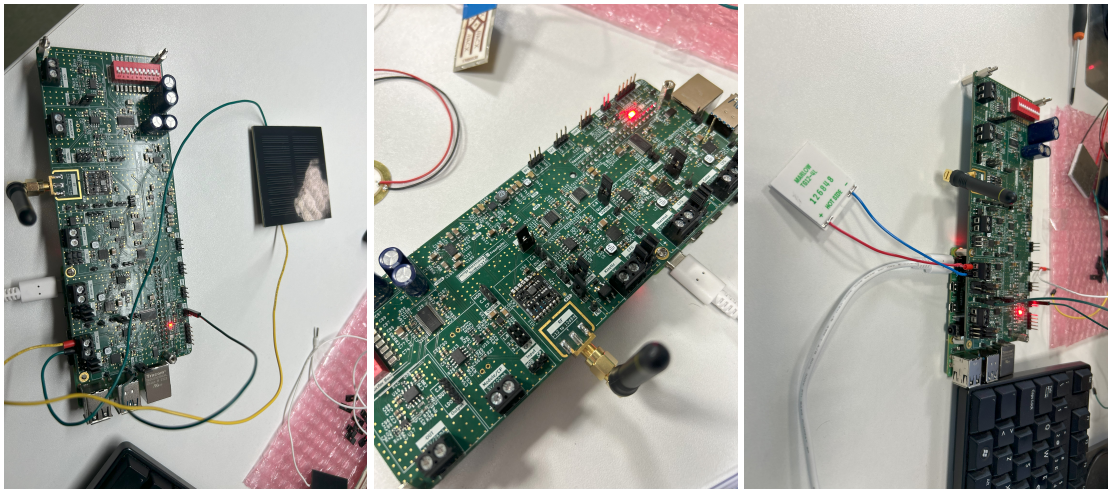

(a) (b) (c)

Figure 3.4: Examples of some of the first experimental setups. Each configuration (solar, RF and thermal) was used to familiarize with the testbed and understand each harvester behavior.

3.4.2 Controlled Environment Tests

After validating safe operating conditions, each energy harvester was tested under standardized laboratory conditions to evaluate and compare energy conversion efficiency and storage performance. Experiments were conducted employing regulated light, thermal, mechanical, and radio-frequency inputs. All storage capacitors were fully discharged to below 50 mV before each run to ensure repeatability [14].

Solar Energy (SW-0.4M Panel)

Tests were conducted using a high-intensity SW-0.4M PV panel under controlled indoor lighting. The AEM10941 was configured at 70% MPPT. Sampling was performed at 10 kHz, and three storage configurations were tested. Measured illuminance values were between 12000 lx and 13000 lx.

The setup is shown in Figure 3.5, and Figure 3.6 shows the input power evolution and capacitor charging. The results demonstrate that while the smallest capacitor (976 µF) charges very quickly, it saturates early and cannot sustain energy for longer periods. In contrast, the larger banks (0.47 F and hybrid 1.47 F + 976 µF) charge more slowly but provide smoother and more stable energy buffering, particularly suitable for longer operation.

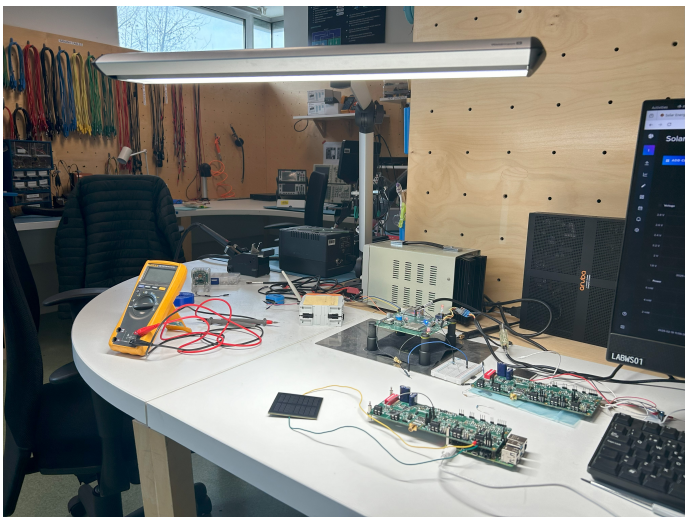

Figure 3.5: Solar test setup with SW-0.4M panel.

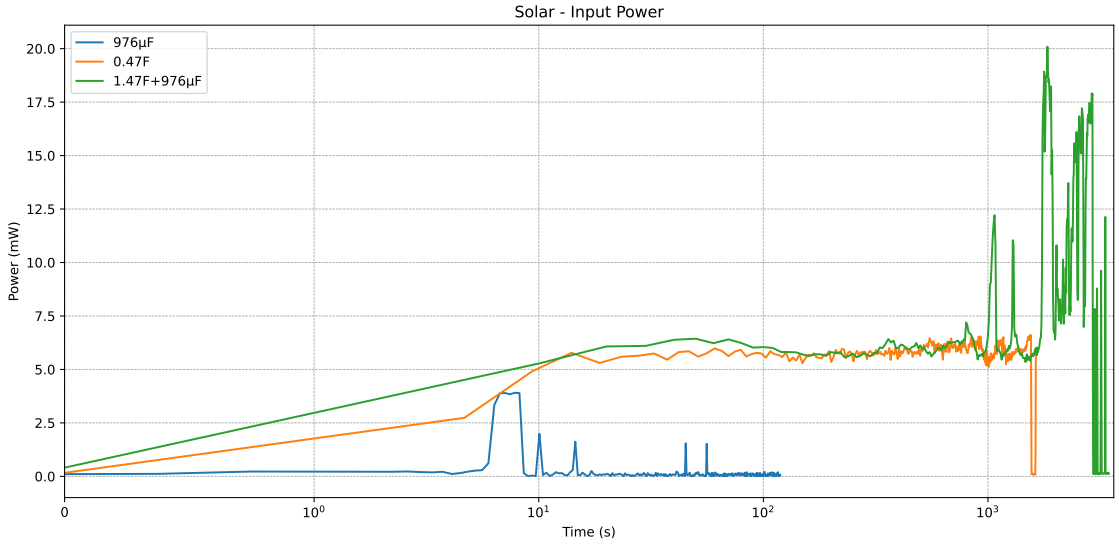

(a) Input power evolution

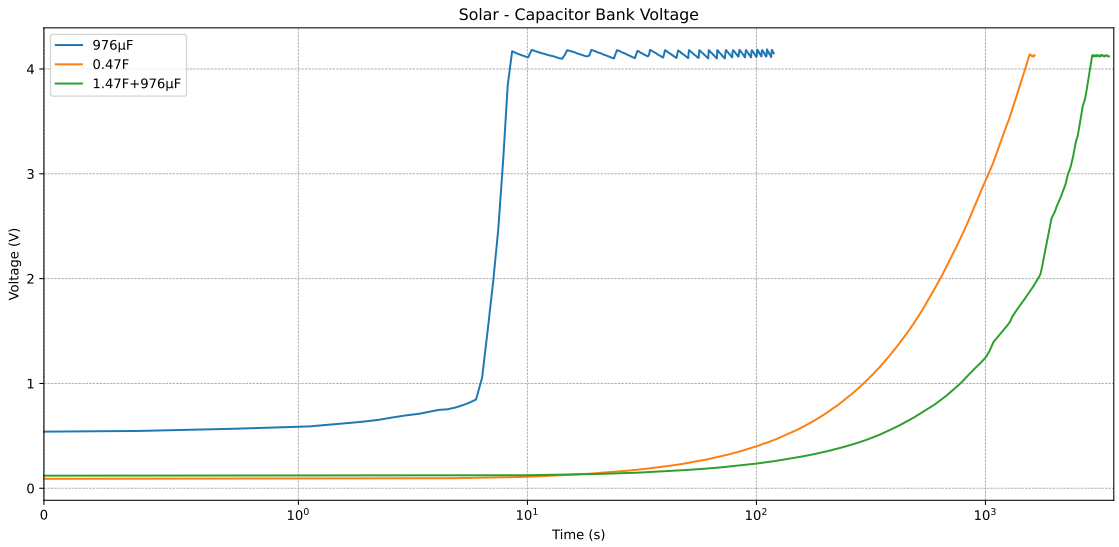

(b) Capacitor voltage during charging

Figure 3.6: Performance of SW-0.4M panel with three storage configurations under indoor controlled lighting. Measurements were conducted at an illuminance level between 12 000 lx and 13 000 lx.

Indoor Solar (LL200 Panels)

Three amorphous silicon PV panels (LL200-2.4-75, LL200-3.6-75, and LL200-3-37) were tested under artificial indoor lighting. The LL200-2.4-75 panel, with dimensions of 94 × 73 mm (active area of approximately 68.6 cm²) and only 0.22 mm thick, was used as the main reference for the Luxor node. The AEM10941 was set to **70% MPPT**, meaning it regulates the panel at 70% of its open-circuit voltage (V_{OC}). This fixed ratio is commonly used since many indoor PV cells reach peak power around 70–80% of V_{OC}. For the LL200-2.4-75 panel, illuminance exceeded 15 000 lx.

The setup is shown in Figure 3.8, and Figure 3.7 shows that indoor panels achieve lower input power compared to SW-0.4M but display highly stable output. Capacitor charging is again fastest for the 976 µF bank, while the larger banks demonstrate longer charging times but higher stability.

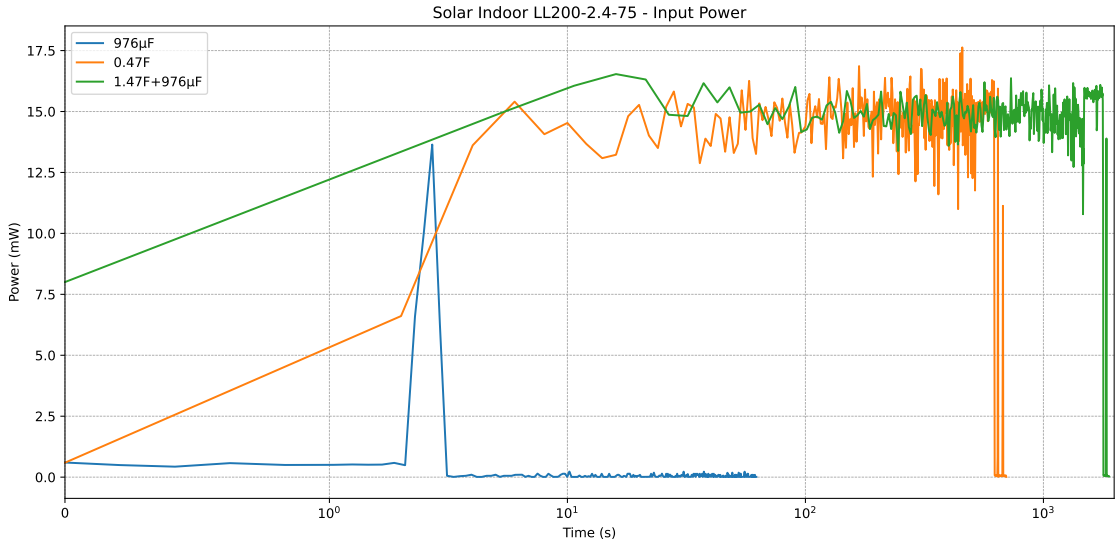

(a) Input power

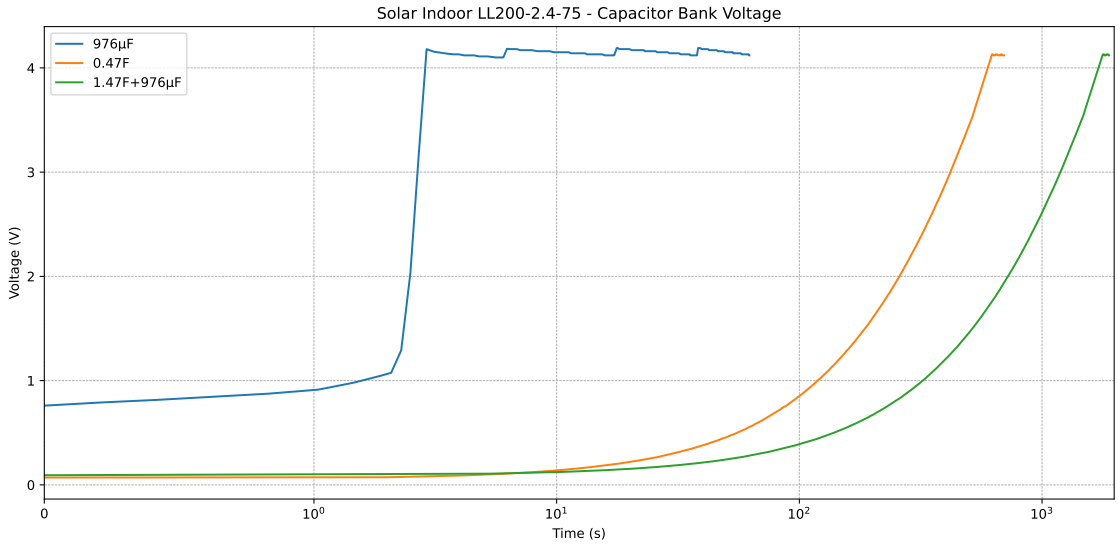

(b) Capacitor bank voltage

Figure 3.7: Performance of LL200-2.4-75 indoor solar panel with three storage configurations under artificial lighting. The AEM10941 was configured at 70% MPPT, and illuminance exceeded 15 000 lx.

Figure 3.8: Indoor solar harvesting using LL200 PV panels.

Thermal Energy (Marlow TG12-4-01L)

Thermal harvesting was evaluated using a TG12-4-01L TEG and the AEM20940 at 50% MPPT. Two heating sources were used: a resistive heater (rated 5 W, 5 V) powered from a source with limits set to 5 V and 2 A, and a hot-air station which operated between 200–250 °C at 30% airflow.

The setups are shown in Figure 3.9, while Figures 3.10 and 3.11 show the input power and capacitor voltages. With resistive heating, input power is relatively stable but low, resulting in slow charging of large capacitor banks. In contrast, the hot-air source produces higher instantaneous power but with significant fluctuations, explaining the uneven charging curves. These results underline the sensitivity of TEGs to thermal gradients and environmental stability.

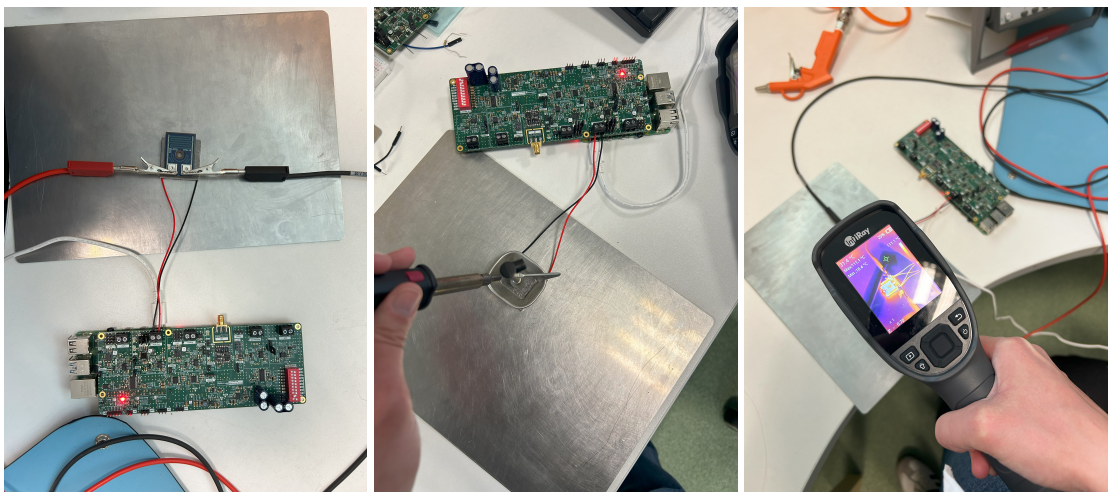

(a) Resistive heater (b) Hot-air source (c) Thermal monitoring

Figure 3.9: Thermal harvesting setup.

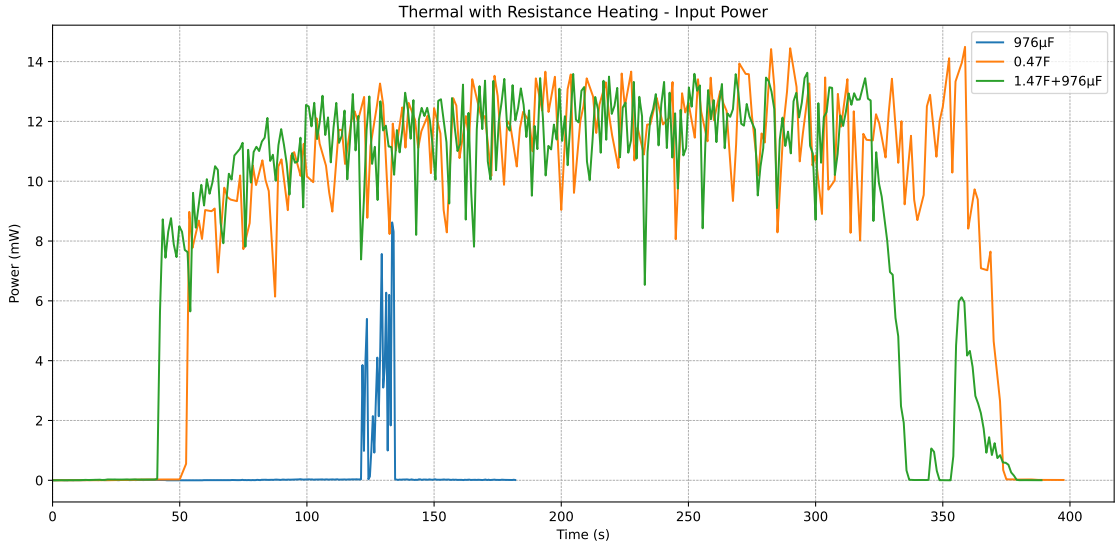

(a) Input power with resistive heating

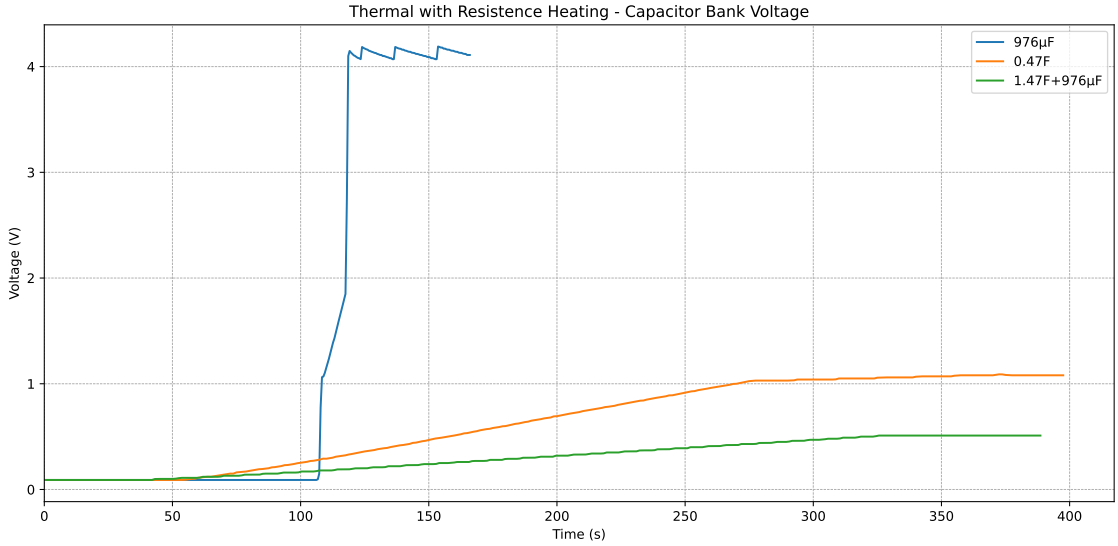

(b) Capacitor voltage

Figure 3.10: Performance of the TG12-4-01L TEG under resistive heating (5 W, 5 V, supply limited to 5 V/2 A).

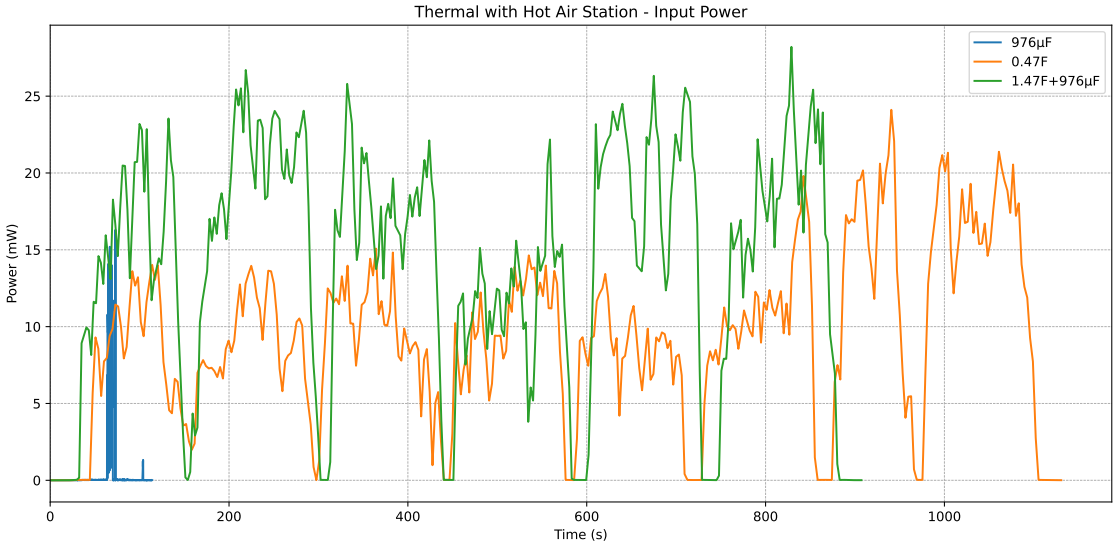

(a) Input power with hot-air source

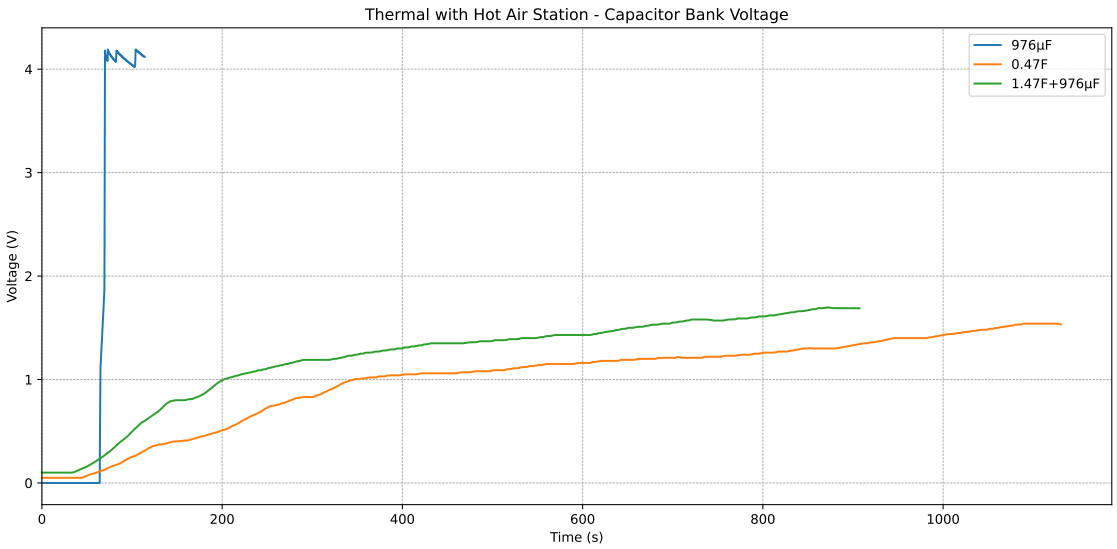

(b) Capacitor voltage

Figure 3.11: Performance of the TG12-4-01L TEG under hot-air stimulation (200–250°C, 30% airflow).

Kinetic Energy Harvesting

The MCFT-27T-4.2AL-127 piezoelectric sensor was excited by manual taps at 1–2 Hz. Only the internal 150 µF capacitor was used. The setup is shown in Figure 3.13, and Figure 3.12 shows sharp voltage spikes with minimal accumulation in the storage capacitor, illustrating the poor efficiency of direct piezo setups.

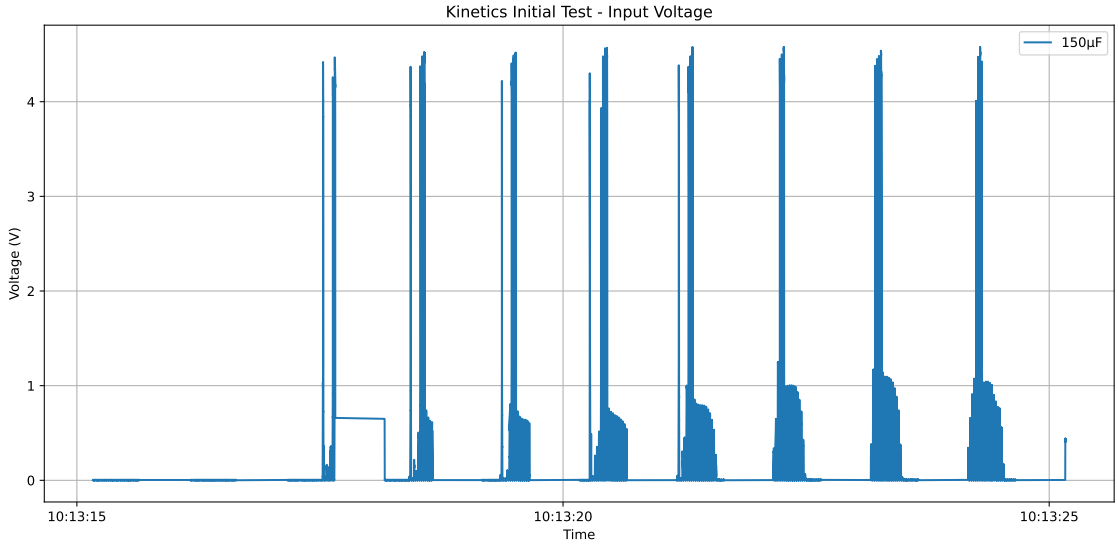

(a) Input voltage spikes

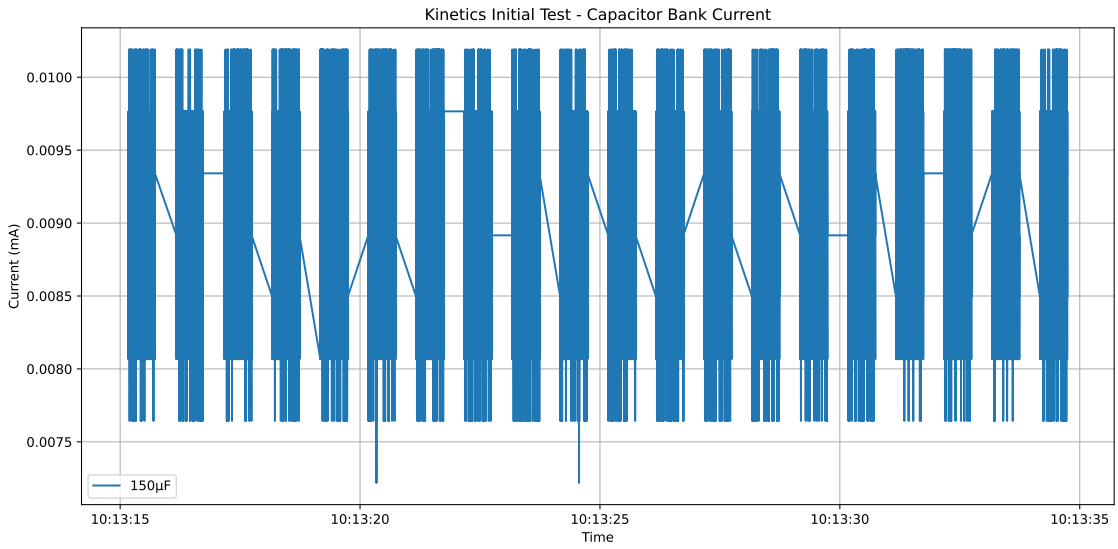

(b) Capacitor bank current

Figure 3.12: Direct piezoelectric harvesting with MCFT-27T-4.2AL-127 under manual tapping at 1–2 Hz.

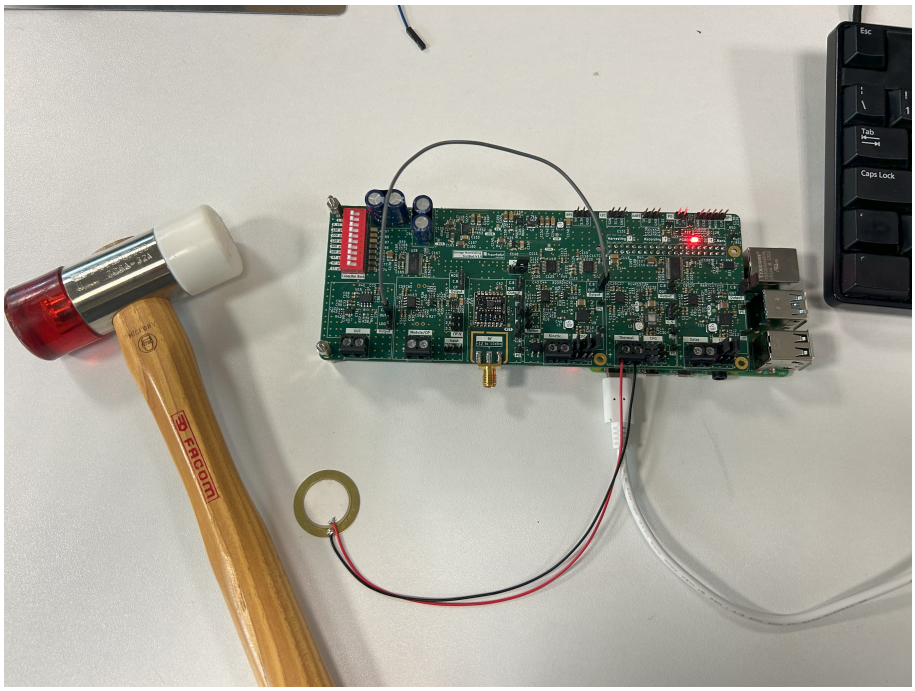

Figure 3.13: Direct piezo excitation setup with MCFT-27T-4.2AL-127 tapped manually at 1–2 Hz.

Using the LTC3588-1 module (with integrated regulation and a 47 µF capacitor), the performance improved significantly. The setup is shown in Figure 3.14, and Figure 3.15 shows that while charging is still slow for large capacitors, extended operation enables gradual accumulation, highlighting the benefit of dedicated conditioning circuits for kinetic harvesters.

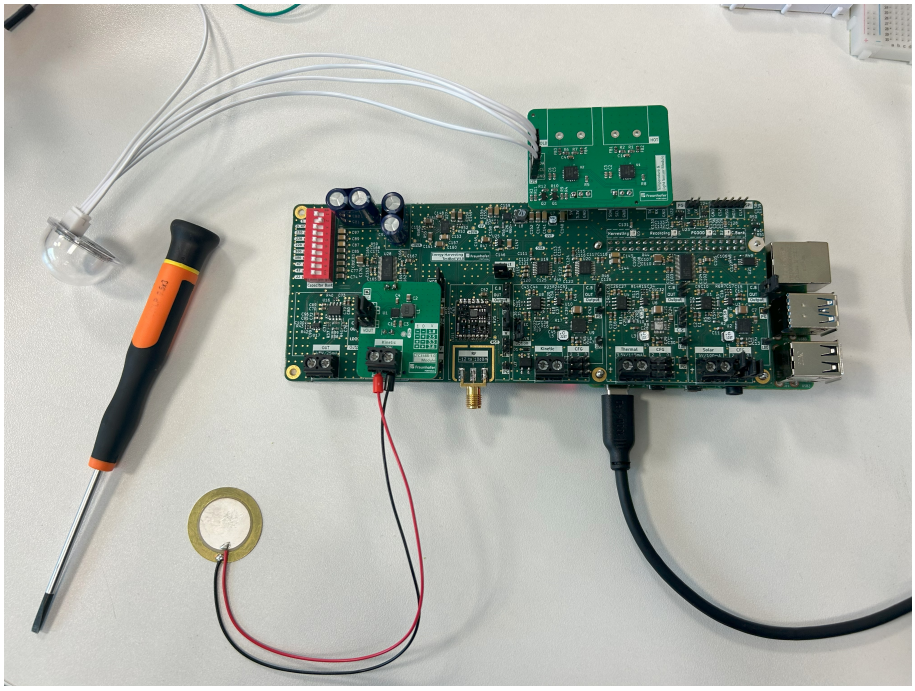

Figure 3.14: Improved kinetic harvesting setup using LTC3588-1 module.

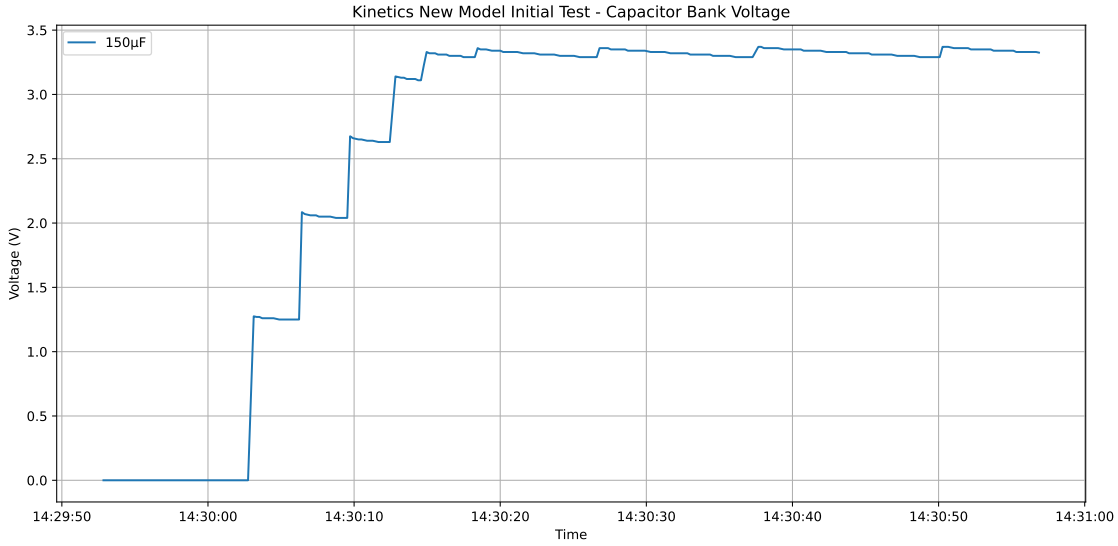

(a) Initial test: 47 µF only

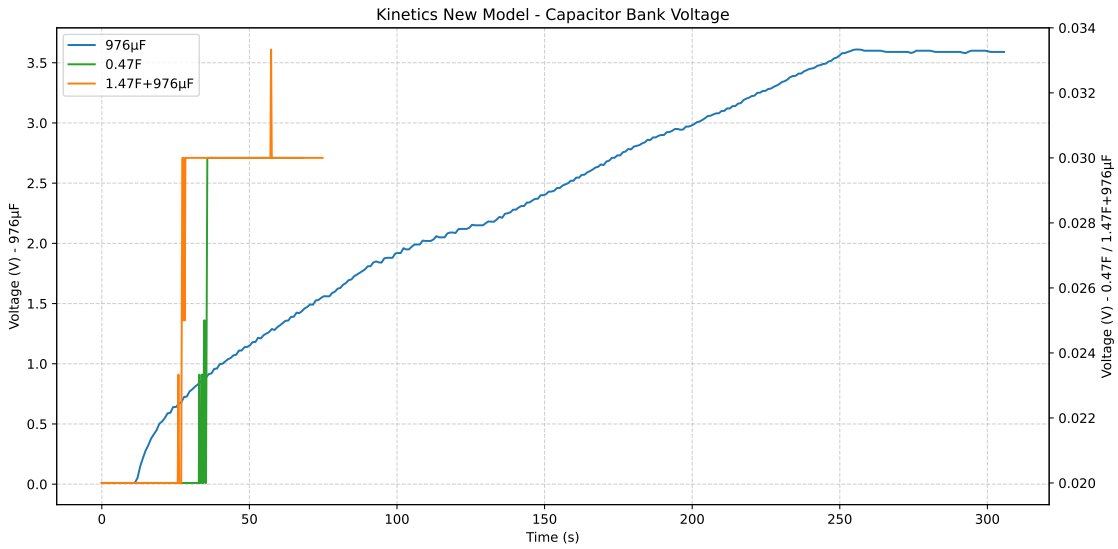

(b) Extended configurations

Figure 3.15: Capacitor charging profiles with LTC3588-1 module under manual tapping (1–2 Hz).

RF Energy Harvesting

Tests were performed for both 915 MHz (P2110B EVK) [29] and 2.45 GHz (AEM30940 EVK) [11, 12] RF harvesters. A 20 dBm signal was transmitted and amplified by 14 dB. The antenna was placed 15–20 cm from the receiver inside a shielded box. For the 915 MHz tests, the received power was approximately –5.8 dBm. The setup is shown in Figure 3.17, and the results are shown in Figure 3.16.

Figure 3.16a shows the measured input power of the 915 MHz module. The unusual offset at the beginning of the trace is due to the moment when the RF source was powered on, which slightly shifted the starting position of the measurement. After stabilization, the received

power remained around –5.8 dBm with some fluctuations caused by antenna alignment inside the shielded environment. Figure 3.16b illustrates the charging performance of the capacitor banks. The smallest configuration (976 µF) was able to charge steadily up to 2.4 V, while larger banks (0.47 F and 1.47 F+976 µF) showed very slow charging due to the limited available input power. This demonstrates the difficulty of sustaining large energy buffers at 915 MHz under the given power conditions.

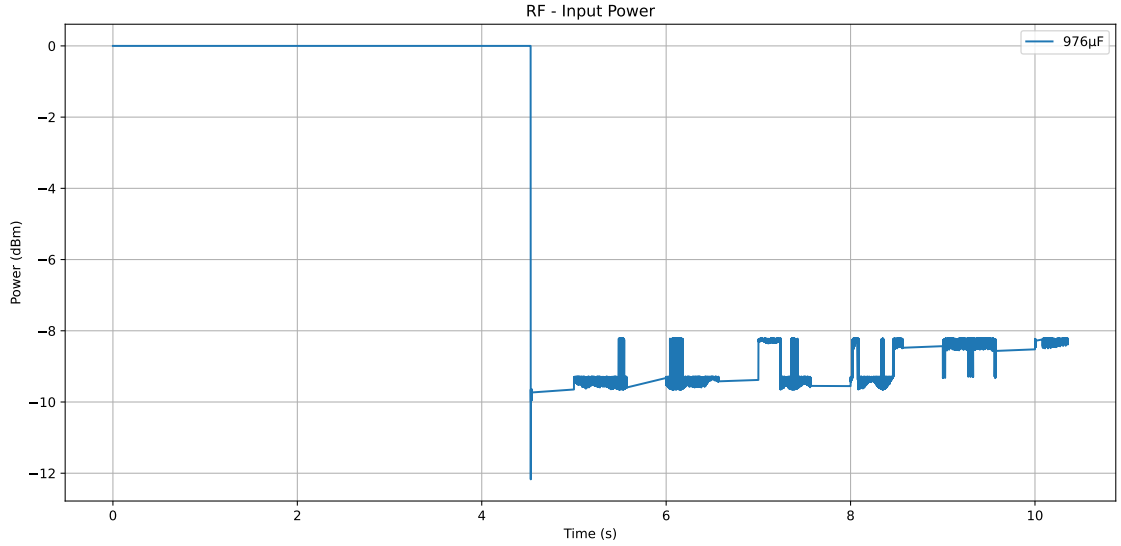

(a) RF input power (915 MHz)

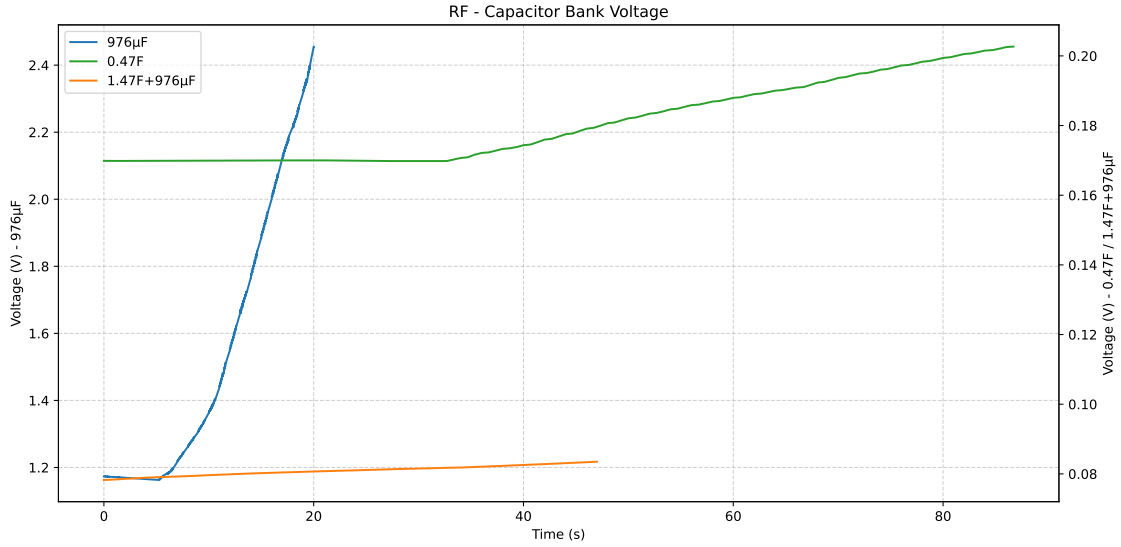

(b) Capacitor bank voltage

Figure 3.16: RF energy harvesting with P2110B at 915 MHz.

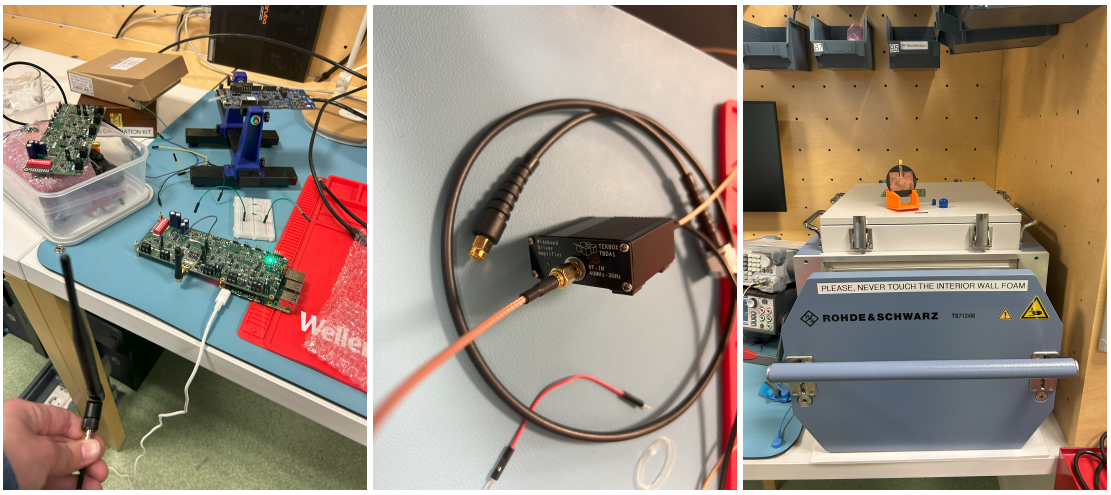

(a) Module placement (b) Signal amplification (c) Shielded box

Figure 3.17: RF harvesting setup.

The 2.45 GHz variant, operating at a lower received power of approximately –10 dBm, is shown in Figures 3.18 and 3.19. Despite the reduced input power, this harvester exhibited more consistent charging behavior across different capacitor configurations. In particular, the smaller capacitors (150 µF and 976 µF) reached full voltage relatively quickly, while the 0.47 F supercapacitor also charged successfully, albeit at a slower rate. This indicates that the 2.45 GHz module can still provide practical energy for low-power IoT devices when paired with appropriately sized storage.

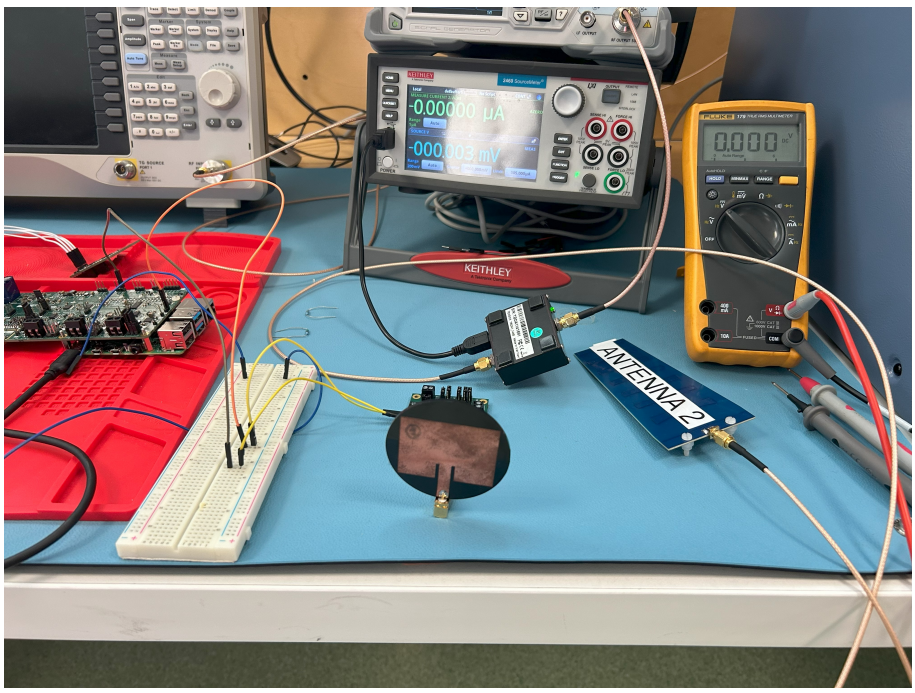

Figure 3.18: 2.45 GHz RF harvesting setup.

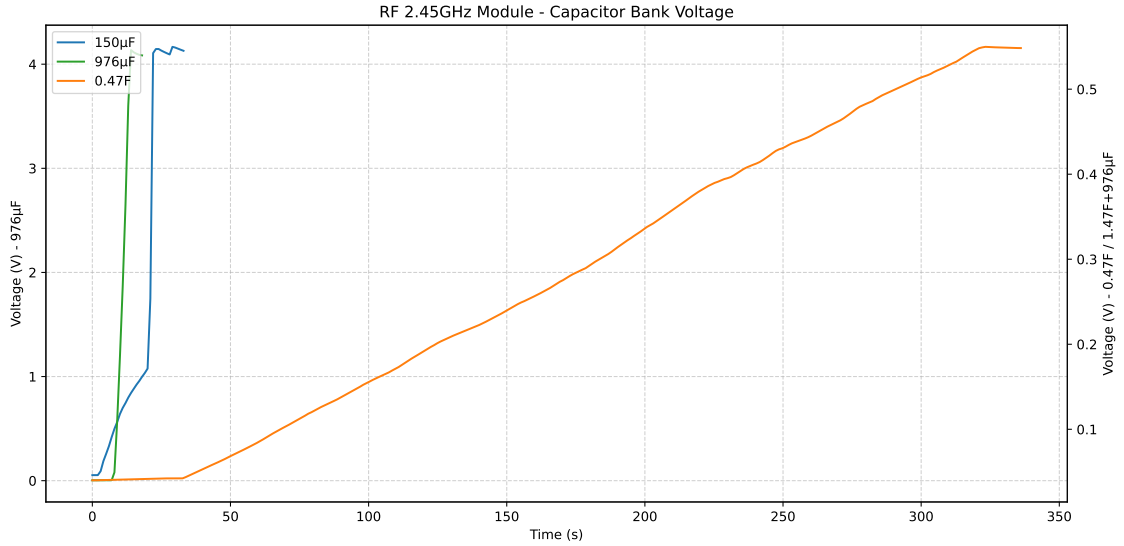

Figure 3.19: Capacitor bank charging profiles of the 2.45 GHz RF harvester.

All tests were concluded when the capacitor bank reached full voltage or energy input plateaued. These controlled trials revealed distinct performance characteristics for each harvester. The solar (SW-0.4M) and RF 2.45 GHz modules demonstrated the most stable and repeatable results and were selected for extended-duration testing campaigns.

Controlled testing revealed distinct performance patterns across the four energy harvesting modalities. Solar energy (especially with the SW-0.4M panel) consistently delivered the highest input power and fastest charging across all storage configurations, both indoors and under artificial illumination. RF harvesting at 2.45,GHz, although operating under lower received power (–10 dBm), demonstrated reliable charging with small capacitors and minimal setup constraints, making it particularly well-suited for embedded, low-power deployments. In contrast, thermal and kinetic harvesters exhibited higher sensitivity to environmental and mechanical variables, often requiring invasive stimulus or prolonged operation for meaningful energy accumulation. Based on these findings, the solar module and the 2.45,GHz RF harvester were selected for extended-duration trials, as they showed the most stable, repeatable, and application-feasible performance for autonomous, batteryless sensor operation.

3.4.3 Extended Duration Testing

Extended-duration evaluations were conducted to assess the long-term viability of energy harvesting systems under realistic deployment conditions. Only the two modalities that demonstrated a positive energy margin in controlled laboratory conditions, namely the indoor solar harvester and the external 2.45 GHz RF rectifier, were selected for this phase. The objective was to determine whether these sources could support perpetual operation of low-power sensor nodes in ambient indoor settings.

The solar tests were performed using the LL200-2.4-75 photovoltaic panel connected to the AEM10941-based energy harvester, while the RF tests employed the standalone 2.45 GHz AEM30940 module. In this setup, the RF harvester was configured with `ENHV` disabled, `ENLV` enabled, and MPPT set in a high-efficiency range as described in the Quick Start Guide of the module [11, 12]. These settings define the usable voltage window and the aggressiveness of energy extraction, enabling rapid startup and controlled charging, but requiring sufficient ambient RF levels to sustain operation. The module was tested only with its internal 150 µF capacitor, without the external storage bank, to evaluate the minimum feasible performance of RF harvesting under realistic indoor conditions.

Three test environments were selected to reflect diverse and representative deployment locations within the building:

- **Electronics Laboratory:** Equipped with ceiling-mounted fluorescent lights operating generally from 07:30 to 19:00, providing limited exposure to natural daylight.
- **Open-Space Office:** A hybrid-lighting setting with south-exposed windows providing varying natural light and overhead fluorescent illumination throughout the workday.
- **Meeting Room 1.11:** Characterized by the lowest light levels, receiving diffuse natural light through a north-facing window and artificial light controlled by an occupancy detection system.

In each environment, the solar harvesting system was tested using two storage configurations: one with a 0.47 F supercapacitor in parallel with a 976 µF ceramic bank, and another with a 1.47 F supercapacitor paired with the same 976 µF bank. In both cases, the system's inherent 150 µF internal capacitor was also present but excluded from reported capacity figures. This setup enabled comparison of charge accumulation rates and plateau voltages as a function of environmental conditions and energy buffering.

Ambient illuminance was monitored using a BH1750 lux sensor placed aligned with the surface of the solar panel. Readings were sampled every 60 seconds to enable correlation with energy harvesting performance. Concurrently, capacitor voltage and current were sampled at 10 kHz using the testbed's analog frontend and streamed to a Raspberry Pi for logging and analysis.

In contrast, the RF harvester, which operated with its internal antenna and no external capacitor, was exposed to the same test environments in parallel with the solar harvester. Following 24-hour exposure periods, the voltage of the internal capacitor of the module was manually measured using a multimeter. Across all environments, no measurable voltage accumulation was observed. This result contrasts with controlled lab scenarios and reflects the substantial attenuation and low ambient RF power available in realistic indoor conditions. For this reason, no time-series plots are presented for the RF module, as its energy yield was effectively null under the test conditions.

The following figures illustrate the test environments and the results for the solar energy modality.

Figure 3.20 shows the testbed deployment in the electronics laboratory. This location was selected for its consistent artificial lighting schedule, offering a stable baseline for evaluating solar harvesting under controlled conditions.

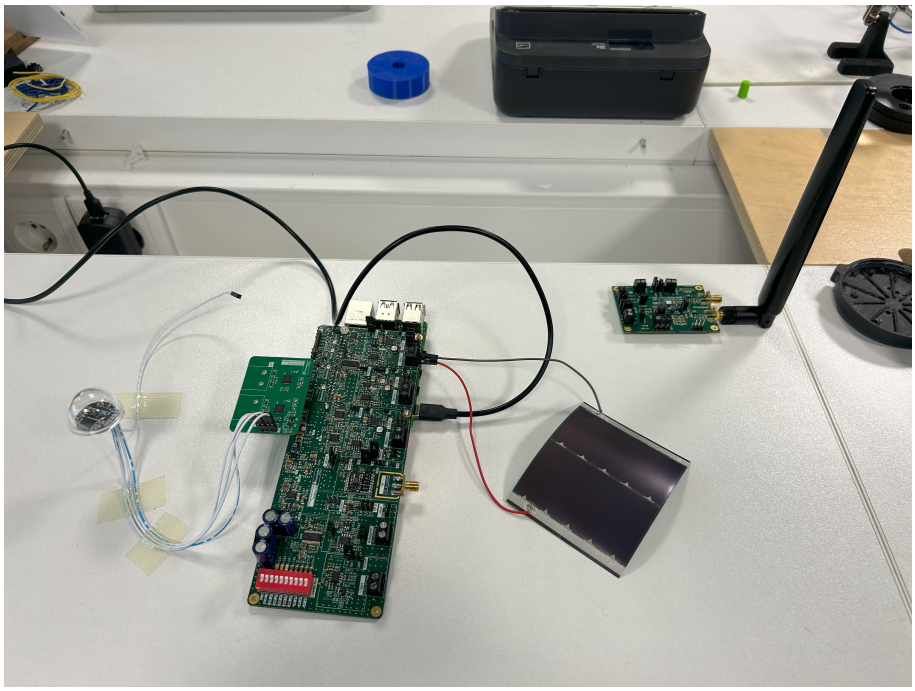

Figure 3.20: Test setup in the electronics laboratory for the 24 hours test.

The collected power and corresponding lux levels, as well as the trend of the capacitor voltage, are shown in Figures 3.21a and 3.21b, respectively. The plots show that during the daytime, the capacitor charges steadily, reaching over 4 V by the end of the cycle, while lux variations track the artificial lighting pattern. Small fluctuations in the power trace correspond to momentary light variations caused by occupancy and switching transients.

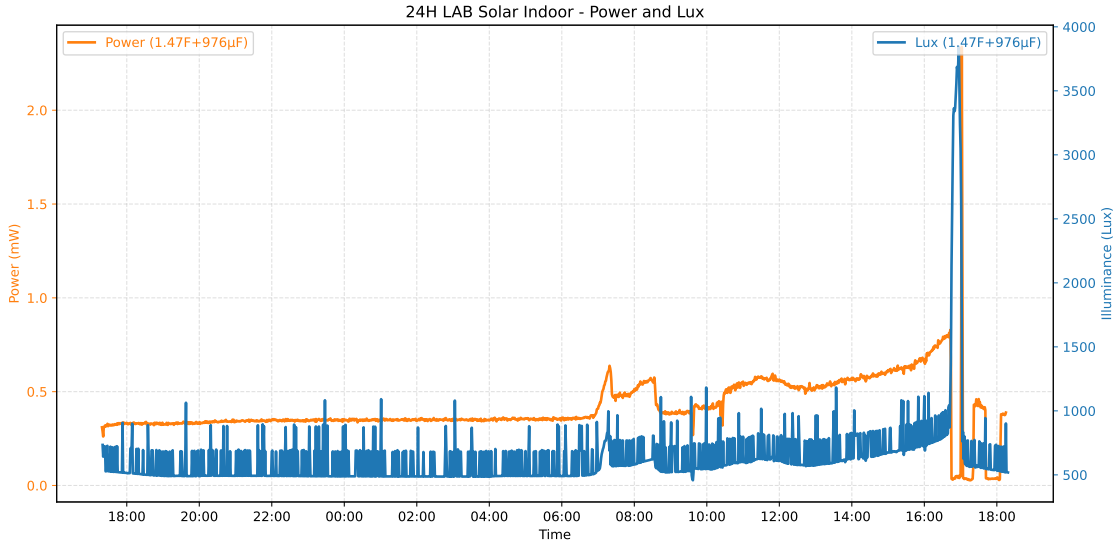

(a) Input power and corresponding illuminance measured over 24 hours in the laboratory.

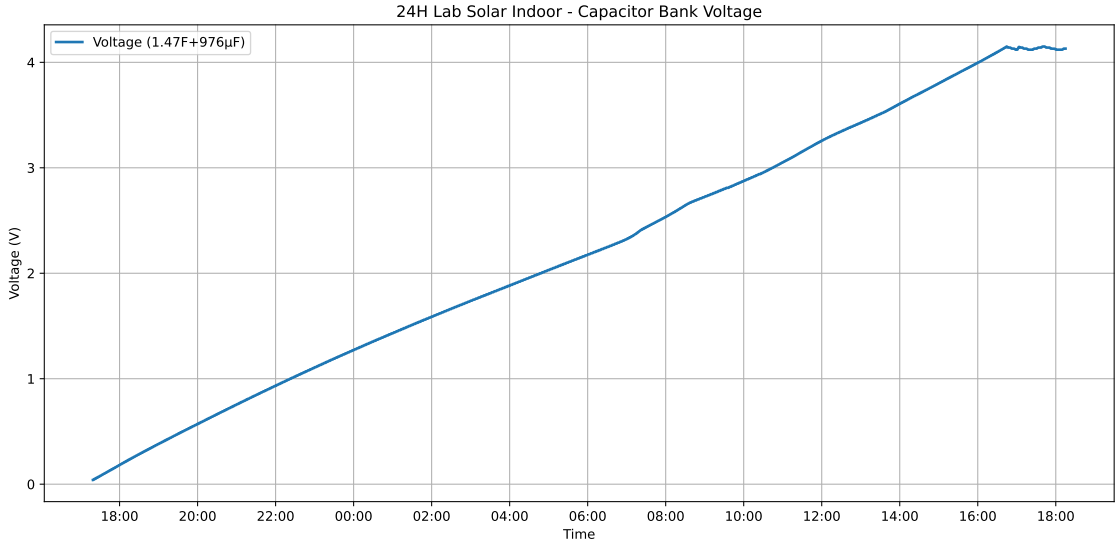

(b) Capacitor bank voltage evolution.

Figure 3.21: Performance of the indoor solar harvester in the laboratory over a 24-hour period.

A second run in the laboratory (Figure 3.22) highlights a different storage configuration. Here, the capacitor bank saturates more quickly, reaching 4 V early in the test. Once charged, the system maintains a near-constant voltage despite lighting fluctuations, demonstrating that the selected supercapacitor bank can buffer short-term variability effectively.

A second run in the laboratory (Figure 3.22) highlights a different storage configuration. Here, the capacitor bank saturates more quickly, reaching 4 V early in the test. Once charged, the system maintains a near-constant voltage despite lighting fluctuations, demonstrating that the selected supercapacitor bank can buffer short-term variability effectively. It is also worth noting that during some intervals, the plots show nonzero harvested power even when the illuminance trace reports

nearly zero. This apparent discrepancy is explained by the different sensitivity thresholds of the devices: the BH1750 lux sensor only provides reliable measurements above 1 lux [32], whereas the AEM10941 energy harvester can cold-start from as little as 380 mV and operate with input power levels as low as 3 µW [10]. Consequently, in very dim conditions the lux sensor reports zero, while the harvester still manages to extract micro-watt levels of power, highlighting its capability to operate in environments below the measurable range of the light sensor.

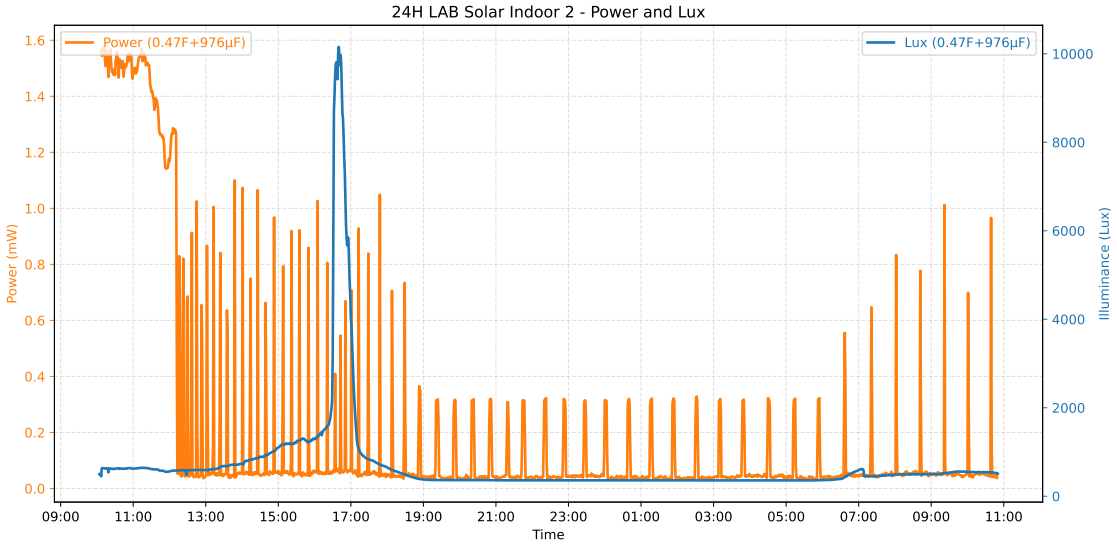

(a) Input power and illuminance over 24 hours in the laboratory.

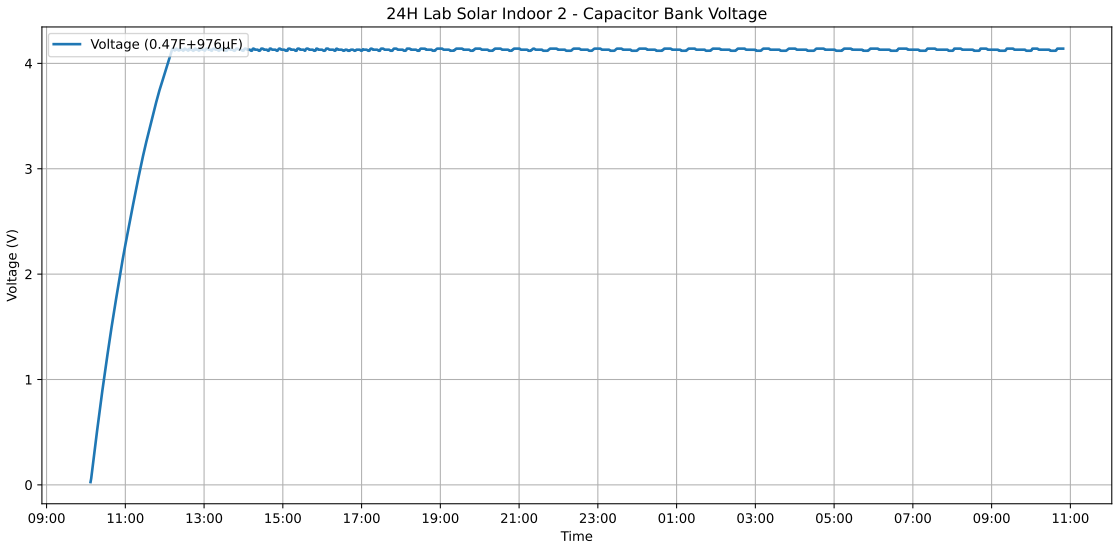

(b) Capacitor bank voltage evolution.

Figure 3.22: Performance of the indoor solar harvester in the laboratory during a second 24-hour run with an alternative storage configuration.

Figures 3.23 show the test setup in the open-space office. This environment provided higher illumination variability due to a combination of artificial and natural lighting.

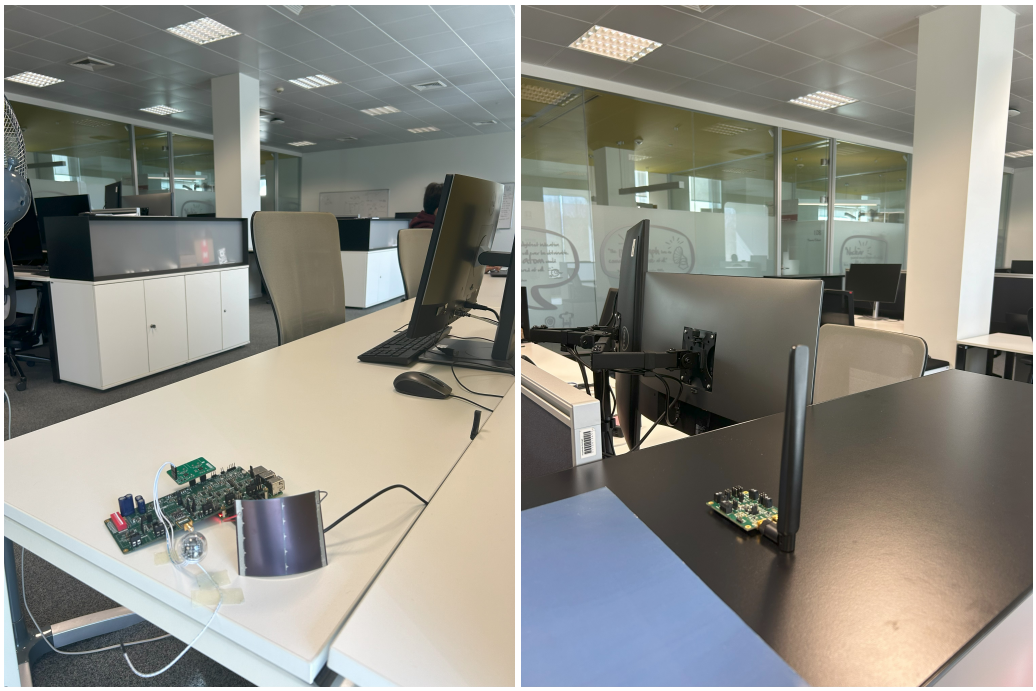

(a) (b)

Figure 3.23: Open Space Setup for the 24-hour test.

Figures 3.24a and 3.24b show that the harvested power follows the large fluctuations in lux caused by the alternation of daylight and artificial light. Despite these variations, the capacitor still charges to over 4 V, though the charging profile shows a plateau during periods of reduced illumination, recovering rapidly when sunlight is present.

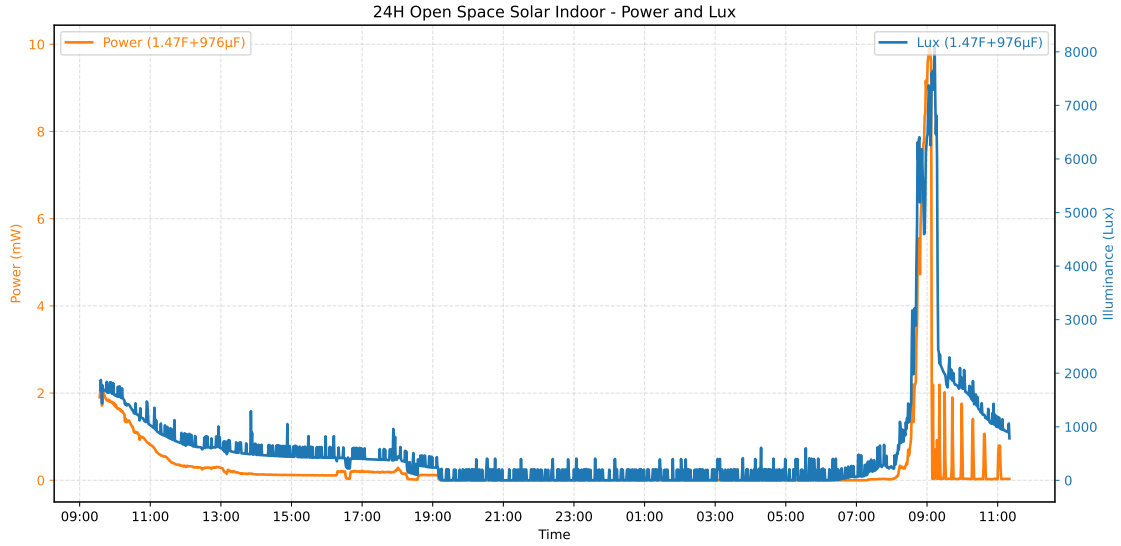

(a) Input power and illuminance over 24 hours in the open space.

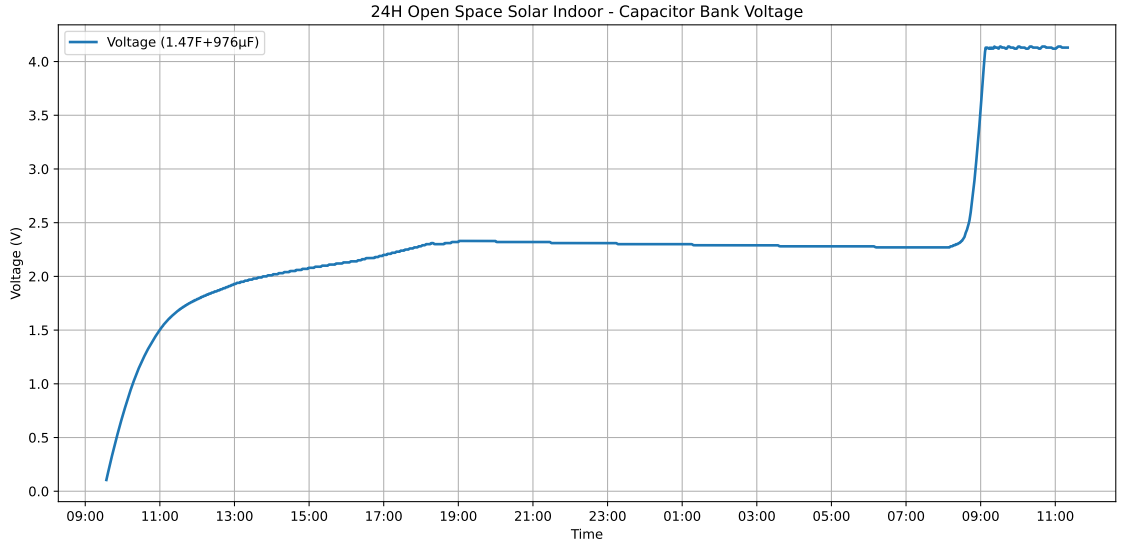

(b) Capacitor bank voltage.

Figure 3.24: Performance of the indoor solar harvester in the open-space office during a 24-hour run, with strong lux variability due to combined natural and artificial lighting.

A second test in the open space (Figure 3.25) shows a similar trend, where capacitor charging slowed overnight due to the absence of light but quickly resumed with the morning increase in illuminance, confirming the robustness of solar harvesting in hybrid lighting environments.

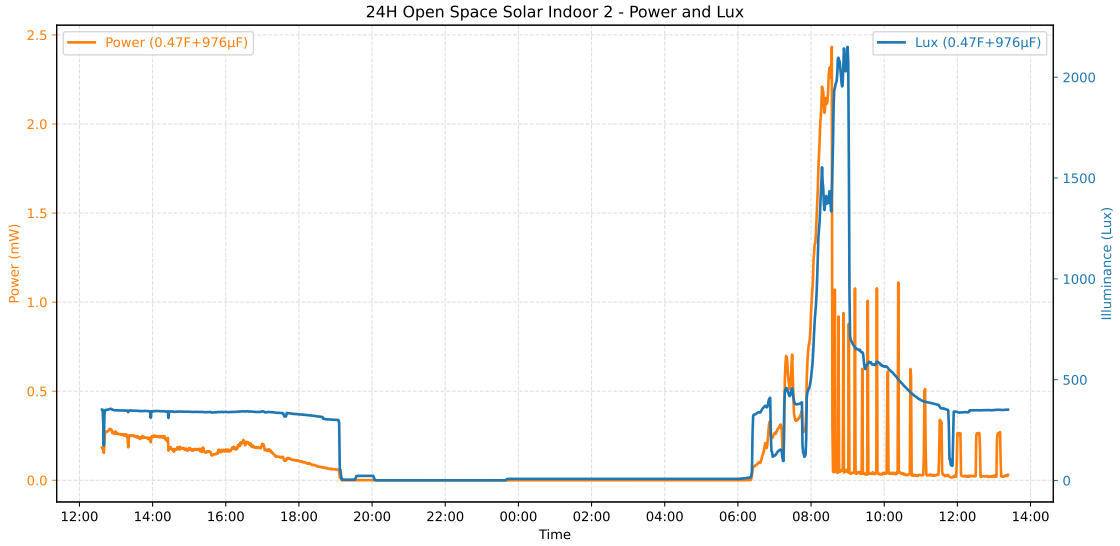

(a) Input power and illuminance during the second open space test.

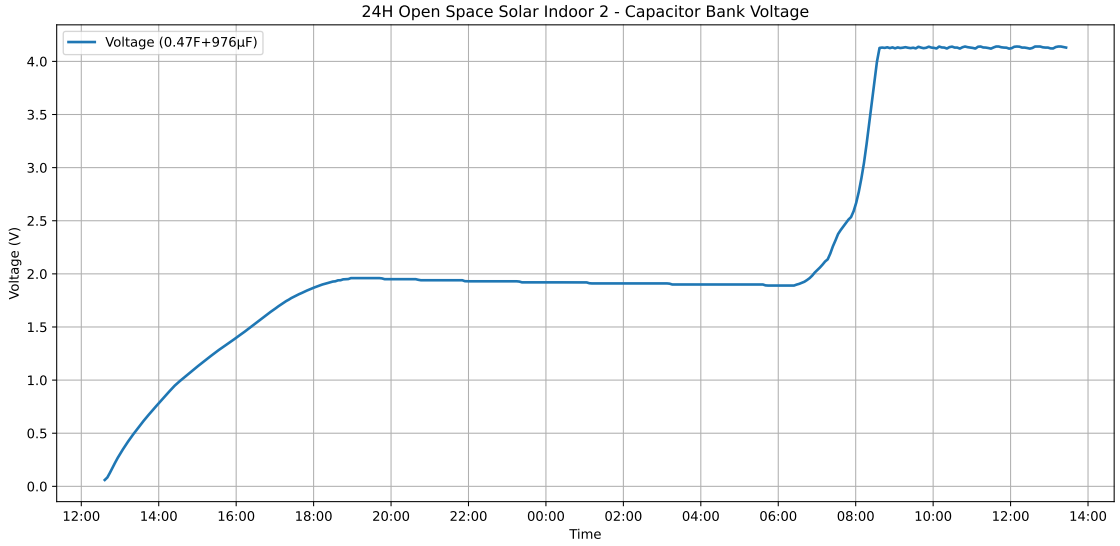

(b) Capacitor bank voltage evolution during the second open space test.

Figure 3.25: Performance of the solar harvester in the open-space office during a second 24-hour run, highlighting stable operation despite strong illumination cycles.

Additional tests were performed in Meeting Room 1.11, illustrated in Figure 3.26, a location that offered the most cautious testing conditions because of inadequate and uneven lighting.

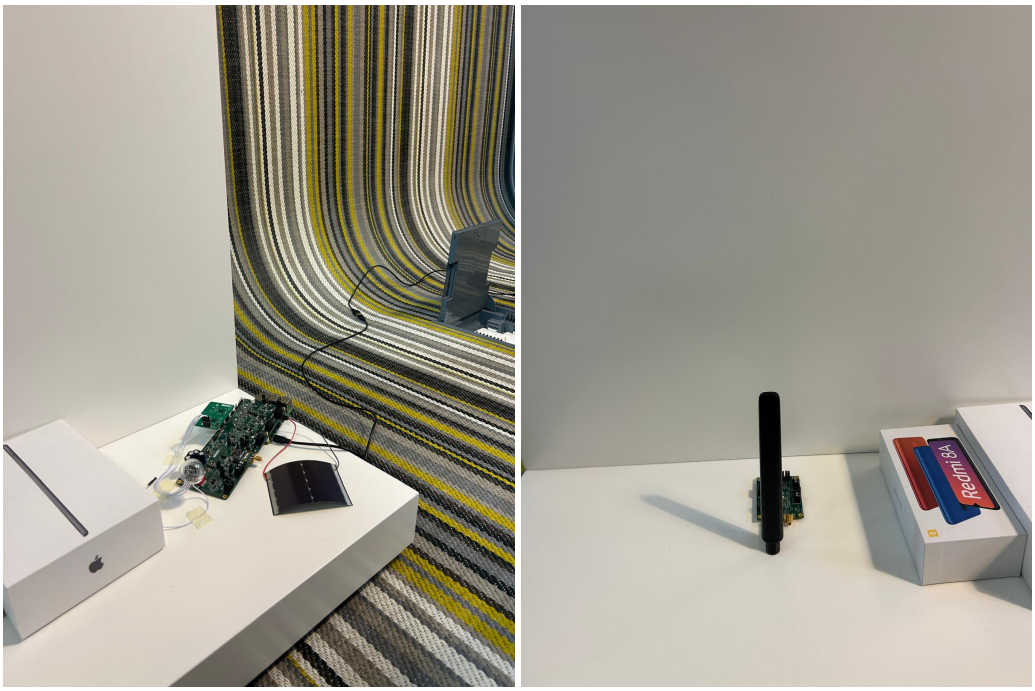

(a) (b)

Figure 3.26: Meeting Room Setup for the 24 hours test.

Figures 3.27a and 3.27b highlight the challenges of harvesting in such low-light conditions. The lux levels rarely exceeded 800 lx, leading to very low harvested power below 0.2 mW. As a consequence, the capacitor voltage increased very slowly, reaching only around 0.6 V after 24 hours. These results confirm that in energy-constrained environments, supplementary sources or duty-cycled operation would be necessary to maintain functionality.

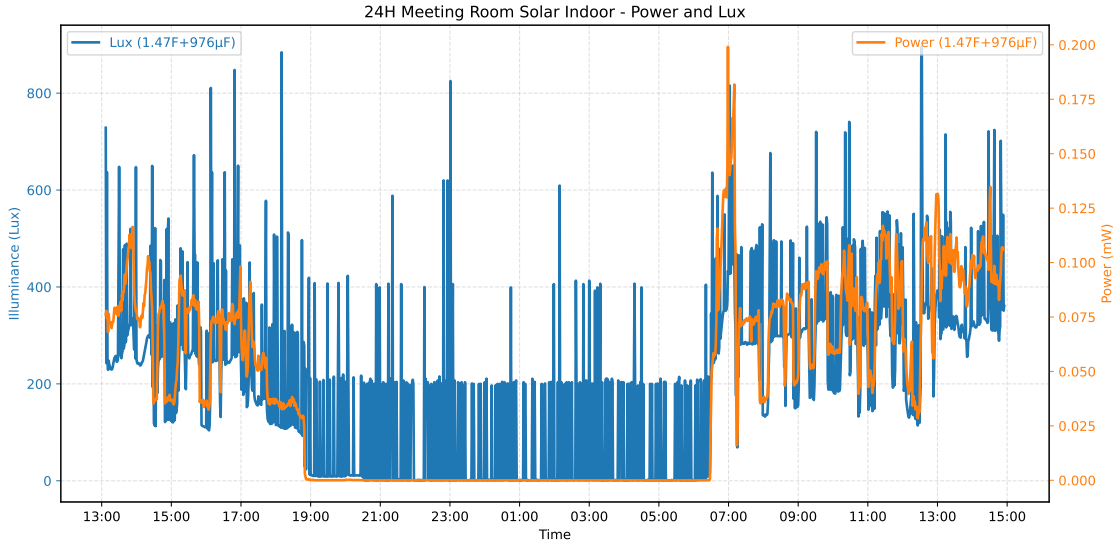

(a) Input power and illuminance during the meeting room test).

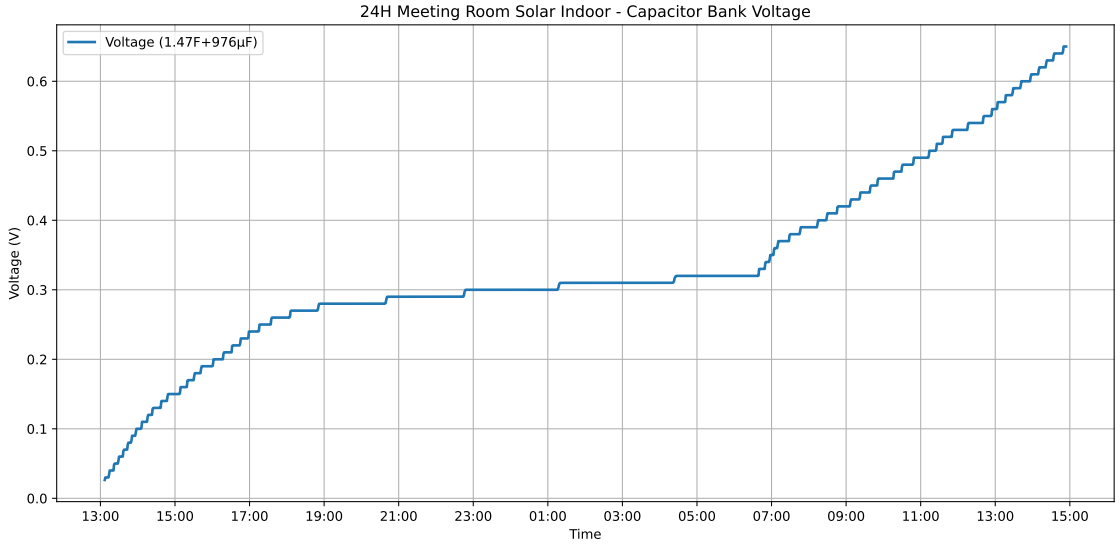

(b) Capacitor bank voltage rise over 24 hours in the meeting room.

Figure 3.27: Performance of the solar harvester in Meeting Room 1.11, demonstrating the limitations of energy harvesting in low-light, energy-constrained environments.

These results confirm the suitability of indoor solar energy harvesting as the main option for powering low-energy sensor functionality in real-world settings. The lack of RF energy accumulation under identical conditions emphasizes the significance of aligning the energy type with the specific deployment scenario.

3.5 Performance Interpretation and Comparative Analysis

This section presents the quantitative outcomes of the experimental procedures described in Section 3.4. Results are analyzed to characterize the performance of each energy harvesting modality

(solar, thermal, kinetic, and radio frequency (RF)) in varying environmental factors and storage configurations. Particular emphasis is placed on the impact of energy input conditions, harvester configuration, and capacitor size on charging efficiency and energy accumulation.

The data is structured to reflect the three test phases: initial exploratory evaluations, controlled laboratory tests, and extended duration measurements in real-world deployment settings. Comparative insights are drawn across modalities, culminating in a discussion of the long-term feasibility of batteryless operation. Only harvesters that demonstrated practical viability during the controlled tests advanced to long-term testing, including the LL200-2.4-75 indoor solar panel and the external 2.45 GHz RF module. Their selection was based on their superior energy yield, stability, and compatibility with indoor IoT deployment scenarios. The subsequent analysis provides a foundation for informed selection and deployment of ambient-powered systems.

3.5.1 Initial Testing Observations

During the initial, informal tests, solar harvesting consistently exhibited the most promising results, particularly under direct or high-intensity lighting. Rapid voltage increases were observed in the dashboard interface, especially when optimal panel orientation and when certain configurations were applied. Thermal harvesting generated noticeable voltage rises only with substantial temperature differentials, and even then required cold-start overrides. Kinetic and RF modalities yielded minimal energy unless exposed to aggressive stimulation or external RF injection. These observations informed the decision to prioritize solar and RF for more rigorous evaluation.

3.5.2 Controlled Testing Insights

Controlled environment testing provided a detailed assessment of harvester efficiency across repeatable and quantifiable conditions. Among the four energy modalities, solar consistently delivered the highest energy throughput. The SW-0.4M panel under artificial lighting conditions achieved full charge on both medium and large capacitor configurations (C_2 and C_3), with predictable input power profiles (Figures 3.6). The LL200-2.4-75 indoor panel, representative of practical deployment conditions, also demonstrated reliable performance with capacitor voltage steadily increasing in line with illuminance levels (Figure 3.7).

Thermal harvesting showed adequate conversion only when subjected to forced heating using hot-air guns or resistive heaters. While input power could be significant under ideal conditions (Figures 3.10, 3.11), energy transfer to storage capacitors was sluggish and plateaued at lower voltages, indicating losses in the conversion process and a mismatch between harvester characteristics and real-world availability of thermal gradients.

Kinetic energy harvesters, especially bare piezoelectric elements, suffered from poor coupling to usable energy. Direct excitation generated high-voltage spikes but negligible current (Figure 3.12). Even with the LTC3588-1 circuit, only small storage capacitors reached usable voltage levels (Figure 3.15). These results confirm that piezo-based kinetic systems are unsuitable for applications lacking constant mechanical vibration.

RF energy harvesting was mixed. The 915 MHz integrated module achieved limited charging when placed in a shielded box with a strong nearby source (–5.8 dBm). The 2.45 GHz module, however, demonstrated meaningful charging under the same test conditions, especially with smaller capacitor banks (Figure 3.19). This relative success supported its selection for extended-duration testing alongside the solar module.

3.5.3 Long-Term Energy Accumulation

The extended-duration trials confirmed the suitability of the LL200-2.4-75 solar module as a sustainable energy source in all three test environments. In the electronics laboratory (Figure 3.20), a stable illumination schedule led to regular capacitor charging cycles. Within the open-space office and Meeting Room 1.11, the system adjusted to a more dynamic lighting scenario, while still showing steady voltage gains throughout 24-hour periods (Figures 3.24, 3.27).

Conversely, the 2.45 GHz RF harvester failed to accumulate measurable voltage under ambient indoor conditions. Its internal 150 µF capacitor showed no noticeable charge after 24 hours. This clear difference from controlled experiments emphasizes the considerable reduction of RF energy in real-life environments and validates its impracticality for wireless energy harvesting without being close to a powerful source.

3.5.4 Comparative Analysis and Summary

Each harvester demonstrated distinct performance characteristics under equivalent testing regimes:

- **Solar** exhibited the highest consistency, scalability, and compatibility with typical indoor environments. Both panels tested were successful, with LL200-2.4-75 being better suited for low-light conditions.
- **Thermal** harvesting was only effective under artificial and invasive stimuli, unsuitable for autonomous sensor operation.
- **Kinetic** energy harvesters failed to produce sustained charging, except in exaggerated excitation scenarios.
- **RF** showed potential in controlled proximity tests but proved impractical under ambient exposure.

Based on these findings, the LL200-2.4-75 solar panel and the 2.45 GHz RF harvester were selected for extended testing. Ultimately, only solar energy harvesting demonstrated real-world viability for continuous, batteryless sensor operation, affirming its role as the primary candidate for deployment in indoor IoT applications.

Chapter 4

Platform Development and Evaluation

This chapter presents the design, evaluation, and comparison of two low-power platforms intended for batteryless sensing applications: the Riotee and IN100-based platforms. The chapter outlines the architecture of each solution, including the corresponding energy-aware strategies, current consumption benchmarks, and 24-hour energy autonomy trials. All tests were performed with harvesting modules and capacitor banks validated in previous chapters.

To provide a clearer understanding of what is meant by "platform" in this context, Figure 4.1 illustrates the Riotee platform. This example highlights the typical structure of the boards evaluated in this chapter, which integrate computation, communication, and power management components into a compact form factor suitable for batteryless operation.

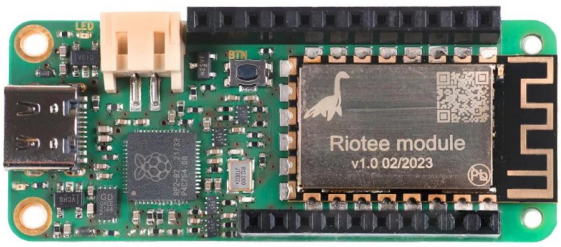

Figure 4.1: Riotee platform used as one of the representative batteryless sensing platforms.

4.1 Experimental Bench

All tests were conducted using the Fraunhofer AICOS testbed, which enabled repeatable ambient energy experiments under controlled and real-world conditions. For current measurements, the Nordic Power Profiler Kit II was used with sampling rates above 10 kHz. Capacitance banks and harvesters were connected according to configurations described in Chapter 3.

4.2 Riotee Platform

4.2.1 Hardware and Firmware Architecture

The Riotee platform combines Nordic's nRF52833 SoC with a custom energy management and memory controller, enabling checkpoint-based execution [25, 26]. Its architecture includes logic for voltage monitoring, automatic shutdown, and resume based on thresholds. Firmware is structured in modules with interrupt-driven energy-aware scheduling and persistent memory.

Riotee enables features such as:

- Energy-aware checkpointing using flash memory [18, 19].
- Stack partitioning and program counter storage.
- Automatic recovery after energy loss.

Despite these capabilities, this complexity introduces significant energy overhead and may be overkill for the intended application: periodic sensing and reporting with minimal computation.

4.2.2 Step-by-Step Energy Consumption

A detailed current analysis was performed by profiling the Riotee platform across the main firmware execution steps. The measurement setup relied on the Nordic Power Profiler Kit (PPK2) to capture fine-grained current traces under controlled harvester-equivalent input. The power routing of the Riotee breakout board, the connection scheme to the profiler, and the final laboratory bench setup are shown in Figures 4.2, 4.3 and 4.4.

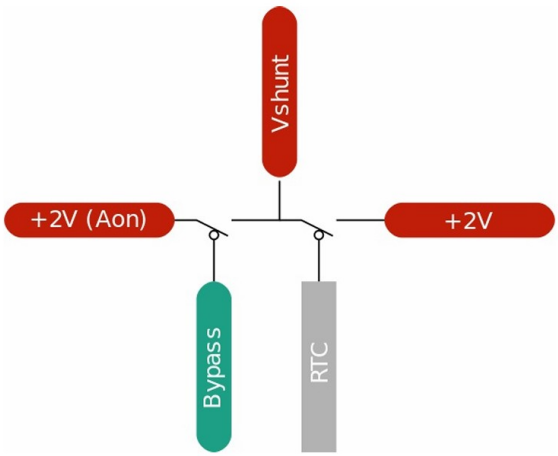

Figure 4.2: Internal power routing of the Riotee breakout board. The measurement shunt (`Vshunt`) isolates the `2V(A)` domain, with bypass and RTC paths selectable through internal switches.

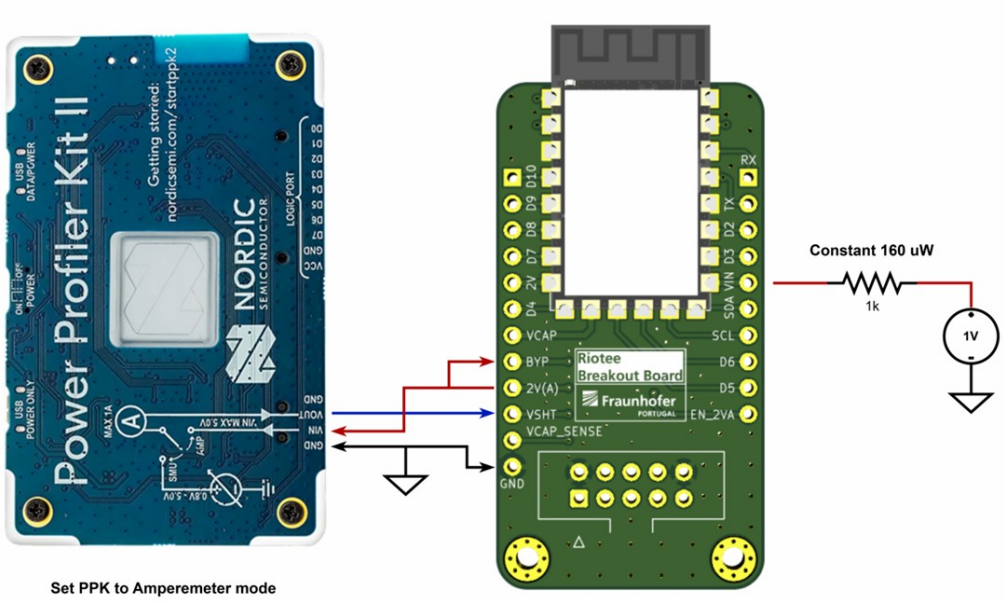

Figure 4.3: Connection of the Riotee breakout board to the Power Profiler Kit II (PPK2) in ammeter mode. A resistive source provides a constant 160 µW input.

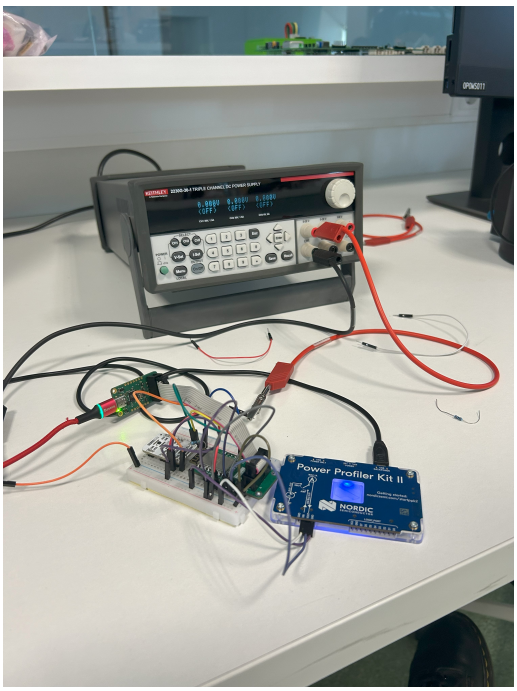

Figure 4.4: Physical test bench used for Riotee current profiling.

The firmware was structured into recurring operations, hereafter referred to as *steps*:

- **Step 1 – BLE initialization and sensor activation**: establishes the BLE link and enables the temperature sensor. Avg. current ∼3.7 mA for 65 ms (max 110 mA).

- **Step 1.1 – Capacitor charge wait**: system idles to allow the supercapacitor to recharge. Avg. current ∼3.6 mA for 65 ms.
- **Step 2 – BLE configuration and sensor read**: performs BLE settings and ADC sampling. Avg. current ∼3.5 mA for 65 ms (max 127 mA).
- **Step 3 – Temperature change detection**: applies threshold logic. Avg. current ∼3.8 mA for 66 ms (max 134 mA).
- **Step 4 – Checkpoint and thresholds**: writes system state to flash memory. Avg. current ∼56 μA over 1 s, with peaks up to 170 mA.

Figure 4.5 shows the current trace across multiple cycles. Short, sharp peaks correspond to sensor and BLE routines, while longer peaks reflect the flash-intensive checkpointing phases.

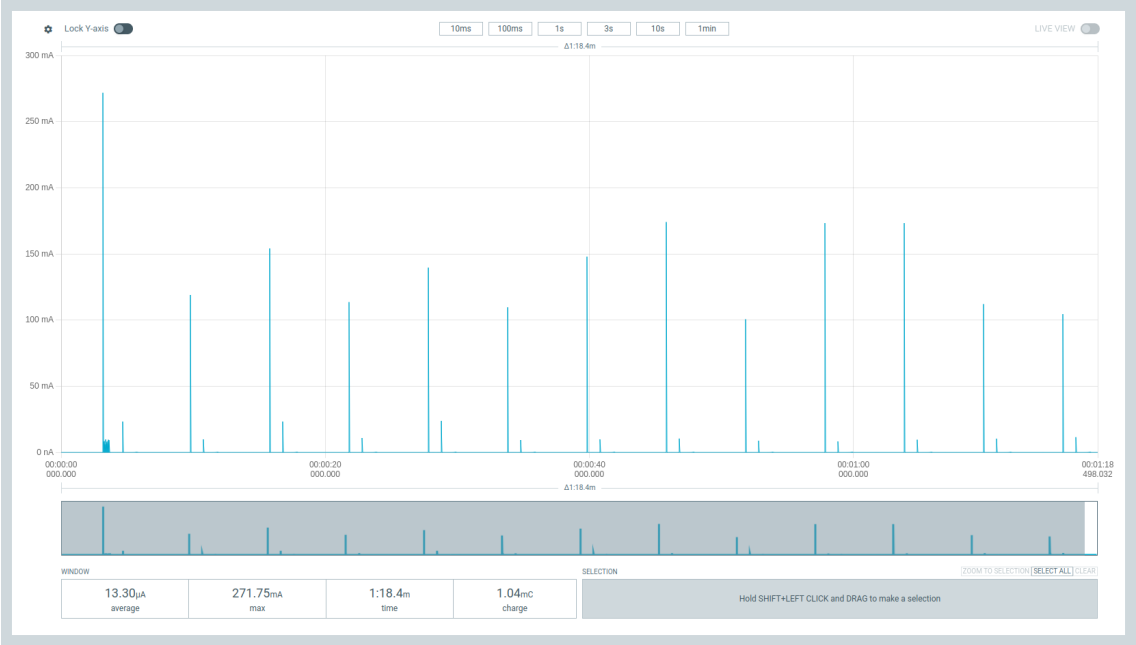

Figure 4.5: Current draw of Riotee operations (Steps 1–4) under a 1.6 V, 0.3 mA supply.

Table 4.1 summarizes the average, maximum, and duration values extracted from repeated measurements.

Table 4.1: Summary of measured current consumption per firmware step (averaged over 10 cycles).

Step	**Avg. Current (μA)**	**Max (mA)**	**Duration (ms)**
Step 1 (BLE init + sensor)	3710	110.6	65.4
Step 1.1 (Cap charge wait)	3555	150.2	64.8
Step 2 (BLE + sensor read)	3465	127.5	65.3
Step 3 (Temp detection)	3789	133.9	66.1
Step 4 (Checkpoint + flash)	56	150.3	1066

The results highlight that the checkpoint step dominates the energy cost, due to repeated flash access and state preservation. Sensor activation and BLE tasks complete within tens of milliseconds and consume modest energy, whereas Step 4 extends over one second with significant peaks. For this reason, optimizing checkpoint frequency and flash access patterns is critical to reduce Riotee's overall energy demand.

For more detail and better understanding, the full measurement dataset is provided in Appendix B.

4.2.3 Single-Cycle Energy

The minimal functional cycle for Riotee included sensor wake-up, a temperature reading, and BLE advertisement. The test was performed using a 976 µF capacitor, charged by the indoor solar panel. The Riotee board was powered through its VIN pin connected to the LDO output of the harvester, while ambient light and humidity conditions were recorded during the run. Figure 4.6 illustrates the physical setup for this experiment.

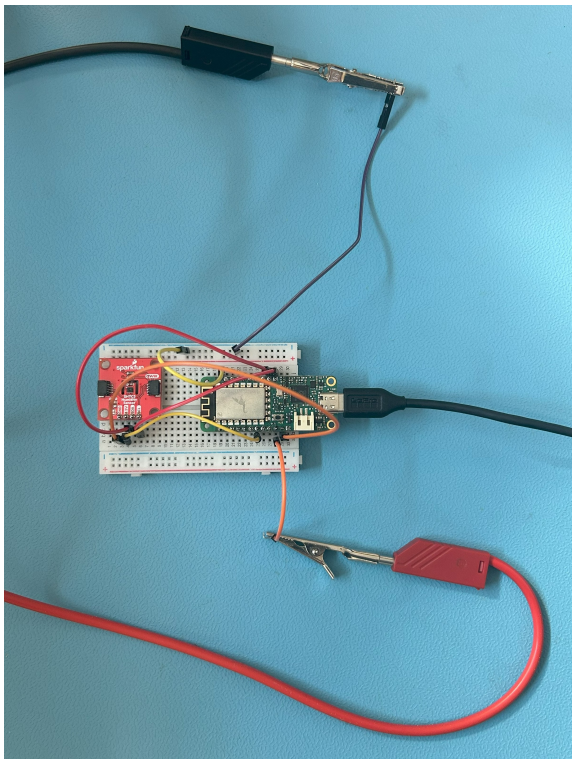

Figure 4.6: Single-cycle measurement and transmission setup.

Figure 4.7 shows the input power evolution during the cycle, while Figure 4.8 presents the capacitor charging profile. The capacitor voltage rose steadily from 1.27 V to 2.5 V (maximum voltage storage for configuration used) under the available illumination, confirming that the solar input was sufficient to both sustain the cycle and restore energy reserves.

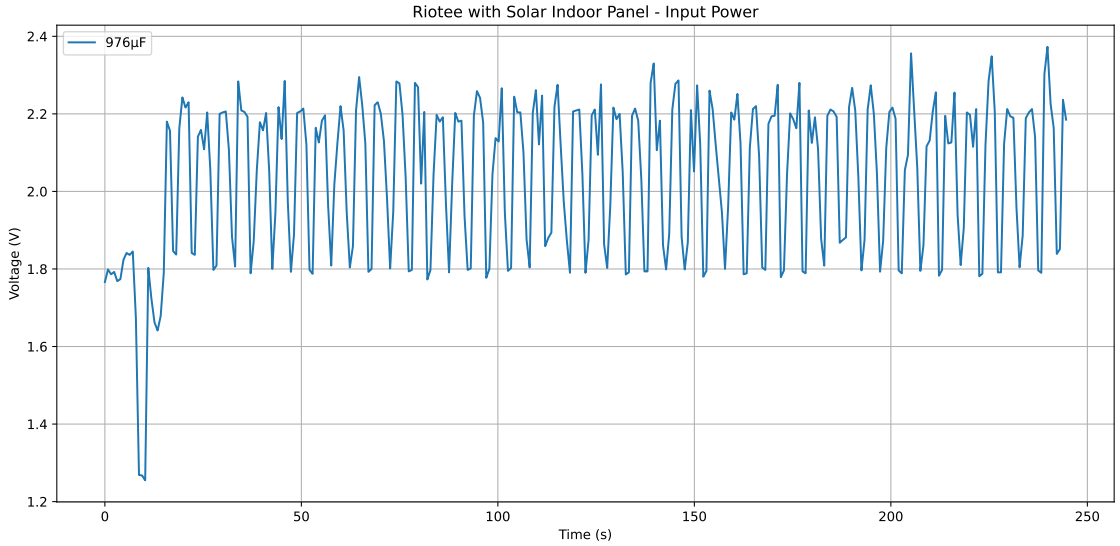

Figure 4.7: Input power profile of Riotee powered by an indoor solar panel during one cycle.

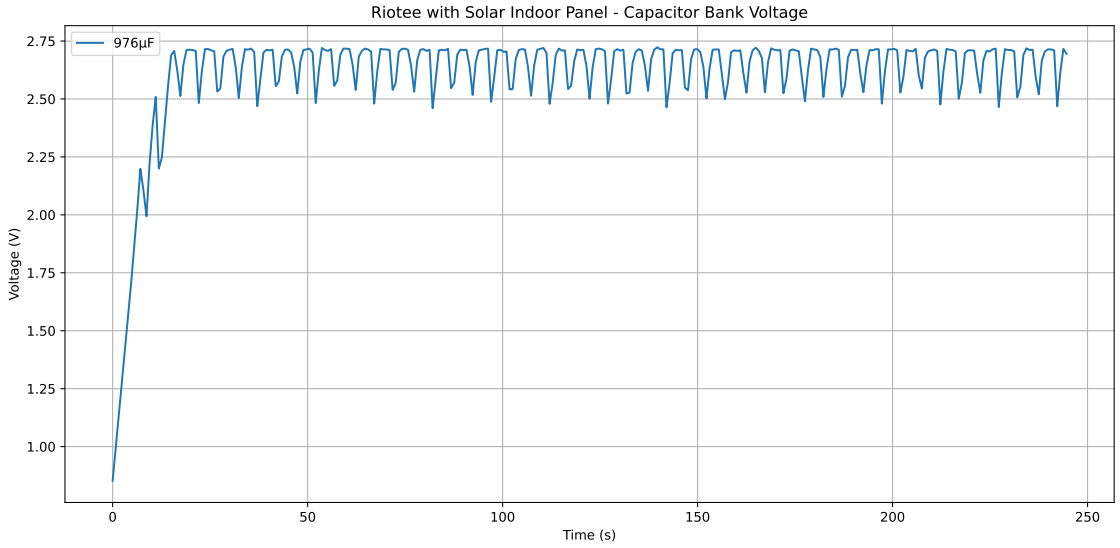

Figure 4.8: Capacitor voltage evolution of Riotee with a 976 µF bank under indoor solar harvesting.

Extended 24-hour trials were conducted separately on the harvesters, demonstrating that both solar and RF sources can supply sufficient energy for periodic operation of low-power nodes. However, when applied to the Riotee platform, the high energy overhead of flash checkpointing and resume operations dominated consumption. This mismatch means that while the harvesters themselves are capable of sustaining long-term operation, the reliance of Riotee on energy-intensive flash utilization makes the system unsuited for continuous autonomous deployment without further optimization.

4.2.4 Discussion

Riotee is a robust and flexible platform for complex edge applications that require ongoing processing, buffering, or machine learning tasks. However, its layered architecture adds unnecessary energy expenses for applications that only collect data from a sensor and send it. As a result, a more straightforward, less resource-intensive option was studied.

4.3 IN100 Platform

4.3.1 Hardware Architecture

The IN100 platform by InPlay is a small, highly efficient Bluetooth Low Energy (BLE) transmitter intended for straightforward and energy-efficient wireless applications. Unlike more complex SoCs, the IN100 is pre-configured via the NanoBeaconTool and does not require firmware development, making it ideal for constrained energy environments.

Internally, the IN100 integrates a compact memory subsystem with 4 KB of SRAM and 4 Kb of one-time programmable (OTP) eFuse for configuration and payload storage [21]. It includes a BLE 5.3 radio with programmable transmit power up to +5 dBm, supporting both 1 Mbps and 2 Mbps PHY modes. Peripheral support includes a UART, an I^2C interface, an 11-bit ADC for direct sensor measurements, and multiple GPIOs for external control. The device can also drive external circuits through two low-leakage load switches (SW0, SW1). In deep sleep mode (with the 32 kHz RC oscillator enabled), the current consumption is less than 650 nA, while the supply voltage range spans from 1.1 V to 3.6 V, making the device well suited for intermittent, capacitor-driven operation in energy-harvesting systems [21].

To enable true batteryless operation, the IN100 was combined with two essential components: a solar energy harvester and a nano-power hardware timer. The timer, a TPL5110 from Texas Instruments, is responsible for periodically powering the node while fully disconnecting it between each transmission. This external control decreases standby leakage current, ensuring energy is only consumed during active sensing and BLE advertisement.

This minimalistic architecture (IN100 + TPL5110 + SHTC3 sensor + solar panel) was first validated through a breadboard-based prototype described in Section 4.5, and is represented in the block diagram shown in Figure 4.11.

4.3.2 Cycle-Level Measurements

To characterize the energy consumption of the IN100 platform, a series of current profiling tests were performed using the Nordic Power Profiler Kit II (PPK2), as shown in Figure 4.9. Two IN100 development boards with identical configurations were programmed through the NanoBeacon Config Tool, differing only in operating clock frequency (400 kHz and 100 kHz). Supply voltages of 2.0 V and 1.8 V were provided directly by the profiler to evaluate performance under different operating points.

The external timer TPL5110 was configured to periodically power the node, with an interval determined by a resistor value (e.g., 10 s → 11.2 kΩ [41]). During each cycle, the profiler recorded the average current, peak current, and active time.. Measurements were repeated for both clock configurations and supply voltages. For comparison, equivalent tests were conducted on the Riotee board as mentioned before.

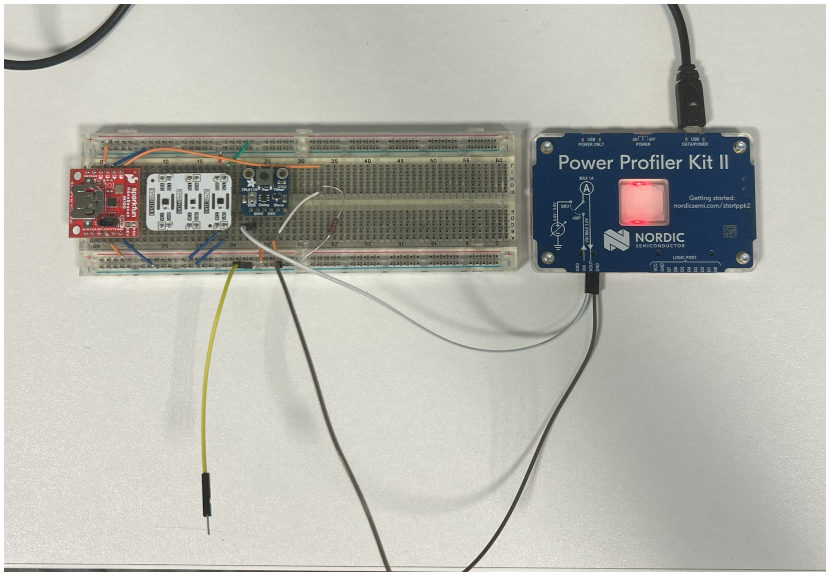

Figure 4.9: Current profiling setup for IN100 platform with Nordic Power Profiler Kit II.

Table 4.2 summarizes the results obtained with the power profiler measurements. At 400 kHz and 2.0 V, the IN100 consumed on average about 1.33 mA per cycle, with activity bursts reaching around 30 mA. At 1.8 V, the average current remained similar (1.32 mA), but occasional instability led to much higher peaks, with averages near 93 mA and some events exceeding 300 mA. At 100 kHz, the average current was slightly higher (around 1.40 mA), with peak currents increasing substantially (105 mA at 2.0 V and up to 142 mA at 1.8 V). These results highlight that, while the mean consumption remains fairly stable across configurations, the supply voltage and clock frequency can strongly influence instantaneous peak behavior.

Table 4.2: Representative current profiling results for IN100 platform (averaged over 11 cycles, excluding first measurement because of Timer initialization).

Configuration	**Avg. Current (mA)**	**Max (mA)**	**Active Time (ms)**
2.0 V, 400 kHz	1.33	30.51	15.69
1.8 V, 400 kHz	1.32	92.65	15.76
2.0 V, 100 kHz	1.40	105.06	16.51
1.8 V, 100 kHz	1.40	141.52	16.53

After analyzing these measurements and comparing them with those from the Riotee, it becomes clear that IN100 cycles are substantially less energy-demanding, since Riotee flash operations represent the main consumption element (Section 4.2). The TPL5110 timer ensured that the

system remained completely off between wakeups, reducing leakage and making capacitor-driven operation viable. A more detailed breakdown of the IN100 profiling results, including per-test cycle traces and configuration sweeps, is provided in Appendix C.

4.3.3 Twenty-Four-Hour Autonomy

Extended testing was performed in three locations: open space, meeting room, and lab. All used the LL200-2.4-75 solar panel, the TPL5110 set to 30-minute intervals (92.4 kΩ), and two capacitor configurations: 0.47 F and 1.0 F. Figure 4.10 illustrates a representative open-space case with a 0.47 F capacitor.

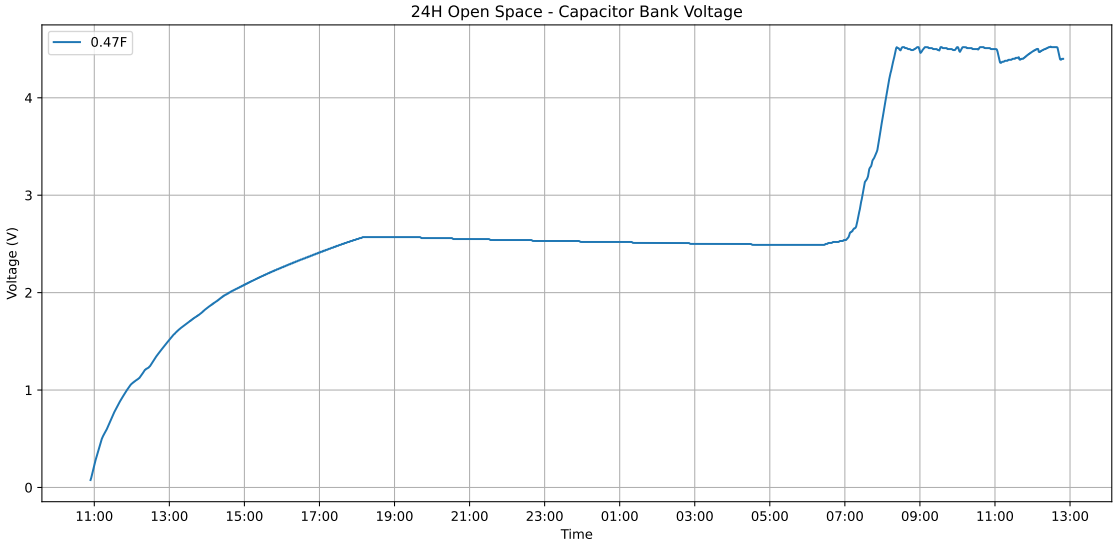

Figure 4.10: Capacitor voltage evolution over 24 h with solar harvesting and IN100 duty cycles.

Three distinct phases can be observed in the plot:

- **First charging phase (11:00–18:00):** the capacitor voltage rises under daylight, reaching around 2.7 V. This enables the system to overcome cold start and power multiple transmission cycles.

- **Night phase (18:00–09:00):** the voltage stabilizes near 2.7 V and decreases only slightly overnight to a minimum value of about 2.55 V, demonstrating that current leakage and power consumption were well balanced by residual storage.

- **Second charging phase (09:00 onward):** with the morning sunlight, voltage rises again, this time reaching close to 4.2 V, the maximum sustainable by the AEM10941 regulation stage. The ending plateau indicates that the harvester supported the IN100 cycles while also charging the capacitor to full capacity.

In general, the IN100 node maintained stable operation in all settings. The analysis of Figure 4.10 demonstrates that, even with the 0.47 F super capacitor, the system operated uninterruptedly during a full day, validating its feasibility.

4.3.4 Discussion

While Riotee provides a rich set of features through its checkpointing mechanism, this flexibility comes at the cost of higher energy per cycle and significant flash overhead usage. In contrast, the IN100 is better suited for lightweight, periodic sampling/reporting tasks, making it better simple and ultra-low consumption scenarios. Table 4.3 summarizes the comparison between both platforms.

Table 4.3: Comparison of Riotee and IN100 platforms for batteryless node deployment.

Feature	**Riotee (nRF52833 + PMU)**	**IN100 + TPL5110**
Processing Core	ARM Cortex-M4F SoC	InPlay IN100 BLE NanoBeacon
Firmware Complexity	High (modular, checkpoint)	Low (sequential)
Energy per Cycle	160 µJ (with flash)	20 µJ (avg. per TX)
Sleep Current	∼2.1 µA	∼35 nA (TPL)
Sleep Time	Configurable (checkpoints)	30 minutes (@92.4 kΩ)
Overhead	Flash writes, system reboots	None (timer-controlled)
Suitability	Complex edge applications	Minimal sensing / reporting

According to Table 4.3, Riotee's checkpoint-based execution protects against power loss, although it requires significant energy for flash operations. The IN100 combines a minimal BLE SoC with an external timer, resulting in significantly reduced standby leakage and cycle energy, but losing flexibility. These compromises indicate that Riotee is better for computation-heavy edge tasks, while IN100 is more suited for ultra-low-power, capacitor-based applications.

4.4 Comparative Assessment

Sensor and timer selection was mainly influenced by ultra-low power needs, alignment with the energy-harvesting power availability, and characteristics that promote effective periodic functioning. Two categories of components were especially significant: timers for scheduling and humidity/temperature sensors for monitoring the environment.

4.4.1 Timer Evaluation

A comparison of the TPL5110 and TPL5111 was carried out to identify the best low-power timer for operation without batteries. In the proposed architecture, the timer is essential because it guarantees that the node only powers ON when sufficient energy has been harvested, otherwise,

it remains fully disconnected from the capacitor. This way, leakage currents are prevented during idle times, which would otherwise drain limited storage and compromise autonomy. When enough energy is stored, the timer enables the system for a short interval, during which sensing and transmission are executed, before it is powered off again.

Table 4.4 outlines the main differences between the two devices. The TPL5110 was chosen due to its ability to physically cut off power from the system during idle periods, ensuring nearly zero leakage current (typ. 35 nA). This works particularly well with energy harvesters such as the AEM10941, which can cold-start the system once sufficient energy is available. In contrast, the TPL5111 maintains power to the MCU and only wakes it through an interrupt, which is less efficient for ultra-low-power batteryless operation [10, 41, 42].

Table 4.4: Comparison between TPL5110 and TPL5111 [41, 42].

Feature / Model	**TPL5110**	**TPL5111**
Main Use Case	Powers ON system via external switch	Sends interrupt to MCU (MCU stays powered)
Wake Trigger	Powers up connected load at intervals	Sends digital signal (interrupt)
Control Output Type	Drives Power MOSFET (EN pin)	Drives MCU interrupt line
ON Time Duration	Until MCU pulls DONE pin	Until MCU acknowledges DONE
Timing Configuration	External resistor (100 ms – 2 h)	Same
Supply Current (typ.)	35 nA	35 nA
Accuracy	1% (typ., resistor dependent)	1% (typ., resistor dependent)
Typical Use Case	Wake MCU from total power-off	Wake MCU from low-power sleep

The analysis confirmed that the TPL5110 is the most suitable option, since it ensures that the IN100 node remains completely disconnected until the capacitor is recharged, enabling true cold-start cycles with negligible leakage. The precision of its timing (within $\pm 1.5\%$) is more than adequate for periodic sensing and BLE advertisement tasks, where tight synchronization is not required. With that, it is the most efficient choice for a batteryless architecture, whereas the TPL5111 would unnecessarily keep the MCU powered, reducing energy availability.

4.4.2 Sensor Evaluation

Table 4.5 compares four commonly available temperature and humidity sensors. The main factors taken into account were sleep mode and active current, accuracy of temperature and humidity, as well as power-on response durations. From this comparison, the **SHTC3** was determined to

be the best sensor for the node. It provides a remarkable equilibrium among energy efficiency, sampling speed, and accuracy, making it ideal for batteryless applications powered by harvested energy [36].

Despite the SHT40 offering the highest precision and a very low active current (210 µA) in normal operation, its comparatively slower response time and limited immediacy made the SHTC3 a more functional option for this design [35]. The SHTC3 combines fast wake-up (240 µs) with flexible operating modes: in normal mode it requires 900 µA for 12 ms, while in low-power mode it operates at 270 µA for 0.8 ms. This balance between configurability, compact size, and very low sleep current (<0.2 µA) makes the SHTC3 particularly efficient for reducing overall energy use during sporadic node operation, which is critical in energy-harvesting scenarios [36].

The ENS210 and HDC2080 were additionally taken into account. The HDC2080 features the lowest sleep current (50 nA) and a quick response, but it provides slightly reduced accuracy and a limited number of integrated features. The ENS210 provides great precision and quick responses; however, it was ultimately omitted because of its elevated active current (6.6 µA), making it less suitable for energy-harvesting applications [23, 40].

Table 4.5: Comparison of Humidity and Temperature Sensors [23, 35, 36, 40].

Feature	**ENS210**	**HDC2080**	**SHT40**	**SHTC3**
Humidity Accuracy	±2% RH (typ)	±2% RH (typ)	±1.8% RH (typ), ±1.5% (best)	±2% RH (typ)
Temperature Accuracy	±0.15 °C (typ)	±0.2 °C (typ)	±0.1 °C (typ)	±0.2 °C (typ)
Supply Voltage Range	1.71–3.6 V	1.62–3.6 V	1.08–3.6 V	1.62–3.6 V
Sample time	∼110–130 ms	∼225–660 µs depending on resolution	∼1 ms	∼12.1 ms (normal), ∼0.8 ms (low-power)
Active Current	6.6 µA (avg @ 1 Hz)	0.55 µA (avg @ 1 Hz), 0.7–0.9 mA (conv.)	0.4 µA (avg @ 1 Hz)	270 µA (low-power), 900 µA (normal)
Operating Temp Range	–40–100 °C	–40–85 °C	–40–125 °C	–40–125 °C
Features	Direct RH/T output, low standby	Integrated heater, auto mode	Internal heater, NIST traceable, supports condensation	Fast wake-up, NIST traceable

These choices demonstrate a compromise among energy efficiency, speed of measurement, and data reliability, which are essential priorities in systems exclusively powered by harvested energy.

4.5 Prototype Node Validation and Range Testing

After defining the final architecture for the sensing node (including selection of the IN100 SoC, TPL5110 nano timer, SHTC3 sensor and LL200-2.4-75 solar panel), a full system block diagram was created to guide integration. This is shown in Figure 4.11. The architecture was designed to enable ultra-low-power, energy-autonomous operation using harvested indoor light. A more detailed description will be given in Chapter 5.

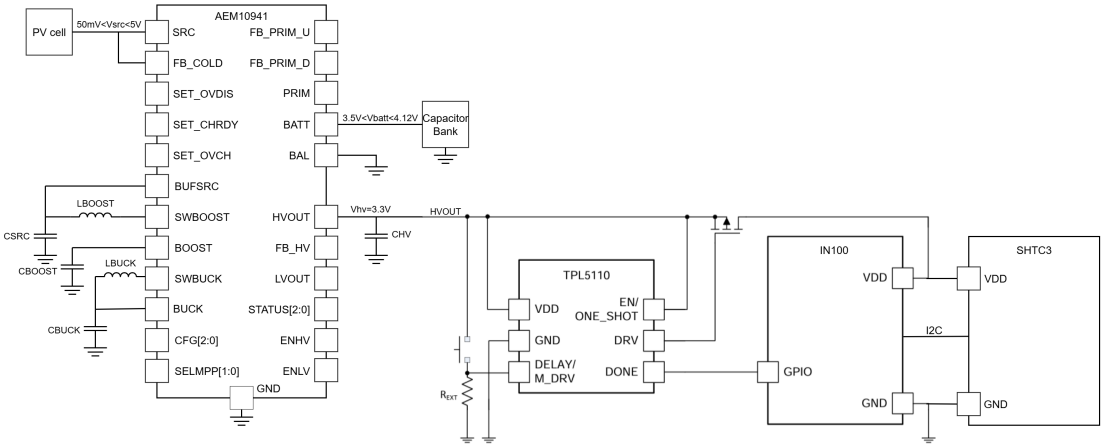

Figure 4.11: System block diagram: Solar Harvester + TPL5110 + IN100 + SHTC3. This architecture was used in prototype validation prior to PCB design.

Before proceeding with printed circuit board (PCB) design and production, a breadboard-based prototype node was assembled to validate this component combination under real-world conditions. The main objectives were to:

- Confirm the node could operate autonomously on solar energy alone.
- Measure capacitor charge/discharge behaviour over extended periods.
- Evaluate BLE communication range in typical indoor environments.
- Establish how long the system would function without harvesting (control test).

Figure 4.12 shows the prototype node built for these tests.

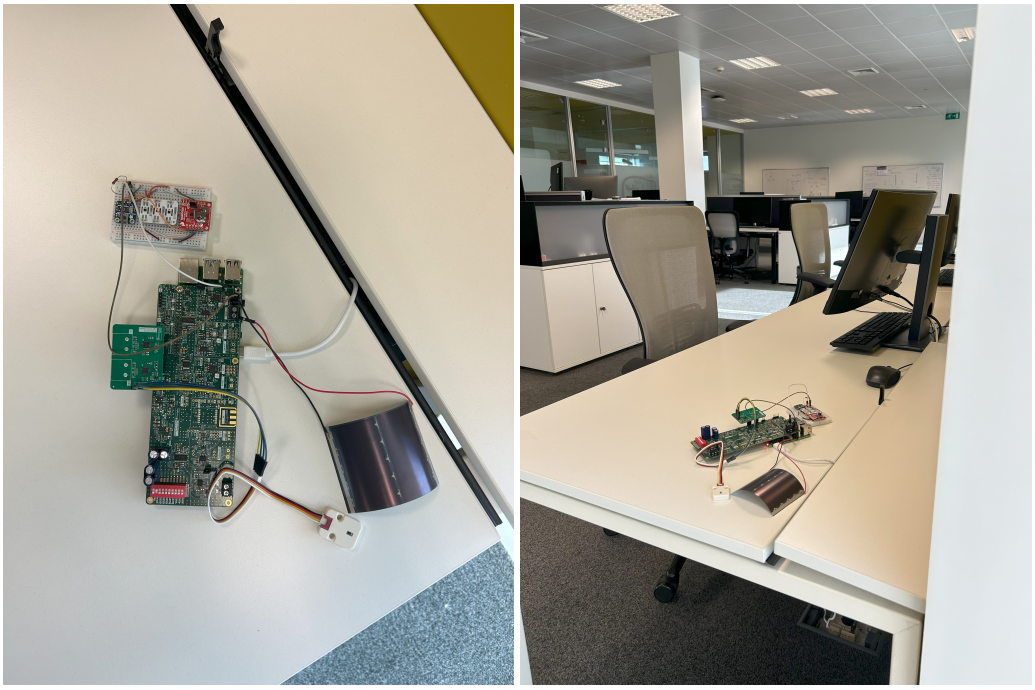

(a) (b)

Figure 4.12: Prototype node using final architecture components, deployed for long-duration and range testing.

4.5.1 Test Setup and Environments

All tests used a 0.47 F super capacitor and configured the TPL5110 with a 30-minute wake-up period. The node was implemented in two different indoor environments within the Fraunhofer AICOS facility: an open office area and a meeting room.

In practice:

- One prototype node was installed inside a meeting room, and another on one side of the open space (around 8 and 10 meters away from the BLE receiver, respectively).
- A BLE receiver, implemented with an ESP32 dongle connected to a Raspberry Pi, was placed at a fixed position in the middle of the open space to log all advertisements (Figure 4.13a).
- The nodes operated under ambient light with the solar panel connected, and capacitor voltage, input power, and lux levels were recorded over time.

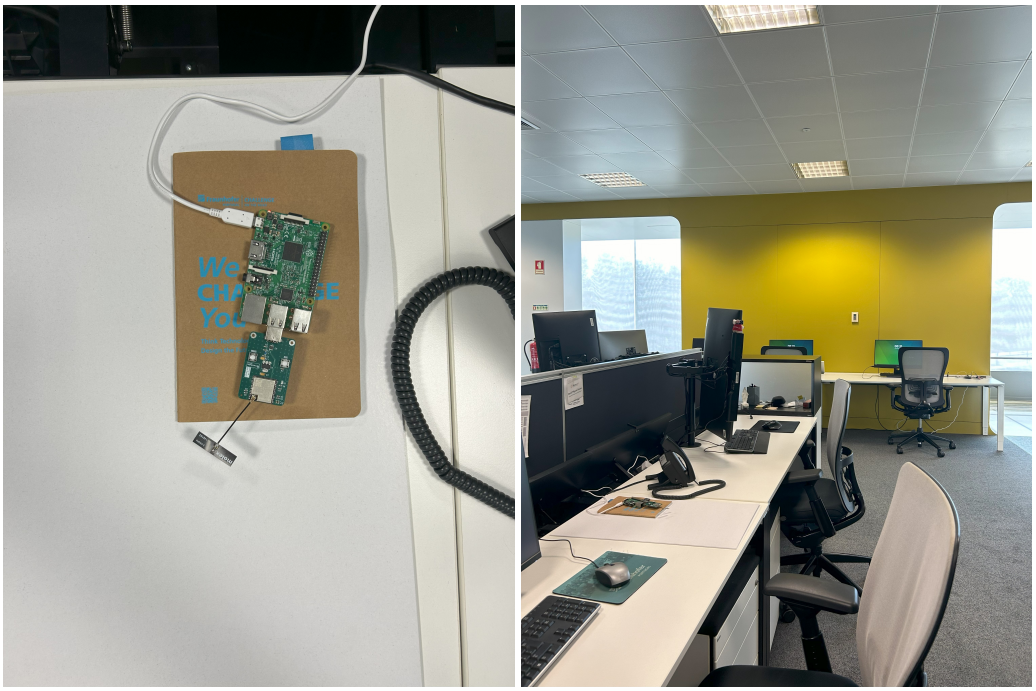

(a) (b)

Figure 4.13: Stationary BLE dongle and laptop used to log advertisements during range testing.

4.5.2 Long-Duration Autonomy Results

The first objective was to confirm whether the prototype could sustain perpetual operation using indoor light. Capacitor voltage and input power were monitored over multiple hours per location.

Open Space Results:

Figure 4.14 shows the capacitor voltage profile in the open space office. The voltage demonstrates repeated charge–discharge cycles, where the supercapacitor is recharged during periods of illumination and gradually discharges when light levels drop. This pattern indicates stable harvesting performance over multiple days.

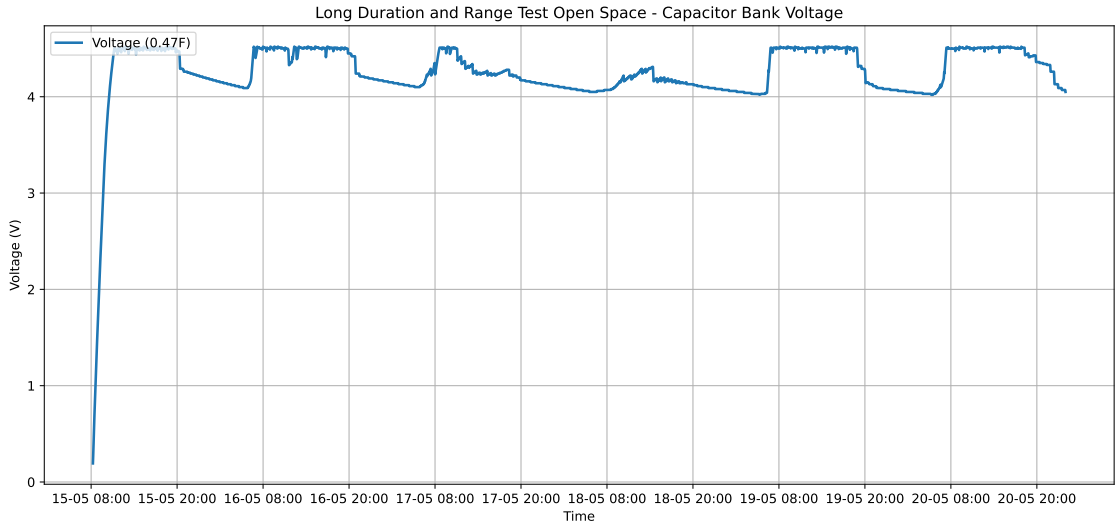

Figure 4.14: Capacitor voltage over time in open-plan office with solar harvesting.

The corresponding input power and illuminance levels are illustrated in Figure 4.15. Peaks in illuminance from both natural and artificial light correlate with increases in harvested power, while low-light periods result in reduced input. Despite these fluctuations, the capacitor voltage remained within safe operational limits.

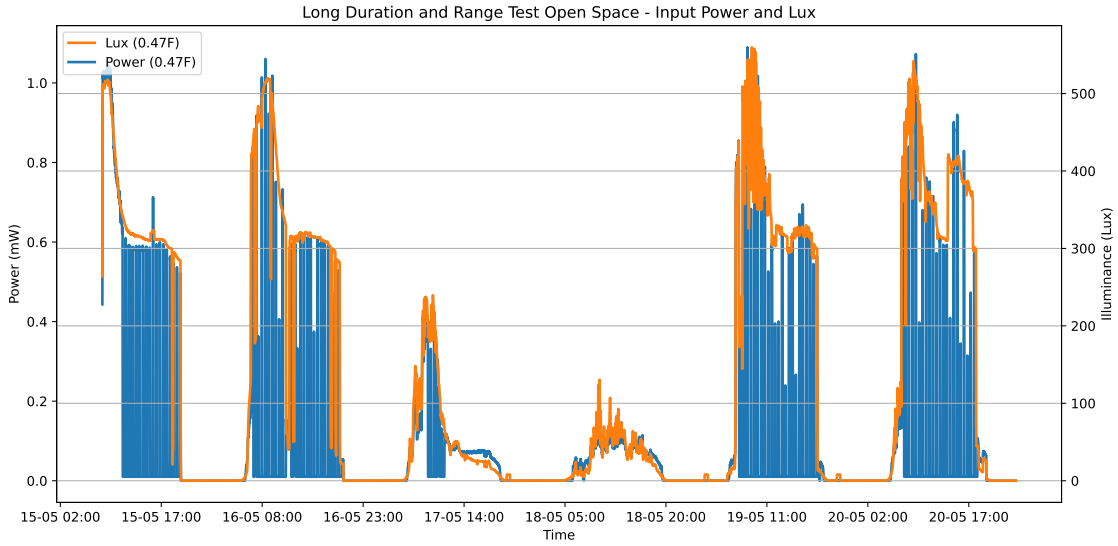

Figure 4.15: Solar harvester input and illuminance during open space deployment.

Meeting Room Results:

Figure 4.16 shows the capacitor voltage evolution in the meeting room, where available light was considerably lower. Voltage increases occur in a step-like fashion, corresponding to the intermittent activation of artificial lighting. While the growth was slower compared to the open space scenario, the capacitor was still able to recharge consistently.

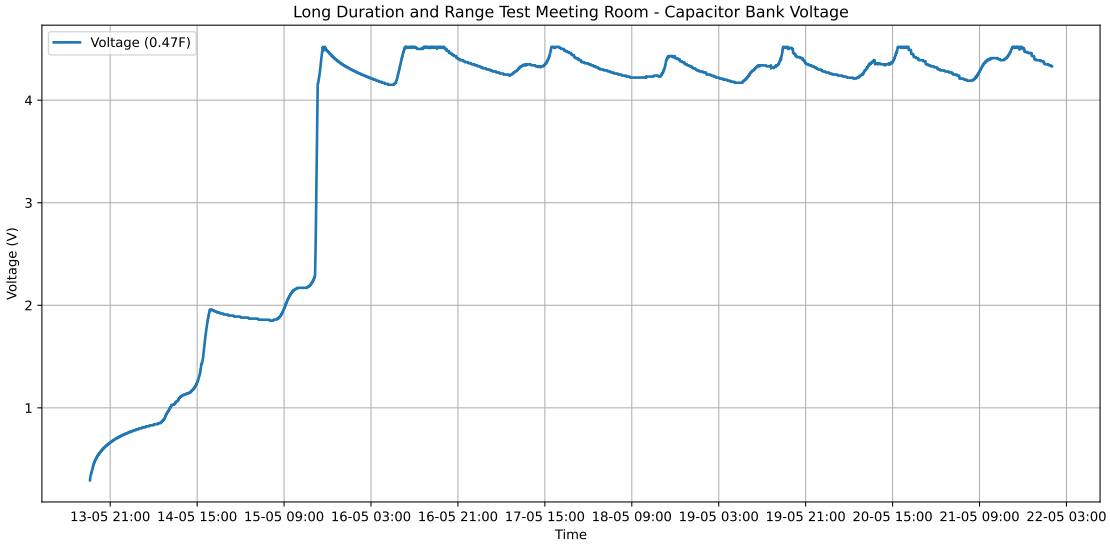

Figure 4.16: Voltage profile showing periodic recharge and operation under lower lighting conditions.

The staircase profile in Figure 4.16 reflects the periodic activation of the node enforced by the TPL5110, configured for 30-minute intervals. Each voltage increment corresponds to the capacitor recharging between wake-up events, after which the node performs a sensing and BLE advertisement cycle. Throughout multiple days of operation, the harvested energy consistently outpaced the usage, as shown by the overall upward trend in capacitor voltage until it reached the limit of approximately 4.5 V. During the night periods, the capacitor discharged with voltage drops between 0.2–0.4 V. This corresponded to an energy loss of about 0.9–1.8 J, depending on the night. These losses were quickly overcome during the following day, as the energy gathered per cycle amounted to several tens of joules, ensuring that the system maintained a sufficient energy buffer for ongoing autonomous operation.

The input power and illuminance measurements in Figure 4.17 confirm this behavior. While the lower average illuminance values limited harvested power, the results demonstrate that even under these constrained conditions, the system maintained sufficient energy for uninterrupted autonomous operation.

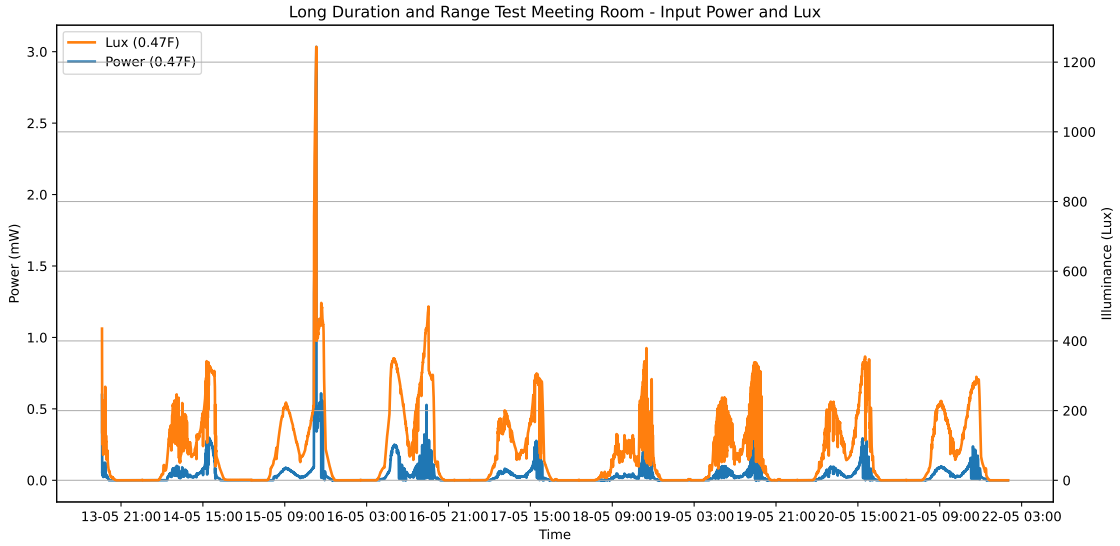

Figure 4.17: Lower illuminance levels still enabled autonomous node operation.

In both cases, the capacitor voltage remained within operational limits across the full test duration, confirming that ambient indoor light was sufficient to power the node indefinitely.

4.5.3 Control Test – Discharging

To verify that long-duration operation was indeed due to energy harvesting and not residual charge, the same prototype was tested with the solar panel disconnected. The capacitor (0.47 F) was pre-charged to the same initial voltage used in previous experiments.

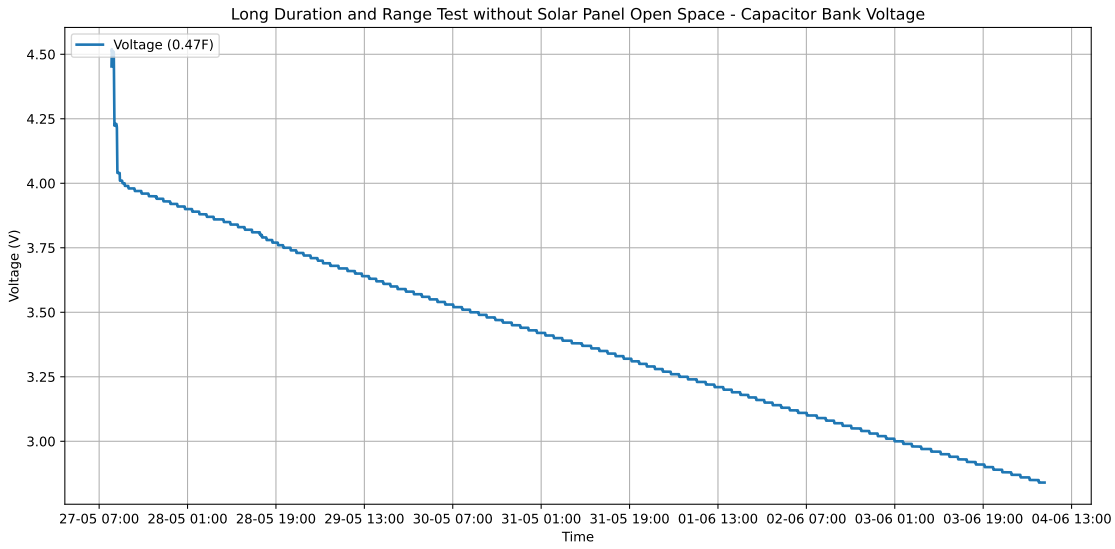

Figure 4.18: Capacitor discharge profile without solar input. The node eventually ceased operation once voltage fell below the operating threshold, confirming harvesting was essential for sustained autonomy.

As shown in Figure 4.18, the capacitor voltage follows a gradual and continuous decrease over time. Each drop corresponds to the periodic transmission cycles of the node, with no recovery in between due to the absence of harvested energy. From about 4.52 V, the voltage gradually decreased until it reached the minimum operating threshold of approximately 2.84 V, at which point the node stopped operating. The overall slope of the discharge was around 0.21 V per day. This corresponds to a total released energy of about 3.2 J from the 0.47 F capacitor, supporting more than 350 wake-up and transmission cycles at the 30-minute TPL5110 periodicity. This quantification confirms that the extended autonomy observed in previous tests was sustained by energy harvesting and not by residual charge alone.

4.5.4 BLE Range and Connectivity

Following the validation of energy autonomy, the next step was to demonstrate practical data communication from the node. Bluetooth Low Energy (BLE) was chosen due to its extensive use in IoT systems, its inherently low power consumption, and the direct direct assistance offered by the IN100 SoC. To reduce energy usage, data was encapsulated directly into BLE advertisement packets, allowing sensor readings to be periodically broadcast without the overhead of establishing and maintaining connections.

The advertising setup was completed using the NanoBeacon Config Tool. A single advertising set was enabled on the three BLE advertising channels (37, 38, 39), with a 2000 ms advertisement interval, a random delay of $0-10$ ms and $+4$ dBm transmit power. The device returned to sleep after each transmission, using a static random address with standard channel hopping across the three channels. Sensor data was provided through ADC Channel 1 (MPGIO5), configured with VDD power switching and 16-sample averaging to accurately map voltages prior to encapsulation into the payload.

Initial BLE communication tests revealed significant non-detection of packets across different indoor environments. Early tests were performed with two transmitting nodes placed in fixed locations, and one receiving dongle centrally positioned in the test area. As shown in Table 4.6 and Table 4.7, loss rates varied significantly depending on the location and structural environment.

$$\text{Effectiveness} = \left(\frac{\text{Received}}{\text{Sent}}\right) \times 100$$

Table 4.6: Message transmission results (Prototype Node – Open Space).

Metric	**Day 1**	**Day 2**	**Day 3**	**Day 4**	**Day 5**	**Total**
Messages Sent	47	47	47	47	48	236
Messages Received	42	37	43	38	39	199
Messages Failed	5	10	4	9	9	37
Effectiveness (%)	89.36%	78.72%	91.49%	80.85%	81.25%	**84.32%**

Table 4.7: Message transmission results (Prototype Node – Room 1.11).

Metric	**Day 1**	**Day 2**	**Day 3**	**Day 4**	**Day 5**	**Total**
Messages Sent	48	48	48	48	48	240
Messages Received	41	42	45	44	40	212
Messages Failed	7	6	3	4	8	28
Effectiveness (%)	85.42%	87.50%	93.75%	91.67%	83.33%	**88.33%**

Despite these early limitations, later iterations of the hardware and configuration, particularly those incorporating external antennas and improved orientation, showed greatly reduced loss rates. Throughout the final long-duration evaluations, BLE advertisements were consistently received by the stationary USB dongle, even in the more enclosed meeting room and open space environments.

These results confirm that the final node design using the IN100 SoC meets the reliability and range requirements for short-range indoor deployments, with high effectiveness even under mild occlusion.

It is also important to note that part of the packets not received in earlier stages may be attributed to the use of SparkFun breakout boards. These boards are known to include a suboptimal 26 MHz crystal, which can introduce frequency offset issues and reduce communication range and reliability. In a final production-quality design, using a validated crystal from the authorized supplier list would aid in removing this source of instability [39].

In addition, other environmental elements (WiFi interference, Bluetooth congestion, reflections, antenna design, orientation, and receiver location) are anticipated factors that influence detection variability in actual indoor situations. These factors, though inevitable, can be controlled through effective system design and proper testing.

4.5.5 Summary and Impact

This phase of testing demonstrated that the final node architecture:

- Can operate continuously and autonomously using only indoor ambient light.
- Has predictable and stable charging/discharging behavior over time.
- Offers reliable BLE communication range in real-world office-like environments.

These results provided high confidence in the viability of the nodes and informed the decision to proceed with the final PCB layout and fabrication.

Chapter 5

Final Implementation and Results

This chapter outlines the final implementation phase of the project along with the experimental findings achieved. It is structured into separate stages: the final design of the created node, followed by communication evaluation utilizing Received Signal Strength Indicator (RSSI) measurements, analysis of simultaneous scanning and unreceived packets, and a final deployment overview.

5.1 Luxor Node: Final Design and Architecture

The final version of the developed prototype was officially named the **Luxor node**, alluding to resilience and endurance, key characteristics of the presented solution, while also referencing lux, the unit of illuminance, reflecting its solar-powered nature. Luxor is a batteryless environmental sensor node designed for long-term autonomous operation in real-world indoor scenarios under harvested environmental energy.

Hardware Architecture

The Luxor node is composed of a custom-designed PCB integrating the following elements (see Figure 5.1 for the highlighted blocks):

- **AEM10941 PMIC (e-peas)** (yellow block): A power management IC that harvests energy, accommodates indoor solar sources, enables cold start, and features MPPT tracking. Controls charging and the behaviour of the system startup with configurable thresholds [10].
- **IN100 NanoBeacon (INPLAY)** (white block): Ultra-low-power Bluetooth Low Energy SoC. This module handles the measurement and transmission of sensor data through BLE advertisements at adjustable intervals [21].
- **TPL5110 Nano Timer (Texas Instruments)** (red block): An extremely energy-efficient programmable timer that activates periodic wake-ups by supplying power to the IN100. It makes certain that the node remains completely off during cycles, preventing idle-mode leakage [41].

- **SHTC3 Sensor (Sensirion)** (purple block on 5.1c): A low-power digital humidity and temperature sensor, chosen for its low energy use and I²C interface [36].
- **Energy Storage (ABRACON)** (orange block on 5.1b): Supercapacitor ADCM-S06R0S, enabling buffered function during periods of reduced light [1].
- **Antenna Options** (blue block): The PCB supports both a compact PIFA antenna and a U.FL connector for external 2.4 GHz antennas.
- **Sensor Module Interface** (pink block): The design features modular connectors to link external sensor boards, allowing for both expansion and replacement.
- **Solar Panel:** Flexible panel compatible with indoor lighting (*e.g.* PowerFilm LL200-2.4-75 or TDK BCS4430B6), selected according to light conditions and node size, connected through VIN/GND pads (green blocks).

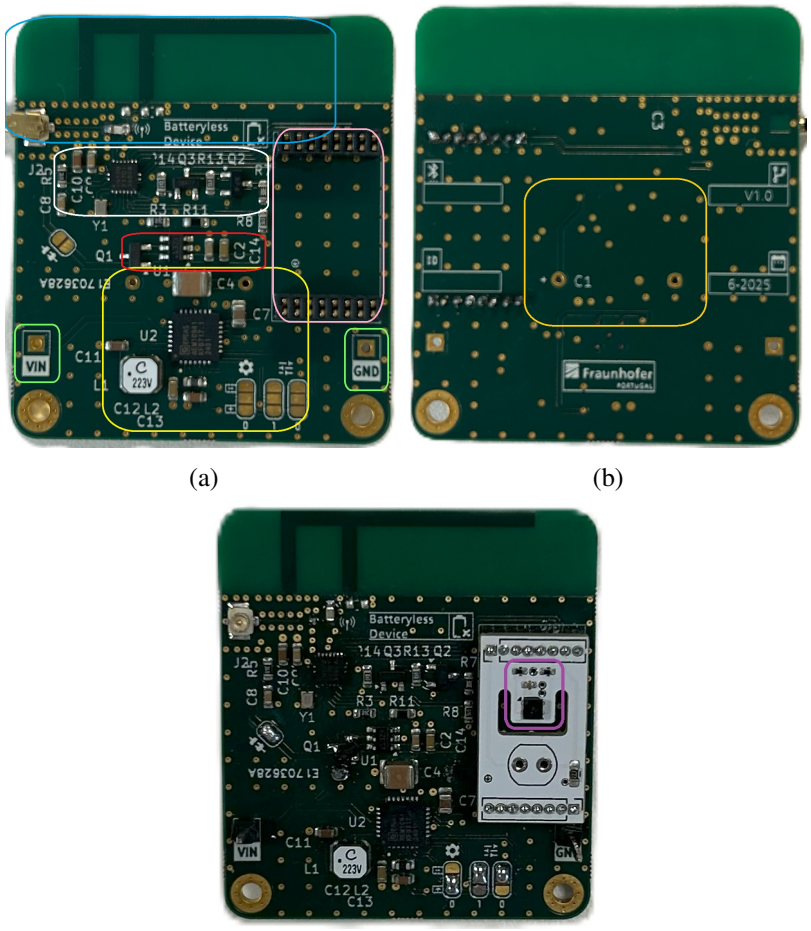

(a) (b)

(c)

Figure 5.1: Different views of the Luxor node showing the main hardware blocks highlighted in color (yellow – PMIC, white – BLE SoC, red – timer, blue – antenna, pink – sensor interface, green – VIN/GND to connect the solar panel, orange – supercapacitor, purple - SHTC3 sensor).

PCB Antenna Design and Simulation Results

To ensure compact integration and optimal wireless performance, a custom Planar Inverted-F Antenna (PIFA) was designed directly onto the PCB. This eliminated the need for external antennas in constrained deployments while maintaining adequate radiation efficiency at 2.4 GHz.

The antenna was modeled and simulated using Ansys HFSS 2024 R2. Key simulation results are provided in Appendix D.

Figure D.1 in the appendix shows the simulated return loss (S11), which presents a strong resonance near 2.48 GHz. The S11 value dips below -10 dB, indicating minimal signal reflection and good impedance matching within the BLE band.

The input impedance, visualized in the Smith Chart (Appendix Figure D.2), confirms that the curve passes near the chart's center, validating a resistive impedance close to 50 Ω at resonance, ideal for maximum power transfer.

To gain further insight, the real and imaginary components of the terminal Z-parameters were plotted (Figures D.3 and D.4). These show that the real component stabilizes near 50 Ω, while the imaginary part crosses zero at the resonant frequency, as expected for efficient radiating behavior.

The directional characteristics of the antenna were assessed using 3D gain simulations. Figure D.5 shows the primary radiation lobe and gain structure. Alternate views are included in Figures D.6 and D.7, highlighting asymmetries caused by the PCB layout and ground plane.

These simulation results demonstrate that the designed PIFA antenna is well-tuned for BLE communication and suitable for integration in the Luxor node.

Schematic Overview

The Luxor node follows a modular architecture, separating the **mainboard** (responsible for energy harvesting, power management, and BLE communication) from the **sensor module**, which contains the environmental sensing circuitry. This design facilitates easy replacement or upgrade of the sensing stage without requiring changes to the energy and communication backbone. The complete schematics of both boards are provided in Appendix E (mainboard) and Appendix F (sensor module).

Harvester

The energy harvesting stage is implemented using the **AEM10941 PMIC** (Figure 5.2), designed for ultra-low-power indoor photovoltaic operation. The input (VIN/SRC) connects to the PV cell and passes through inductors (L1 = 22 µH, L2 = 10 µH) and decoupling capacitors (C11–C13) for stable boost/buck conversion. The IC's maximum power point tracking (MPPT) is configured via pins `SELMMP[1:0]`, while the output regulation and storage thresholds are defined through `CFG[2:0]`.

The harvested energy charges a capacitor bank connected at the `BATT/CAP_OUTPUT` node, which includes a fixed 150 µF capacitor (C4) in parallel with the external supercapacitor bank

(C1). The regulated high-voltage output (`HVOUT`, 3.3 V) is stabilized by C7 (10 µF) and supplies the downstream circuits, including the timing controller and BLE SoC.

This configuration enables efficient indoor energy harvesting, cold-start operation from as low as 50 mV, and long-term storage on supercapacitors, ensuring reliable powering of the Luxor node even under variable illumination [10].

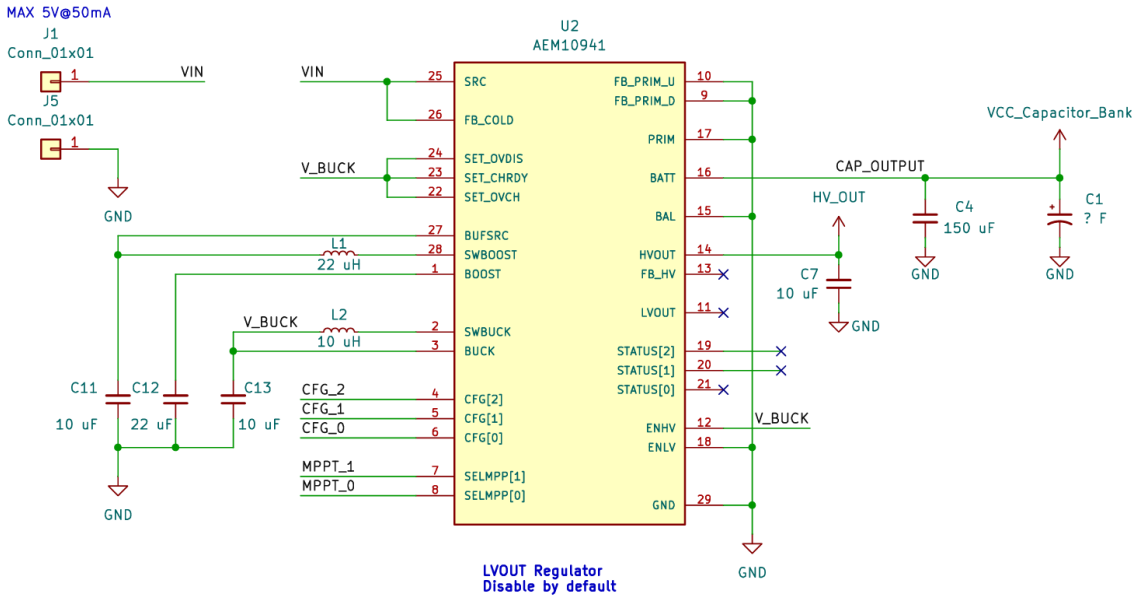

Figure 5.2: AEM10941 harvester schematic: PV input, MPPT configuration, capacitor bank, and regulated HV output.

IN100 BLE SoC and Antenna Interface

At the core of the mainboard is the **IN100 BLE System-on-Chip** (Figure 5.3), which integrates the BLE radio, microcontroller, and baseband. The RF output is routed to a PCB-integrated PIFA antenna, with an antenna switch (JP1) enabling selection between the onboard antenna and a U.FL connector for an external antenna [21].

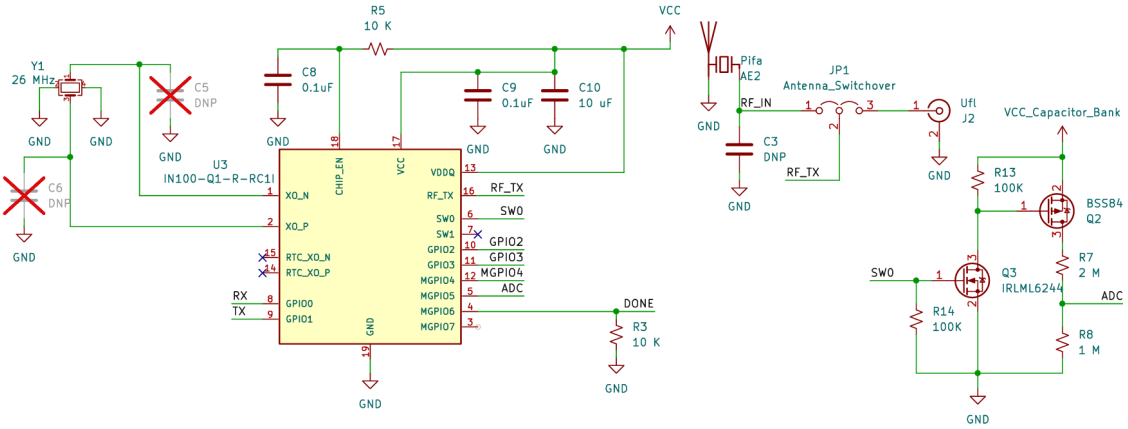

Figure 5.3: IN100 BLE SoC section with antenna interface, decoupling capacitors, and power control MOSFETs.

Ultra-Low-Power Timing Control

A **TPL5110 ultra-low-power timer** (Figure 5.4) is used to physically disconnect the mainboard from the supercapacitor between measurement cycles. The timer controls a PMOS transistor through its *drive-high* output, effectively cutting or enabling the power path. It activates the node at fixed intervals determined by R11, and after the measurement and BLE transmission, the IN100 asserts the DONE pin, signalling the timer to cut power until the next cycle. This strategy reduces leakage losses and extends operating lifetime under limited energy availability [41].

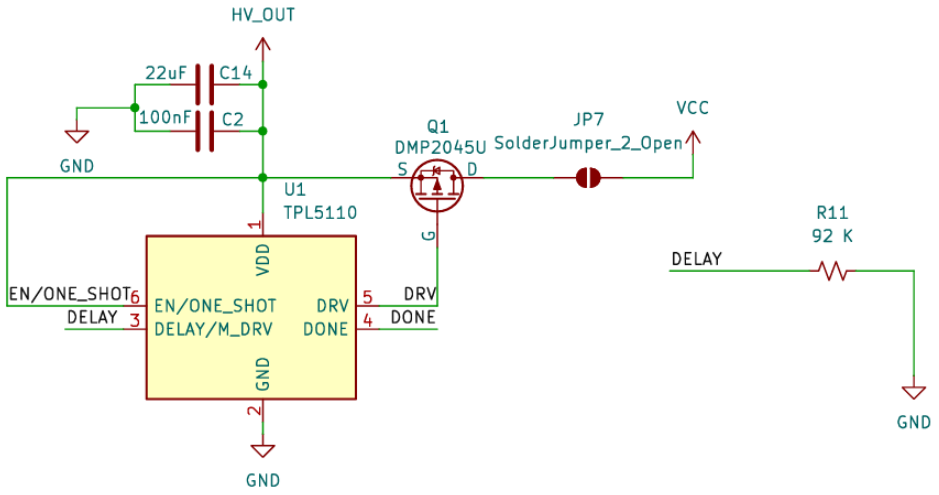

Figure 5.4: TPL5110 timer circuit for duty cycling and power gating of the mainboard.

Sensor Module Electronics

The sensor module implemented in this work (Figure 5.5) integrates a **Sensirion SHTC3** temperature and humidity sensor. Two 10 kΩ resistors (R1, R2) act as I²C pull-ups, and a 100 nF decoupling capacitor (C1) ensures local supply stability. This design is optimized for low idle current and minimal communication latency, enabling accurate readings while preserving energy [36].

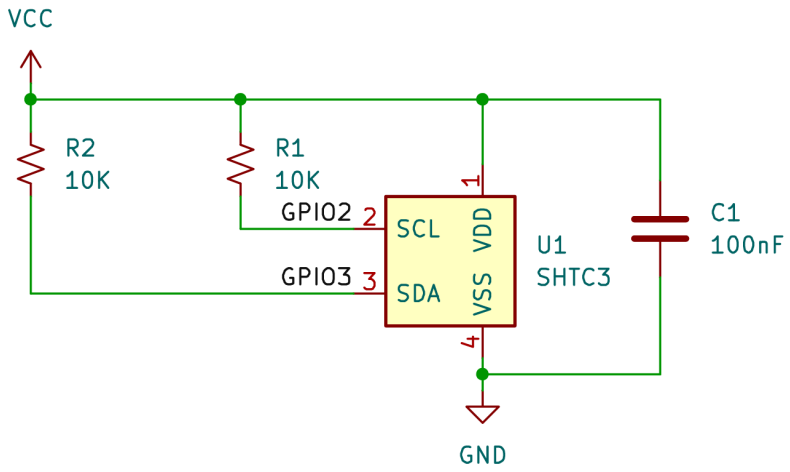

Figure 5.5: Sensor module schematic featuring the SHTC3 temperature and humidity sensor.

Sensor Module Connector and Programmer

The mainboard interfaces with the sensor module via an **8-pin header** (Figure 5.6), providing power (VCC, GND), UART (RX, TX), and I²C (SCL, SDA) lines. This configuration supports both serial and I²C digital sensors, allowing flexible deployment for different sensing modalities without modifying the mainboard.

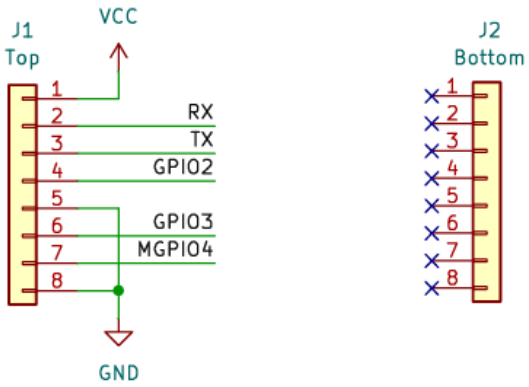

Figure 5.6: 8-pin connector linking the mainboard to the modular sensor board.

In addition to the sensor connector, the system employs a dedicated **USB-C programmer** (Figure 5.7), which provides an interface for flashing firmware to the IN100 BLE SoC and for debugging during development. The programmer communicates with the SoC through the UART interface, specifically using the **RX and TX pins**, ensuring reliable programming and serial monitoring. It can also power the board during development, supplying VCC alongside the communication lines, thereby simplifying testing and firmware updates without requiring an external power source.

Figure 5.7: USB-C programmer used for firmware upload and debugging of the IN100 BLE SoC.

Energy Storage

The energy storage stage is based on a supercapacitor bank that buffers the harvested energy and ensures continuous operation of the node even under fluctuating illumination. In this work, a **0.47 F, 5.5 V supercapacitor** was used [1], chosen for its high cycle life, low equivalent series resistance (ESR), and ability to sustain repeated charge–discharge cycles with minimal degradation.

The selection of this capacitor value was not arbitrary but directly supported by the studies conducted in Chapter 3. In particular:

1. The fundamental energy consumption of a complete operation cycle of the node (sensor sampling and BLE advertisement) was characterized.
2. The operating frequency of the system was established, determining how often these cycles occur under realistic deployment scenarios.
3. The average charging rate of the harvester over a full day, considering varying indoor illumination conditions, was experimentally measured.
4. Based on these results, the capacitor value was dimensioned to maximize the use of the available harvested energy while providing a safety buffer to cope with transient drops in power availability.
5. Finally, the minimum capacitance required to sustain at least one full operation cycle was estimated, ensuring that the chosen 0.47 F provides both efficiency and reliability.

This storage element provides a stable reservoir for powering the sensing and communication stages, enabling multiple BLE transmission cycles during low-light intervals when the photovoltaic source cannot supply sufficient energy. Compared to traditional batteries, the chosen storage technology eliminates maintenance requirements and improves long-term reliability, making it particularly well-suited for autonomous sensor nodes in indoor energy harvesting applications.

Assembled Views

Below are photographs of the fully assembled node from different perspectives, including the main board and attached sensor module. The final prototype is shown in Figure 5.9.

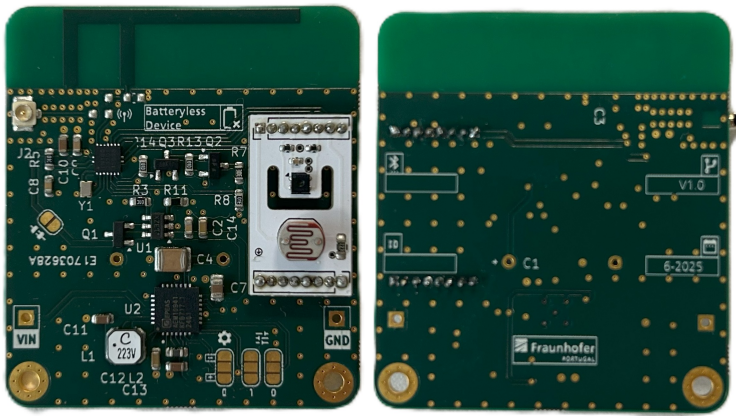

(a) (b)

Figure 5.8: Different views of the Luxor node with modular design (missing the supercapacitor).

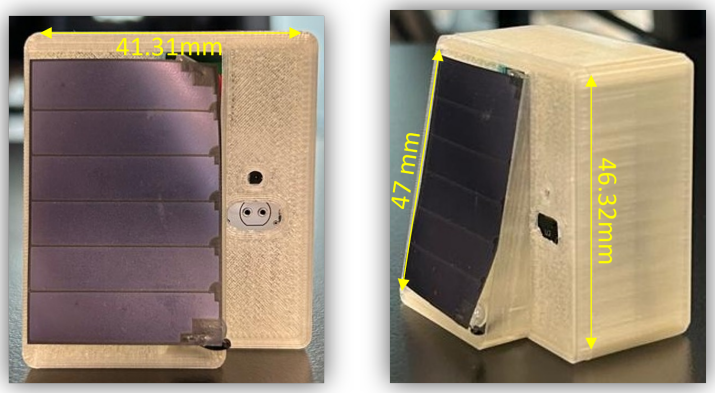

(a) (b)

Figure 5.9: Final Luxor node prototype.

5.1.1 Operatinal Logic and Flowcharts

To better illustrate the behavior of each part of the Luxor system, a set of flowcharts were developed to represent the execution logic at both hardware and software levels. These diagrams provide a visual summary of how the Luxor node operates, how the energy harvesting is managed, and how the receiver scans and processes Bluetooth transmissions.

IN100 Node Flow

The first diagram (Figure 5.10) represents the firmware execution flow of the IN100 SoC during its active phase. Upon power-up by the TPL5110 timer, the IN100 executes a minimal sequence:

- Boot and initialize internal configuration.
- Read data from the temperature and humidity sensor via I^2C.

- Measure the voltage of the supercapacitor.
- Advertise the collected data via BLE.
- Enter sleep mode, awaiting the TPL5110 to cut power.

This approach ensures minimal power usage, with the node remaining fully off between cycles.

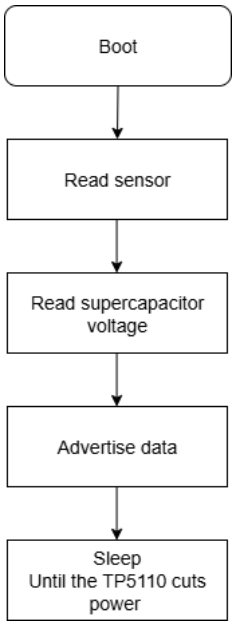

Figure 5.10: IN100 firmware execution flow during a single active cycle.

Full Node Behavior

The complete system logic, including the energy harvester (AEM10941), hardware timer (TPL5110), IN100 SoC, and sensor, is represented in the second diagram (Figure 5.11). This diagram shows how energy is harvested and monitored continuously until sufficient voltage is reached. Then, the timer is activated to begin periodic sensing cycles.

Each 30-minute cycle follows this sequence:

- AEM10941 monitors supercapacitor charge and triggers the timer.
- TPL5110 powers the IN100 and waits for a “Done” signal.
- IN100 boots, reads sensor and voltage, advertises via BLE, and signals completion.
- TPL5110 cuts power and waits for the next scheduled activation.

In this implementation, the AEM10941 thresholds were configured for a dual-cell supercapacitor setup, with a **charge-ready voltage of 3.67 V** (V_{CHRDY}) and an **overdischarge limit of 2.80 V** (V_{DIS}). These thresholds ensure that the node only starts a measurement cycle when enough energy

is available to complete sensing and transmission, while also protecting the storage element from excessive discharge and degradation, as recommended by the manufacturer's datasheet [10].

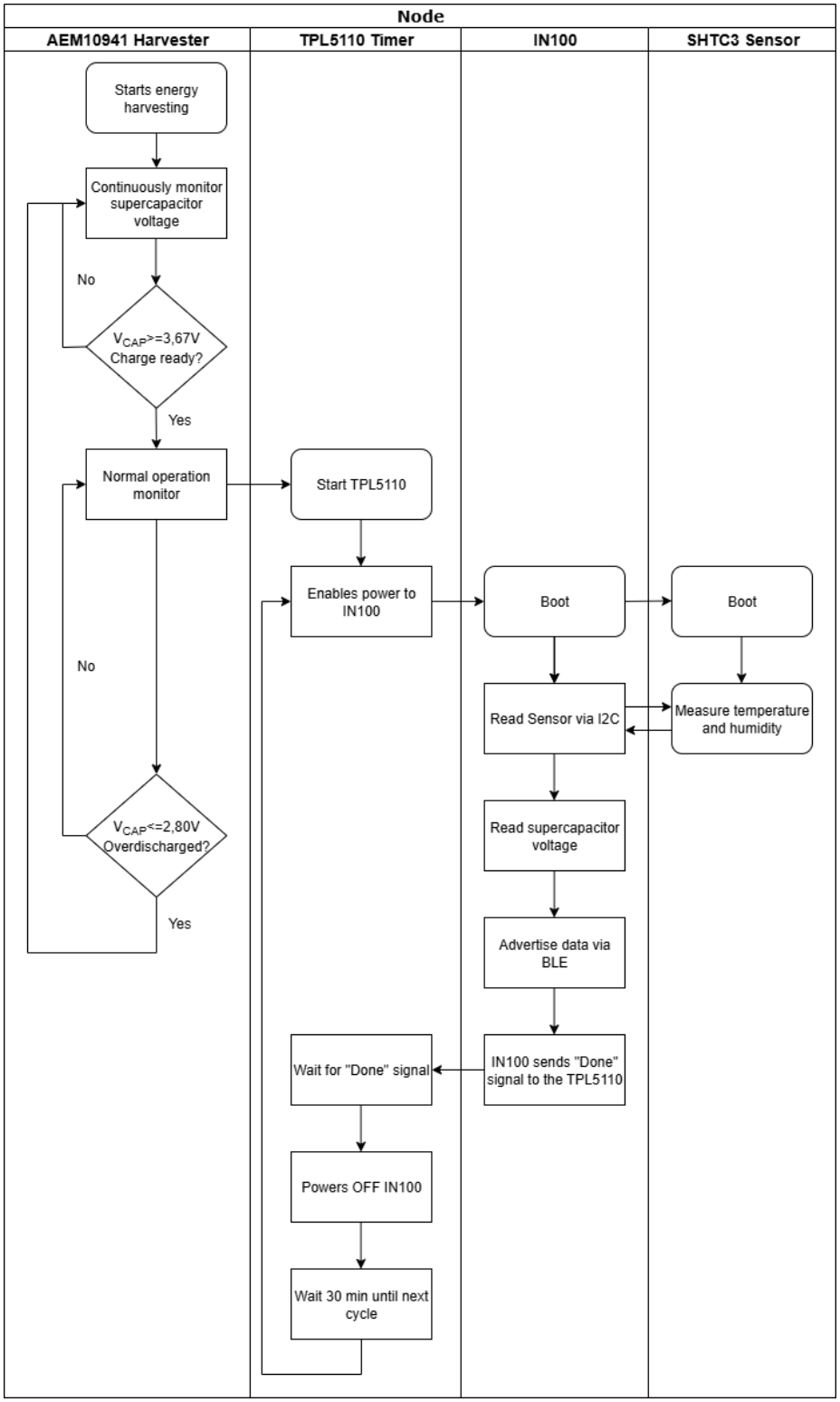

Figure 5.11: Overall flowchart of the batteryless node including energy harvester, timer, IN100, and sensor logic.

BLE Scanner Receiver Flow

On the receiver side, a lightweight scanning infrastructure was implemented to receive BLE advertisements continuously from multiple nodes. The system is based on USB BLE dongles attached to a Raspberry Pi, which acts as the central collection unit. This setup was chosen due to its low cost, scalability, and ability to operate multiple dongles in parallel, thus increasing reception reliability in dense deployments.

The last diagram (Figure 5.12) details the logic of the scanning system implemented on the receiving USB dongles connected to the Raspberry Pi. The scanner is continuously running, searching for BLE advertisements from nodes named “Luxor”.

Once a Luxor device is detected, the received data is sent via USB to a local processing unit for storage or further analysis.

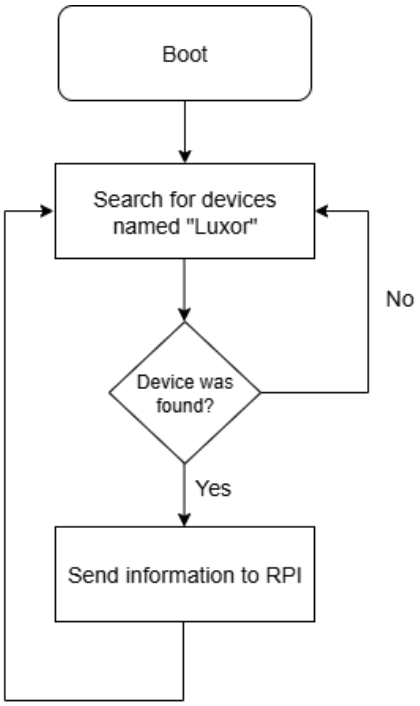

Figure 5.12: Flowchart of the BLE scanning receiver, responsible for decoding and forwarding Luxor node data.

These diagrams summarize the interaction between components and the lightweight firmware strategy employed to achieve fully autonomous, energy-efficient operation.

The following sections present the empirical results obtained through various indoor communication and energy-harvesting trials using the Luxor node.

5.2 Preliminary Communication Testing

Initial tests focused on validating the communication capabilities of the developed nodes. Specifically, RSSI was measured in a range of indoor scenarios, comparing performance using both

internal and external antennas.

5.2.1 RSSI-Based Range Tests

To evaluate the wireless communication range and reliability, multiple RSSI measurements were collected in varied indoor scenarios across the building. These included open-space environments, corridors and enclosed rooms as shown in 5.13. Tests were conducted using nodes with two antenna configurations:

- **External Antenna:** A Molex 2.4 GHz antenna connected via U.FL.
- **Internal PCB Antenna:** Integrated directly on the node PCB.

(a) (b) (c)

(d) (e) (f)

Figure 5.13: RSSI testing with external and internal antenna: various indoor scenarios.

In almost all the test scenarios, the average RSSI values with external antennas were slightly better, indicating a stronger and more reliable reception compared to internal PCB antennas. In

addition to antenna comparison, the RSSI tests were crucial in identifying the optimal TX power setting for each deployment scenario. As detailed in Appendix G, the best-performing power level fluctuated based on environmental factors such as line of sight, barriers, and room shape. Significantly, in several locations, reduced TX power levels provided a sufficient signal quality and stability, proving it was not necessary to use higher ones. These results directly guided deployment strategies, allowing for a careful balance between energy efficiency and communication robustness.

5.2.2 Impact of Simultaneous Scanning on Packet Reception

Simultaneous scanning experiments were conducted in a controlled laboratory environment (Figure 5.14) to assess the ability of the system to interpret concurrent transmissions. One transmitting node was deployed, configured with randomized start time and fixed transmission interval, while three scanning devices monitored the channel simultaneously. A central receiver logged successful detections and associated RSSI. The node was configured using the NanoBeacon Config tool [24]. Due to the limited flashing capabilities of the IN100 platform [21], which only supports firmware loading through vendor-provided tools and does not allow direct code modification or debugging, precompiled firmware had to be used.

Figure 5.14: Simultaneous scanning setup in the laboratory. The transmitting node is circled in **red**, while the scanning devices are highlighted in **yellow**.

In wireless systems where multiple devices transmit during overlapping time slots, packet collisions are a primary reason for reception failures. When two or more packets overlap in time and frequency, the receiver often struggles to decode them accurately, leading to higher packet loss. This impact intensifies as the count of simultaneous transmissions increases, as the likelihood of collisions escalates non-linearly with network density.

Simultaneous scanning addresses this limitation by deploying multiple receivers that simultaneously monitor the same channel. If one scanner is unable to decode a packet due to interference or timing issues, another scanner may still successfully capture it. This redundancy increases the actual likelihood of packet recovery and strengthens the resilience of the system during high-load situations. Moreover, the spatial variation of the scanning devices can additionally minimize losses, since signal quality fluctuates based on antenna alignment and local multipath scenarios.

Packet loss increased progressively with the number of simultaneous transmissions. However, nodes using external antennas consistently yielded higher successful decoding rates, confirming that both antenna design and multi-receiver scanning strategies play a key role in ensuring reliable packet reception under dense transmission scenarios.

5.2.3 First Real Node Evaluation: Energy-Harvesting Test with Solar Panel

Until this point, all functional tests had been performed with the node powered via USB and reprogrammed at each run using `Run in RAM`. Due to IN100's architectural constraint of being flashable only once [21], this approach was necessary during the development stage. However, it did not reflect the final intended mode of operation, which corresponded to perpetual energy-autonomous execution.

Previous BLE communication tests with the prototype nodes (Section 5.2.2) revealed non-negligible packet loss, with effectiveness as low as 78–88% in some scenarios. A simple approach to reduce these losses might have been to raise the quantity of advertising packets during each sensing cycle. This method would greatly raise the power consumption of the Luxor node, which is especially detrimental for an ultra-low-power energy-harvesting design functioning within strict energy constraints.

Instead, a more power-efficient and system-responsible solution was adopted: increasing the number of BLE receivers (dongles). Since the USB dongles operate on continuous external power, they can scan indefinitely without power constraints. By placing multiple synchronized scanners in proximity to the node, the effective coverage and redundancy of the detection system improves without imposing additional energy burden on the transmitting side. This design decision aligns with the project's architectural philosophy: preserving the energy integrity of the sensing node while distributing the cost of reliability to the more power-rich infrastructure.

Initial Four-Day Test

To validate true autonomous performance, a fully untethered test was conducted using the following configuration:

- Solar panel: **BCS4430B6** film-based module (chosen for aesthetic and dimensional compatibility with the node).
- Energy storage: **0.47 F supercapacitor**.

- Firmware configuration: wake every 30 minutes, two ADC readings per cycle, signal power level set to 2, random advertisement delay between 0–10 ms, and an advertisement interval of 1000 ms.

- Oscillator configuration matched the LFXTAL081614 crystal datasheet.

During this experiment, the node was placed approximately 1 meter away from **two** Nordic USB dongles configured to scan in parallel. The goal was to verify full energy autonomy and track how often both dongles failed to detect a transmitted message.

Results: Over a 4-day continuous experiment, a total of 194 messages were scheduled. Only **2 messages** were missed by both dongles (1 on Day 1, 1 on Day 2), resulting in:

$$\text{Effectiveness} = \left(\frac{192}{194}\right) \times 100 \approx \mathbf{98.97\%}$$

Table 5.1: Message transmission results (Luxor 1 test).

Metric	**Day 1**	**Day 2**	**Day 3**	**Day 4**	**Total**
Messages Sent	48	49	48	49	194
Messages Failed (Both)	1	1	0	0	2
Messages Received (Both)	47	48	48	49	192
Effectiveness (%)	97.92%	97.96%	100.00%	100.00%	**98.97%**

Extended Multi-Day Evaluation

To further validate long-term stability, a second experiment was performed over several days using **three** Nordic nRF52 dongles as BLE receivers [27], replacing the ESP32-based scanners. Two nodes were deployed:

- **Node 1:** Charged before deployment, operated with solar panel connected throughout (Figure 5.15).

- **Node 2:** Initially with solar panel connected, later without it, operating from stored energy alone (Figure 5.16). This is the same node whose results are in the Figures 5.17 and 5.18.

Table 5.2: Extended message transmission and detection results over several days for both nodes.

Metric	**Node 1**	**Node 2**	**Mean**
Messages Sent	585	324	454.5
Messages Failed (Both)	5	3	4
Messages Received (Both)	580	321	450.5
Effectiveness (%)	99.14%	99.07%	**99.11%**

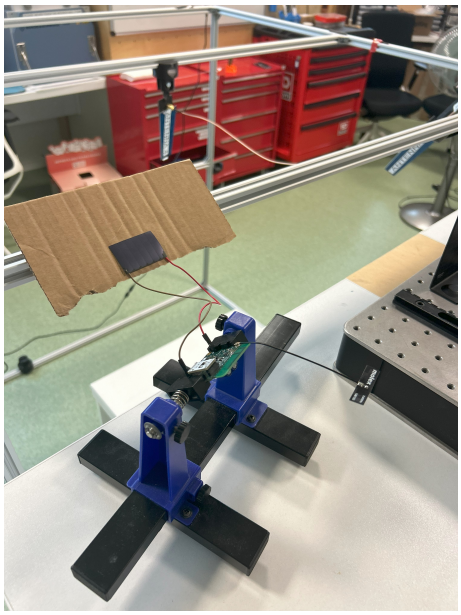

Figure 5.15: Node 1 during initial deployment with solar panel attached.

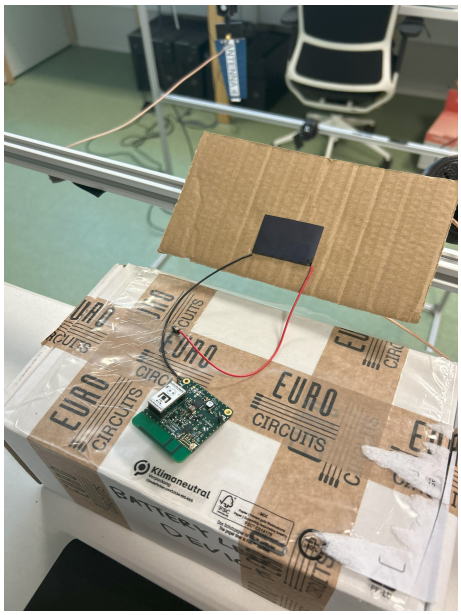

Figure 5.16: Node 2 operating without solar panel after the initial harvesting phase (same node used in charging/discharging tests).

Energy Lifecycle Tests

In addition to the detection tests, charging and discharging behavior of the Luxor node was assessed to evaluate its full lifecycle autonomy. The node was initially fully discharged and placed under indoor lighting with the solar panel connected. The time required to accumulate enough energy (i.e., reaching the startup threshold of 3.67 V) and send the first BLE message was monitored, as shown in Figure 5.17.

Following this charging phase, the panel was disconnected and the node was allowed to continue operating solely from the stored energy (i.e., discharging phase). This procedure demonstrates how long the node can sustain operation without any energy harvesting, as illustrated in Figure 5.18.

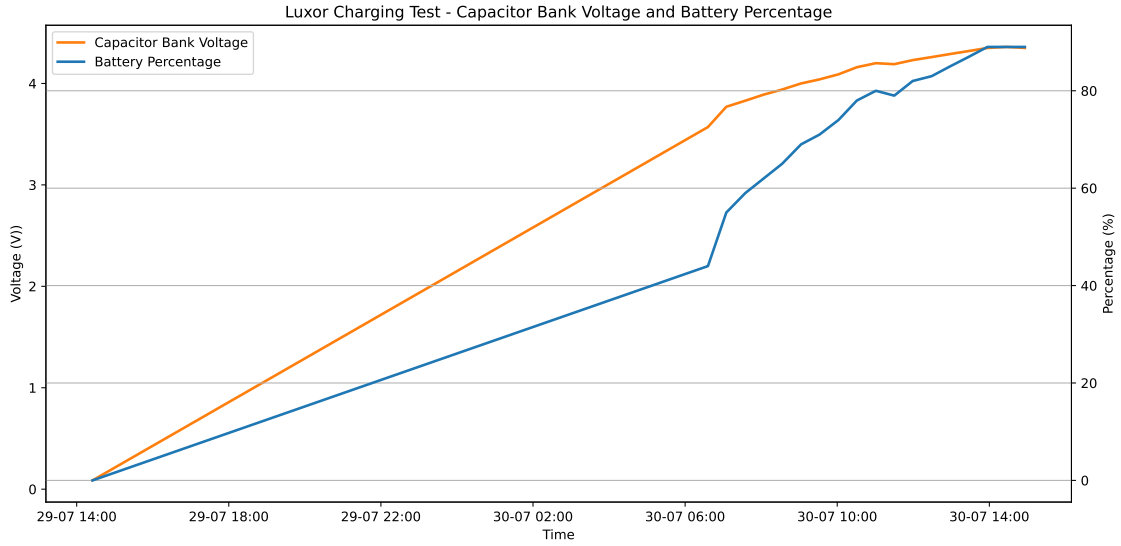

Figure 5.17: Luxor charging test: Capacitor bank voltage and estimated battery percentage under ambient light with solar panel connected.

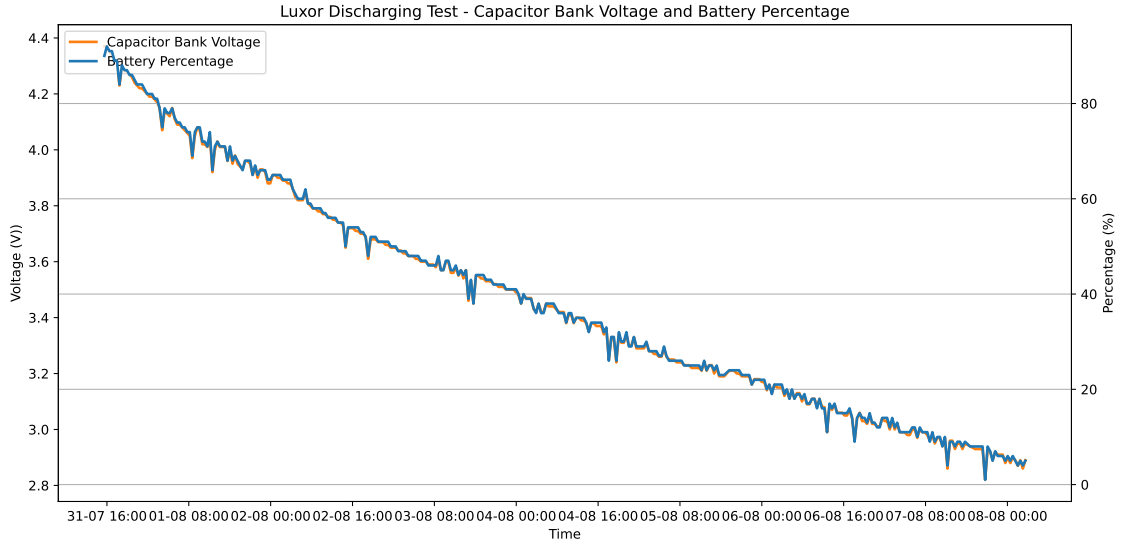

Figure 5.18: Luxor discharging test: Capacitor bank voltage and estimated battery percentage after disconnecting the solar panel.

These experiments confirm the Luxor node's ability to cold-start, harvest energy autonomously, and sustain operation under realistic indoor lighting conditions. Furthermore, they validate the effectiveness of its ultra-low-power design, showing that the node can extend runtime even without

continuous energy input.

Overall, both the short-term and extended multi-day results demonstrate that the Luxor node operates in a **truly batteryless, autonomous fashion**, maintaining stability and timing accuracy over multiple days. The achieved detection rates of nearly 99% confirm the effectiveness of the multi-scanner strategy. This architectural decision proved especially beneficial given the energy limitations of the node and the known unreliability of the IN100 breakout boards, which can suffer from degraded radio performance due to the use of suboptimal 26 MHz crystals [21]. By offloading redundancy to the receiver side, the system successfully avoids excessive energy draw from the node while achieving reliable BLE data collection in real-world conditions.

5.3 Deployment and Final Testing

Final real-world testing involved the deployment of five fully assembled Luxor nodes across different areas of the building to evaluate coverage, reliability, and performance in realistic operating conditions. The objective was to assess how the system behaves in a multi-node configuration under varying lighting conditions, obstructions, and interference sources.

At this stage, all five nodes were operating as intended. Based on the observed behavior, the **settling time** (the period required for nodes to reach stable operation after deployment) was approximately **two days**. This duration varied depending on the initial charging state of each node and its specific location, especially the level of light exposure available for energy harvesting.

The deployment plan placed nodes strategically in both enclosed rooms and open office spaces, while two Nordic USB dongles were positioned to ensure maximum detection coverage. Table 5.3 details the exact configuration of each node.

Table 5.3: Final deployment configuration for multi-node test.

Device	TX Power (dBm)	MAC Address
1	2	00:00:00:00:01
2	2	00:00:00:00:02
3	2	00:00:00:00:03
4	2	00:00:00:00:04
5	2	00:00:00:00:05

Dongle Placement

To maximize packet detection, the three USB dongles were placed in a central elevated location (Figure 5.19), ensuring that all nodes were within effective detection range. The dongles were connected to a Raspberry Pi 4 running continuous BLE scanning software.

Figure 5.19: Close-up of USB dongles used for multi-node scanning.

Deployment Map and Locations

Figures 5.20 and 5.21 show the Fraunhofer office floor plan and the final positions of all five Luxor nodes. Nodes 1 (red) and 3 (grey) were placed in enclosed rooms to assess performance under partial RF isolation, while Nodes 2 (green), 4 (orange), and 5 (pink) were deployed in open-space areas to evaluate performance in less obstructed environments but with greater potential interference from other wireless devices.

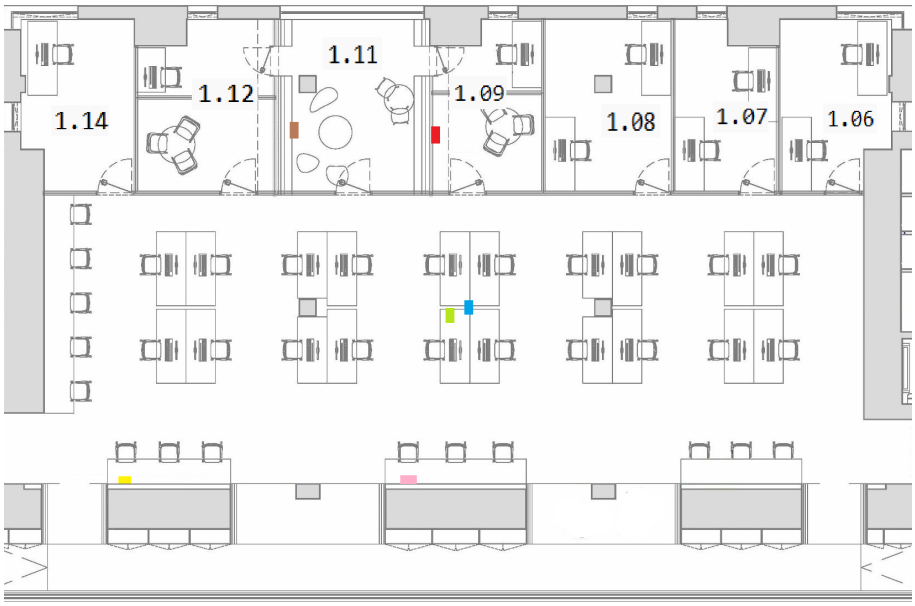

Figure 5.20: Fraunhofer office floor plan with Luxor node positions: Node 1 (red), Node 2 (green), Node 3 (brown), Node 4 (orange), Node 5 (pink).

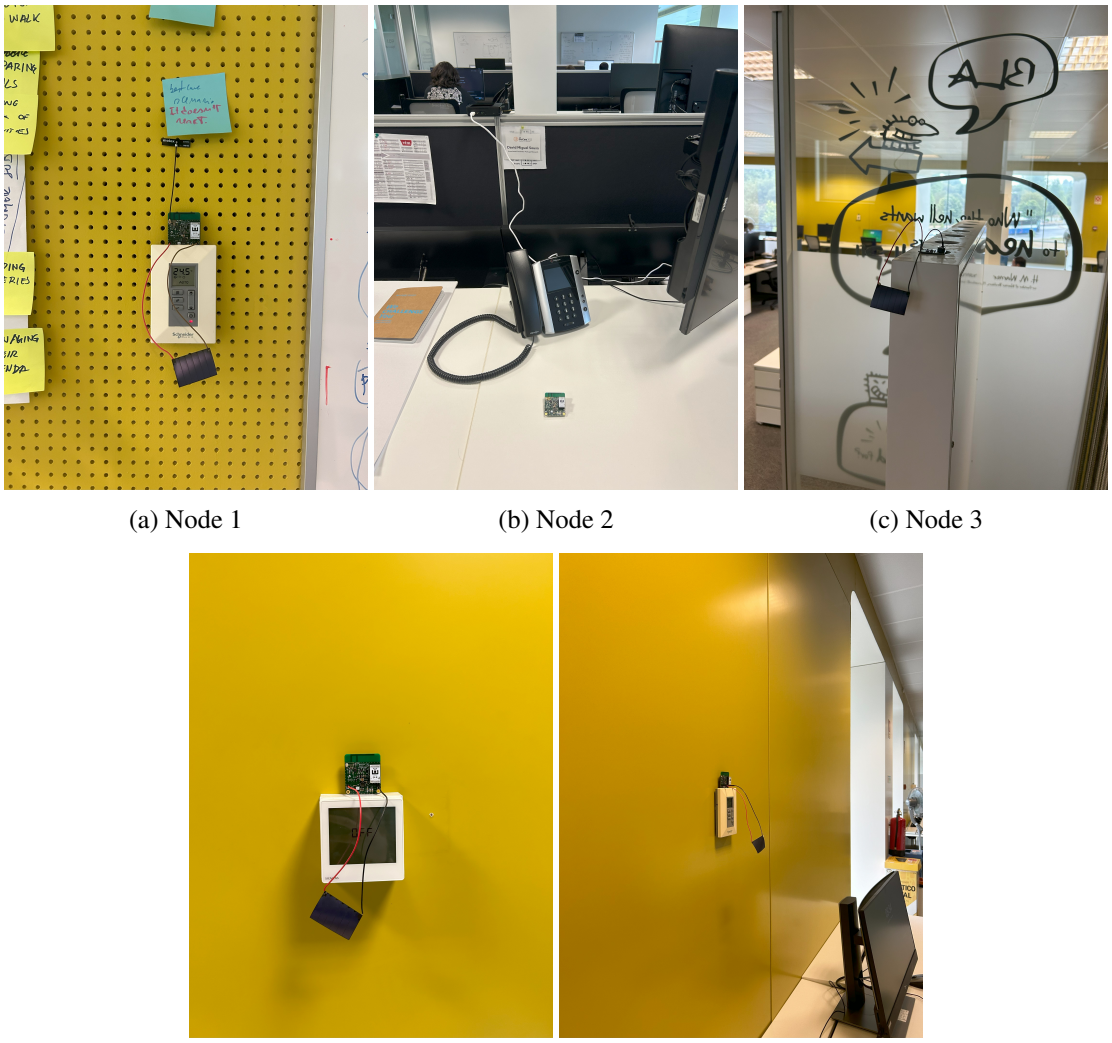

(a) Node 1 (b) Node 2 (c) Node 3

(d) Node 4 (e) Node 5

Figure 5.21: Final deployment locations of the five Luxor nodes across the Fraunhofer office.

ADC Channels and Sampling Behaviour

The Luxor nodes were configured with different ADC channel setups based on insights from initial testing. - Nodes 1 and 2: a single active ADC channel, sending a total of **4 messages** per measurement cycle, with the first **2 messages** discarded due to transient noise during initial readings. - Nodes 3, 4, and 5: also using a single active ADC channel, but configured to send **8 messages** per cycle, with the first **4 messages** discarded. This configuration change was introduced after observing from early tests with Nodes 1 and 2 that additional messages improved the stability and accuracy of the recorded values.

This filtering approach ensures that only stable, noise-free data is used for analysis, improving measurement reliability without increasing the energy consumption of the node.

Dashboard Interface

A custom dashboard was developed to monitor the deployed Luxor nodes in real time. This interface, built by Diogo Gonçalves, a colleague at Fraunhofer, uses *Home Assistant* as the underlying platform. It provides a visual summary of sensor readings (temperature, humidity), energy status (voltage, supercapacitor charge level), communication statistics, and uptime information.

Figure 5.22 shows an example from Node 4, highlighting:

- Real-time temperature and humidity trends.
- Energy harvesting performance, including voltage and charge percentage.
- Message detection statistics, including estimated packet loss and downtime.

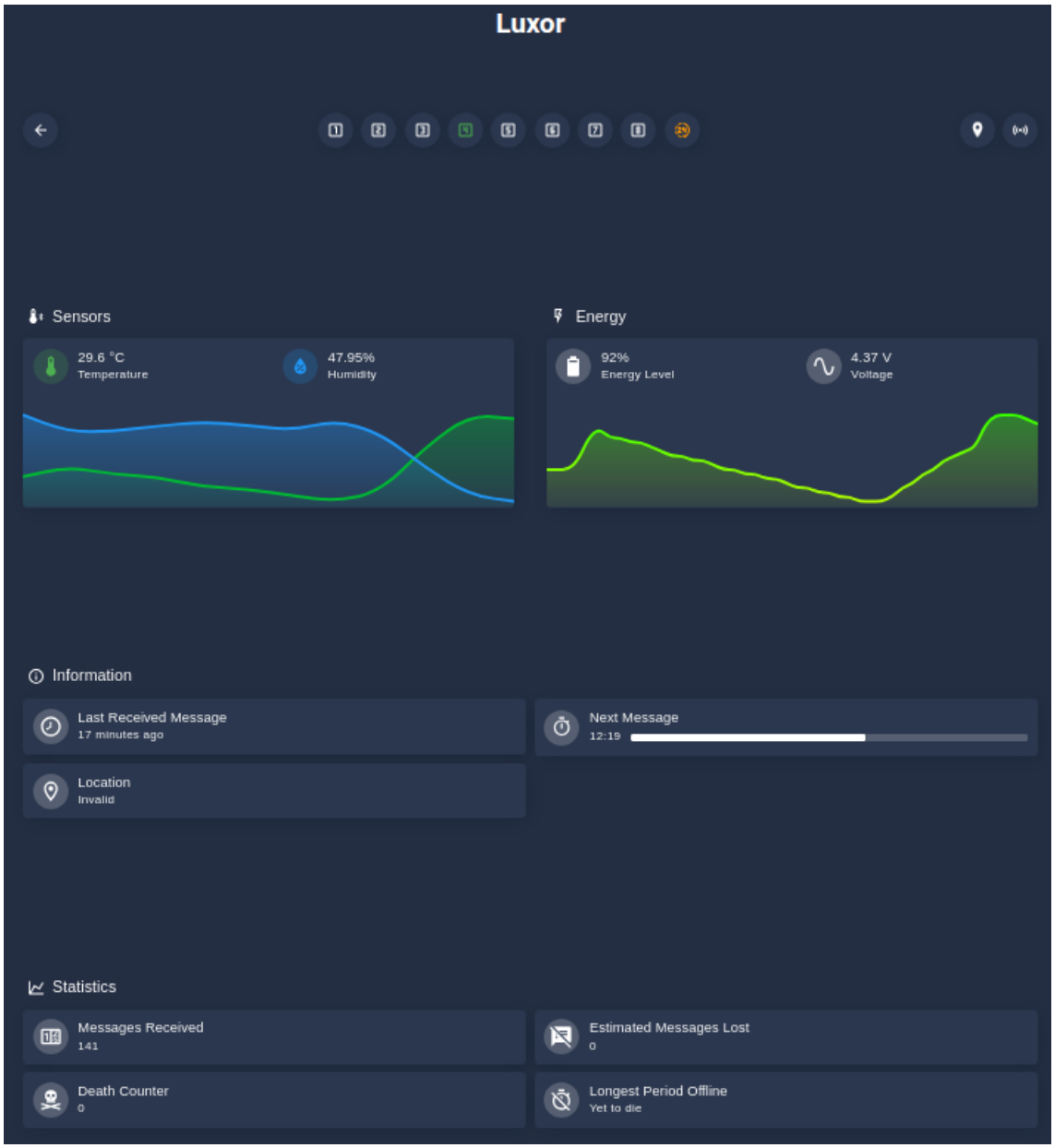

Figure 5.22: Example of the Luxor monitoring dashboard (Node 4), developed in Home Assistant by Diogo Gonçalves at Fraunhofer. The interface displays sensor data, energy status, and communication metrics in real time.

The testing period lasted several days, ensuring that each node experienced varying lighting conditions, occupancy patterns, and interference scenarios. This setup allowed for a comprehensive evaluation of packet detection rates, latency, and energy-harvesting performance in realistic indoor deployment scenarios.

Table 5.4 summarizes the extended message transmission and detection results for the five deployed nodes. Node 3 did not provide usable data due to deployment constraints (the solar panel was not properly soldered), so mean values were calculated over the four active nodes. Overall, the system maintained high reliability across all locations: effectiveness remained above 98% for ev-

ery node, with Node 5 achieving the best performance at 99.34%. The average effectiveness across the deployment was 98.80%, confirming that the Luxor nodes can sustain long-term autonomous operation while maintaining highly reliable BLE communication.

Table 5.4: Extended message transmission and detection results over several days for the five deployed nodes.

Metric	**Node 1**	**Node 2**	**Node 3**	**Node 4**	**Node 5**	**Mean**
Messages Sent	1398	860	–	790	755	950.8
Messages Failed	26	12	–	7	5	12.5
Messages Received	1372	848	–	783	750	938.3
Effectiveness (%)	98.14%	98.60%	–	99.11%	99.34%	**98.80%**

5.4 Summary and Observations

The final implementation and testing phases demonstrated that the **Luxor node** successfully meets its design goals of being a batteryless, energy-harvesting, autonomous sensing platform for indoor environments. Across both controlled laboratory experiments and real-world multi-day deployments, the system consistently achieved high data detection rates while operating within strict energy constraints.

Communication trials confirmed that:

- **External antennas** provide the highest detection reliability, particularly in scenarios involving partial RF isolation or multiple structural barriers.
- **Internal PCB antennas** are suitable for short-range or unobstructed deployments, but show reasonable performance under obstruction.
- **Multi-scanner detection** significantly reduces packet loss without increasing node energy consumption, removing redundancy from the receiver infrastructure.

Simultaneous scanning tests showed that the system can reliably handle multiple concurrent transmissions for low-data-rate applications, although packet loss increases when the number of active transmitters exceeds four. The choice to keep each node's advertisement rate low, combined with strategic placement of multiple USB dongles, proved to be an effective balance between reliability and ultra-low-power operation.

Energy-harvesting evaluations demonstrated:

- Cold-start capability from indoor light and autonomous operation sustained entirely by a small solar panel and 0.47 F supercapacitor.
- Stable operation over multiple days, with extended runtime even without continuous energy input.

- High detection effectiveness in real deployments—98.97% in a four-day single-node test, 99.11% in an extended two-node evaluation, and **98.80% in the final five-node deployment** (Table 5.4).

The multi-node deployment further confirmed that the system maintains reliable BLE communication in mixed open-space and enclosed-room layouts, even with varying light levels and potential interference sources. Node effectiveness remained consistently above 98%, with Node 5 achieving the best performance at 99.34%. This highlights the robustness of the Luxor architecture under realistic multi-node conditions. Filtering of initial ADC samples ensured that only stable sensor data was transmitted, enhancing measurement accuracy without added energy cost.

Overall, the results validate the Luxor node as a robust, scalable, and energy-resilient platform for indoor IoT sensing. By pairing ultra-low-power node design with strategically placed, continuously powered receivers, the system achieves high reliability without compromising the energy autonomy of the sensing units.

Chapter 6

Conclusions and Future Work

6.1 Contributions

This dissertation presented the design, implementation, and real-world validation of a fully batteryless sensing node optimized for long-term indoor deployment. By combining photovoltaic energy harvesting with ultra-low-power operation [13, 17], the system achieves perpetual autonomy without battery replacements or human intervention, addressing sustainability goals in modern IoT infrastructures [43].

The main contributions of this work are:

- **Energy Source Evaluation:** A detailed comparison of indoor harvesting sources, including solar [30], thermal [8], kinetic, and RF harvesting [29], demonstrated that photovoltaic harvesting is the only consistently viable option for office lighting conditions.
- **Node Design and Energy Architecture:** Development of an optimized energy-harvesting node architecture using the LL200-2.4-75 solar panel [30], AEM10941 energy management unit [10], and a tailored supercapacitor bank. The system features cold-start capability, voltage regulation, and storage sized for a 30-minute sensing cycle [19].
- **Platform Optimization:** Comparative evaluation between the Riotee system [25] and the IN100 NanoBeacon [39] identified the IN100, combined with a TPL5110 timer [41] and SHTC3 sensor [36], as the most energy efficient and deployment ready option.
- **Multi-Node Real-World Deployment:** A complete five-node deployment was executed throughout the Fraunhofer office (Figure 5.20). All nodes operated as expected, with a typical settling time of around two days to achieve stable operation, depending on pre-deployment charge and light exposure. This confirmed stable BLE reception, perpetual operation, and reliable sensing performance in diverse indoor lighting and interference conditions.
- **Sampling Strategy and Noise Mitigation:** Nodes 1 and 2 sent four messages per measurement cycle, discarding the first two to remove transient noise. Nodes 3–5 sent eight

messages, discarding the first four. This approach ensured stable, noise-free data without additional energy cost.

- **Data Integration and Visualization:** Sensor data from deployed nodes was integrated into a Home Assistant dashboard, developed by the Fraunhofer colleague Diogo Gonçalves. This dashboard (presented in Chapter 5) displays real-time temperature and humidity values and device status for each node.

These contributions collectively demonstrate the feasibility of maintenance-free, energy-autonomous BLE sensor nodes for sustainable IoT applications in modern office environments.

6.2 Identified Limitations

Although the system met its performance targets, several limitations were identified:

- **Dependence on Illumination:** Performance is directly tied to available light. In lower-light spaces (e.g., Meeting Room 1.11), operation stability is reduced without adaptation [15].
- **Energy Storage Leakage:** Supercapacitors provide fast charging and long cycle life, but leakage currents can lead to slow energy loss during prolonged low-light conditions [18].
- **RF Attenuation:** BLE range was sufficient for most scenarios but degraded with walls and furniture, even with multiple receivers [37].
- **Fixed Duty Cycle:** The nodes used a fixed wake-up interval and advertisement configuration, lacking adaptive energy-aware operation [38].
- **Platform-Specific Design:** The firmware and power architecture are tailored to the IN100 platform [39]. Migration to different hardware would require substantial adjustments [45].
- **Flexible Solar Panel Availability:** The flexible solar panel used in the prototype has been discontinued by the manufacturer. While its flexibility offers mechanical advantages and easy integration on curved or uneven surfaces, it also presents drawbacks such as mechanical fragility and difficulty in soldering electrical connections, which complicates assembly and long-term reliability.

6.3 Future Development Opportunities

Building on this work, several promising research and development directions emerge:

- **Energy-Aware Adaptation:** Implementing real-time adjustment of sensing rates based on stored energy and forecasted harvesting could improve resilience in variable lighting conditions [22].

- **Hybrid Harvesting:** Combining photovoltaic harvesting with RF or kinetic sources [4] could enhance robustness in extended low-light scenarios.
- **Emerging low-light photovoltaic technologies:** The industry is rapidly developing energy harvesters optimized for low-lumen indoor conditions, expanding the viability of batteryless nodes in dimly lit environments such as offices, warehouses, or display cases [20].
- **Protocol Enhancements:** Adding BLE mesh or synchronization features could enable multi-hop communication and time-aligned sensing [33].
- **Extended Field Trials:** Long-term deployments in outdoor, industrial, or heritage sites could validate multi-year durability and maintenance-free performance [2].
- **Packaging and Integration:** Improved enclosure design for robustness, reduced form factor, and seamless architectural integration [7].

In conclusion, this dissertation establishes a practical, sustainable, and fully autonomous IoT sensing platform. The success of its five-node deployment demonstrates its readiness for scaled deployments, paving the way for future smart sensing systems that are robust, adaptive, and truly maintenance-free.

Appendix A

LIGHTED Schematic

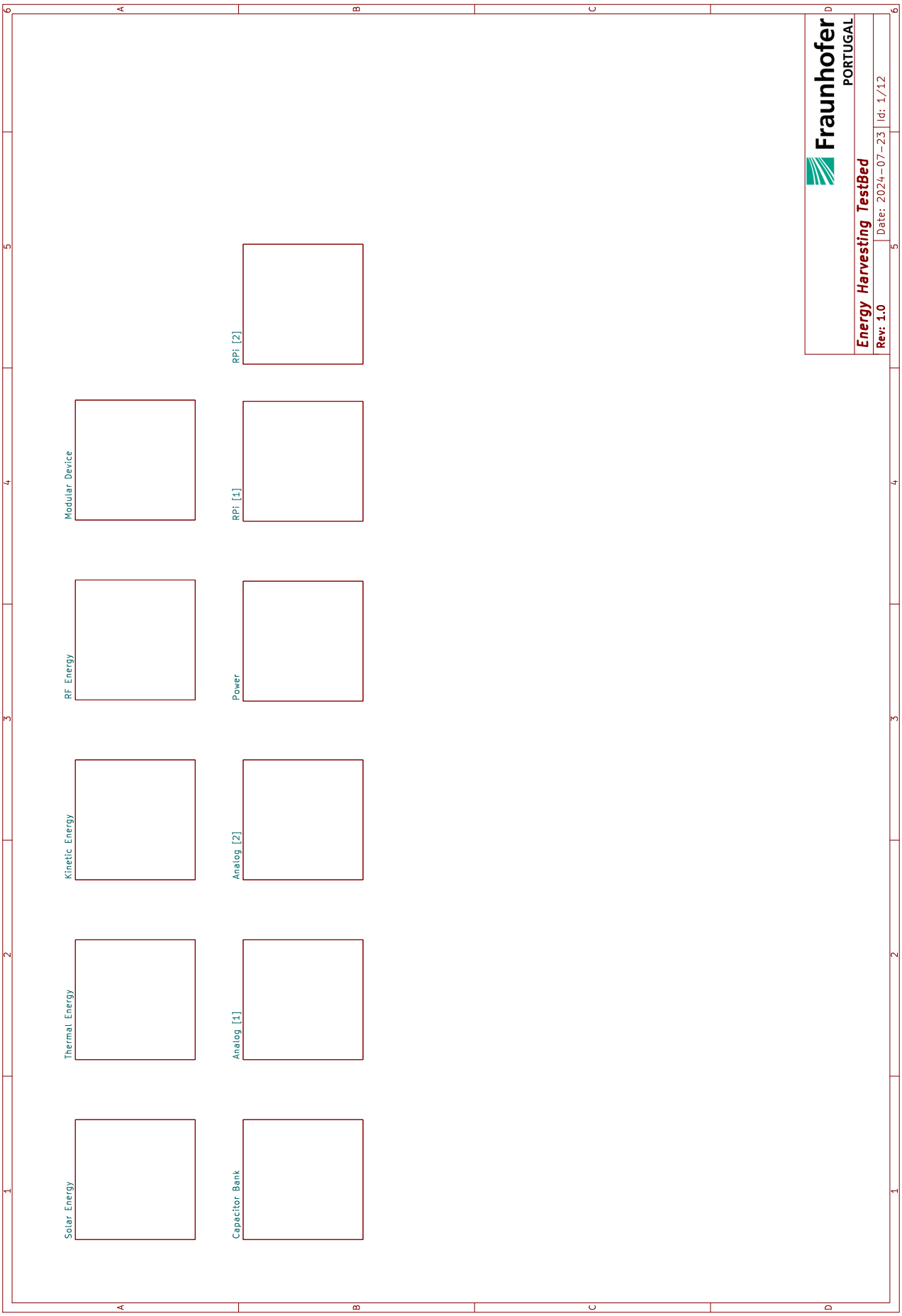
Fraunhofer
PORTUGAL
Energy Harvesting TestBed
Rev: 1.0
Date: 2024-07-23
Id: 1/12
Solar Energy
Capacitor Bank
Thermal Energy
Analog [1]
Kinetic Energy
Analog [2]
RF Energy
Power
Modular Device
RPi [1]
RPi [2]

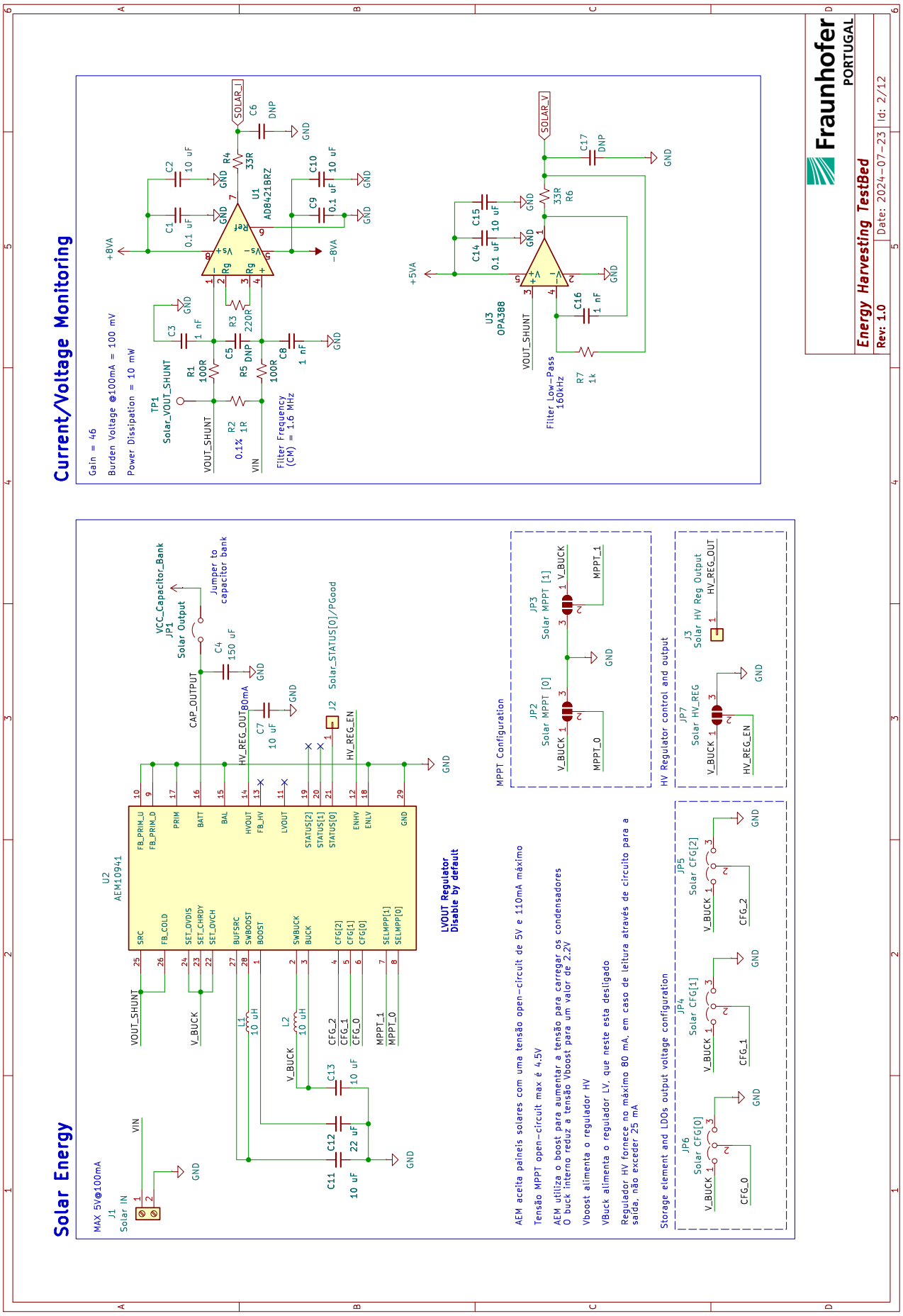
Solar Energy
Current/Voltage Monitoring
Fraunhofer PORTUGAL
Energy Harvesting TestBed
Rev: 1.0
Date: 2024-07-23
Id: 2/12
MAX 5V@100mA
J1 Solar IN
U2 AEM10941
VCC_Capacitor_Bank
JP1 Solar Output
Jumper to capacitor bank
CAP_OUTPUT
HV_REG_OUT 80mA
HV_REG_EN
Solar_STATUS[0]/PGood
LVOUT Regulator Disable by default
MPPT Configuration
JP2 Solar MPPT [0]
JP3 Solar MPPT [1]
HV Regulator control and output
JP7 Solar HV_REG
J3 Solar HV Reg Output
HV_REG_OUT
AEM aceita painéis solares com uma tensão open-circuit de 5V e 110mA máximo
Tensão MPPT open-circuit max é 4.5V
AEM utiliza o boost para aumentar a tensão para carregar os condensadores
O buck interno reduz a tensão Vboost para um valor de 2.2V
Vboost alimenta o regulador HV
VBuck alimenta o regulador LV, que neste esta desligado
Regulador HV fornece no máximo 80 mA, em caso de leitura através de circuito para a saída, não exceder 25 mA
Storage element and LDOs output voltage configuration
JP4
JP5
JP6
Solar CFG[0]
Solar CFG[1]
Solar CFG[2]
Gain = 46
Burden Voltage @100mA = 100 mV
Power Dissipation = 10 mW
TP1 Solar_VOUT_SHUNT
VOUT_SHUNT
VIN
Filter Frequency (CM) = 1.6 MHz
U1 AD8421BRZ
U3 OPA388
Filter Low-Pass 160kHz
SOLAR_I
SOLAR_V
+8VA
-8VA
+5VA
GND

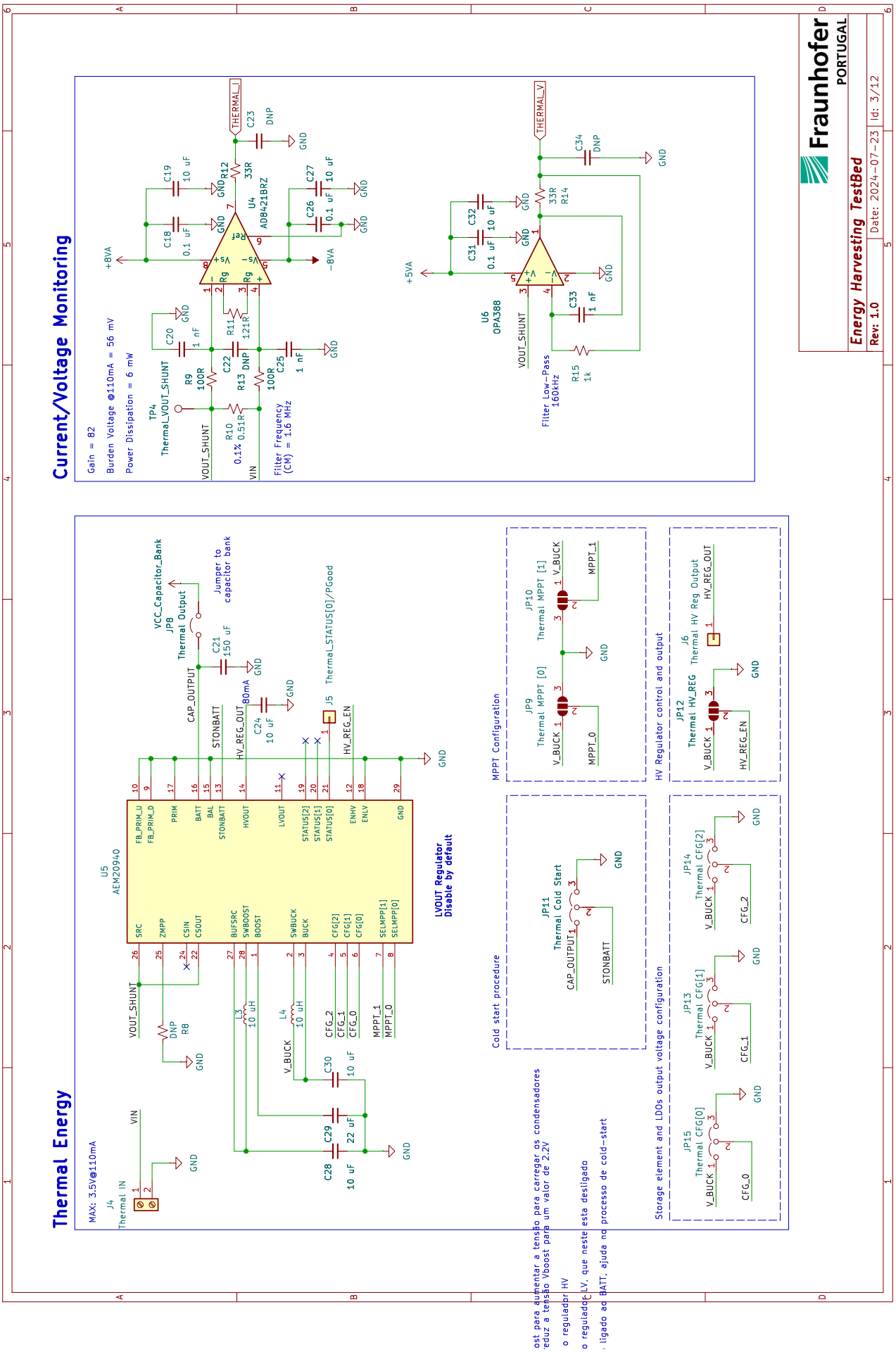
Current/Voltage Monitoring
Gain = 82
Burden Voltage @110mA = 56 mV
Power Dissipation = 6 mW
Filter Frequency (CM) = 1.6 MHz
Filter Low-Pass 160kHz
Thermal Energy
MAX: 3.5V@110mA
LVOUT Regulator Disable by default
MPPT Configuration
Cold start procedure
HV Regulator control and output
Storage element and LDOs output voltage configuration
Fraunhofer PORTUGAL
Energy Harvesting TestBed
Rev: 1.0
Date: 2024-07-23
Id: 3/12

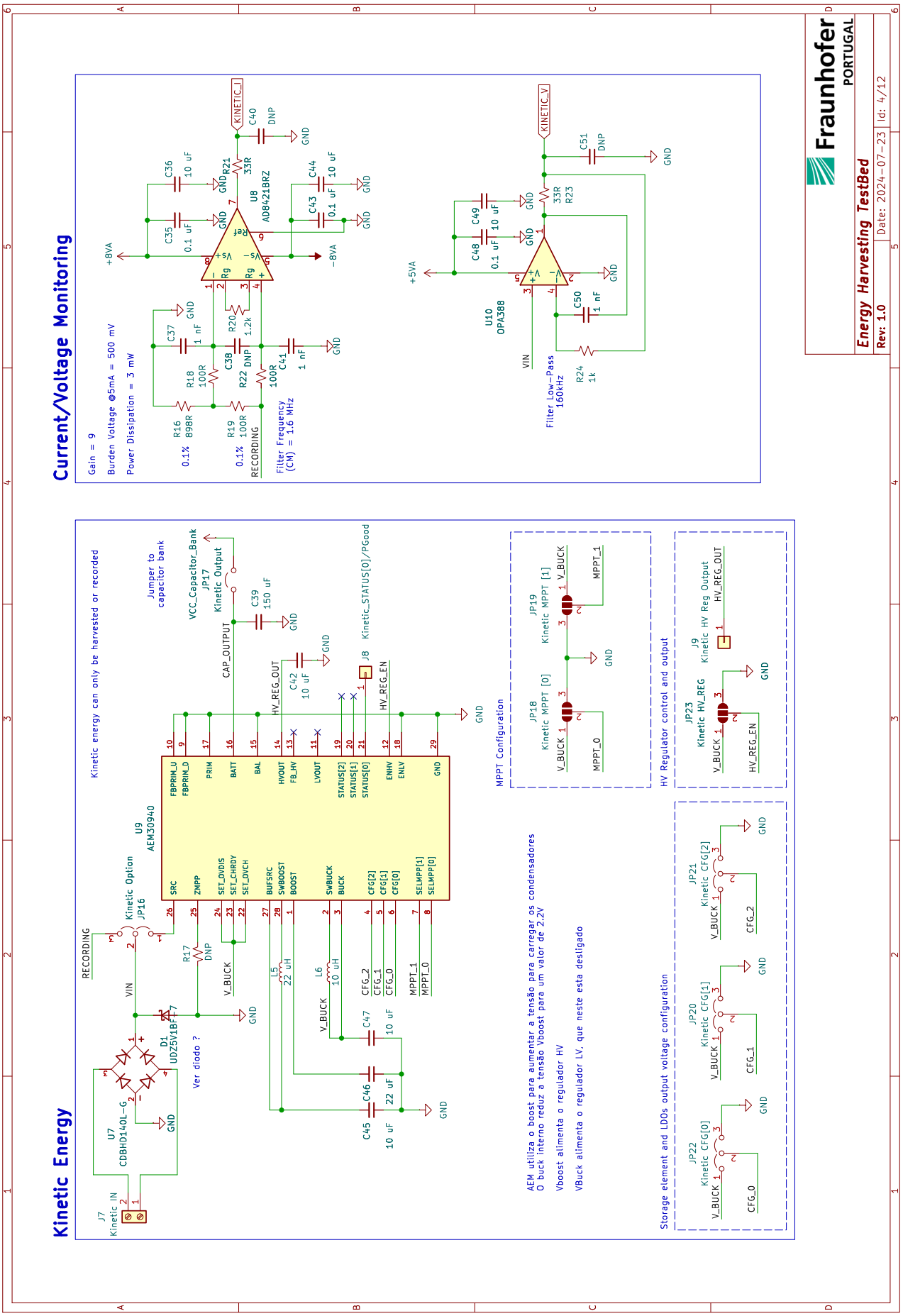
Kinetic Energy
Current/Voltage Monitoring
Fraunhofer PORTUGAL
Energy Harvesting TestBed
Rev: 1.0
Date: 2024-07-23
Id: 4/12
Kinetic energy can only be harvested or recorded
Jumper to capacitor bank
VCC_Capacitor_Bank
Kinetic Output
CAP_OUTPUT
HV_REG_OUT
HV_REG_EN
Kinetic_STATUS[0]/PGood
RECORDING
Kinetic Option
VIN
V_BUCK
U9 AEM30940
U7 CDBHD140L-G
D1 UDZ5V1BF
Ver diodo ?
MPPT Configuration
HV Regulator control and output
Storage element and LDOs output voltage configuration
AEM utiliza o boost para aumentar a tensão para carregar os condensadores
O buck interno reduz a tensão Vboost para um valor de 2.2V
Vboost alimenta o regulador HV
VBuck alimenta o regulador LV, que neste esta desligado
Gain = 9
Burden Voltage @5mA = 500 mV
Power Dissipation = 3 mW
RECORDING
Filter Frequency (CM) = 1.6 MHz
U8 AD8421BRZ
KINETIC_I
KINETIC_V
U10 OPA388
Filter Low-Pass 160kHz
+8VA
-8VA
+5VA
GND

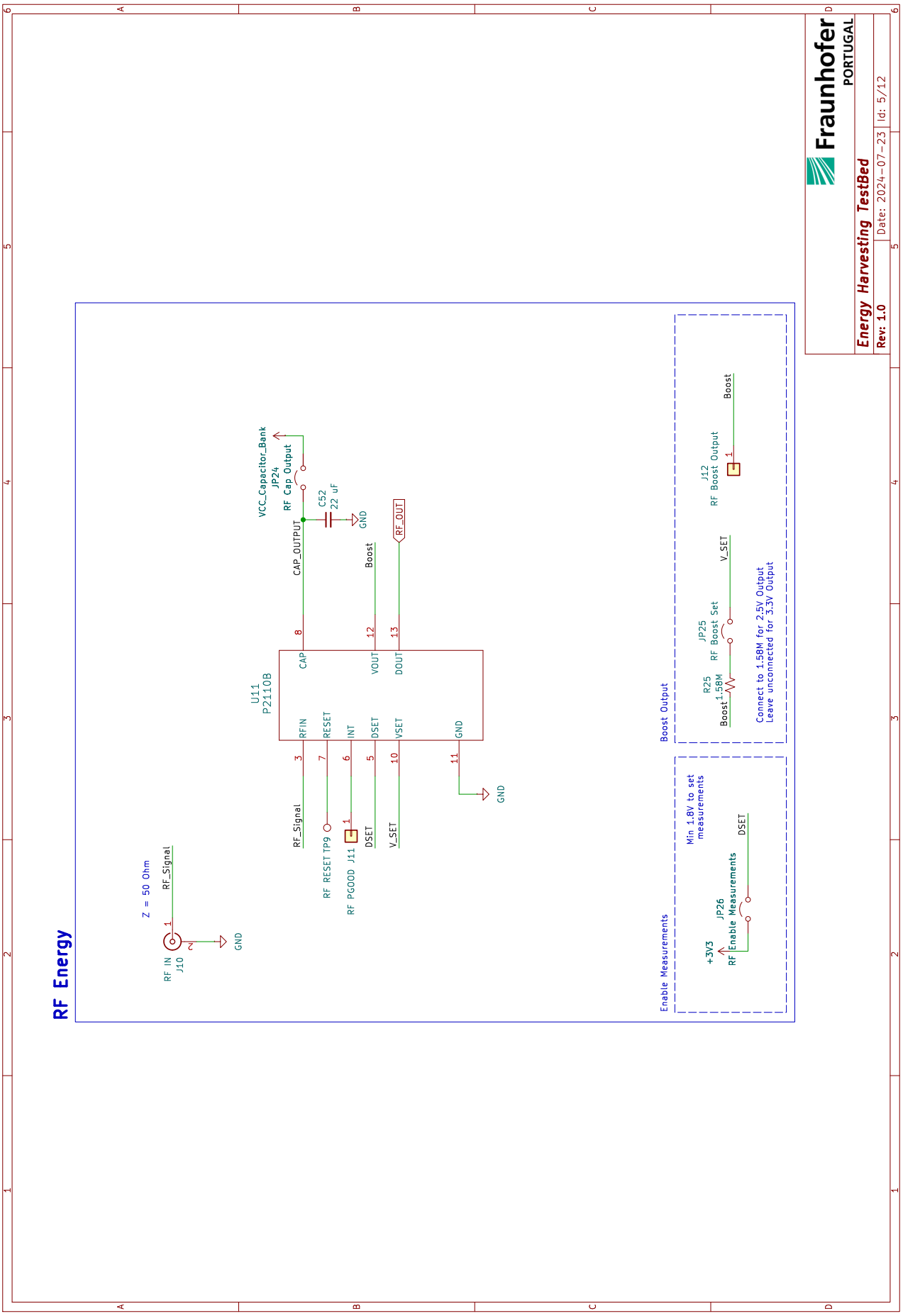
RF Energy
Energy Harvesting TestBed
Rev: 1.0
Date: 2024-07-23
Id: 5/12
Fraunhofer PORTUGAL
RF IN J10
Z = 50 Ohm
RF_Signal
GND
U11 P2110B
RFIN
RESET
INT
DSET
VSET
GND
CAP
VOUT
DOUT
RF_Signal
RF RESET TP9
RF PGOOD J11
DSET
V_SET
GND
VCC_Capacitor_Bank
JP24 RF Cap_Output
CAP_OUTPUT
C52 22 uF
GND
Boost
RF_OUT
Boost Output
J12 RF Boost Output
Boost
JP25 RF Boost Set
V_SET
R25 1.58M
Boost
Connect to 1.58M for 2.5V Output
Leave unconnected for 3.3V Output
Enable Measurements
Min 1.8V to set measurements
JP26 RF Enable Measurements
+3V3
DSET

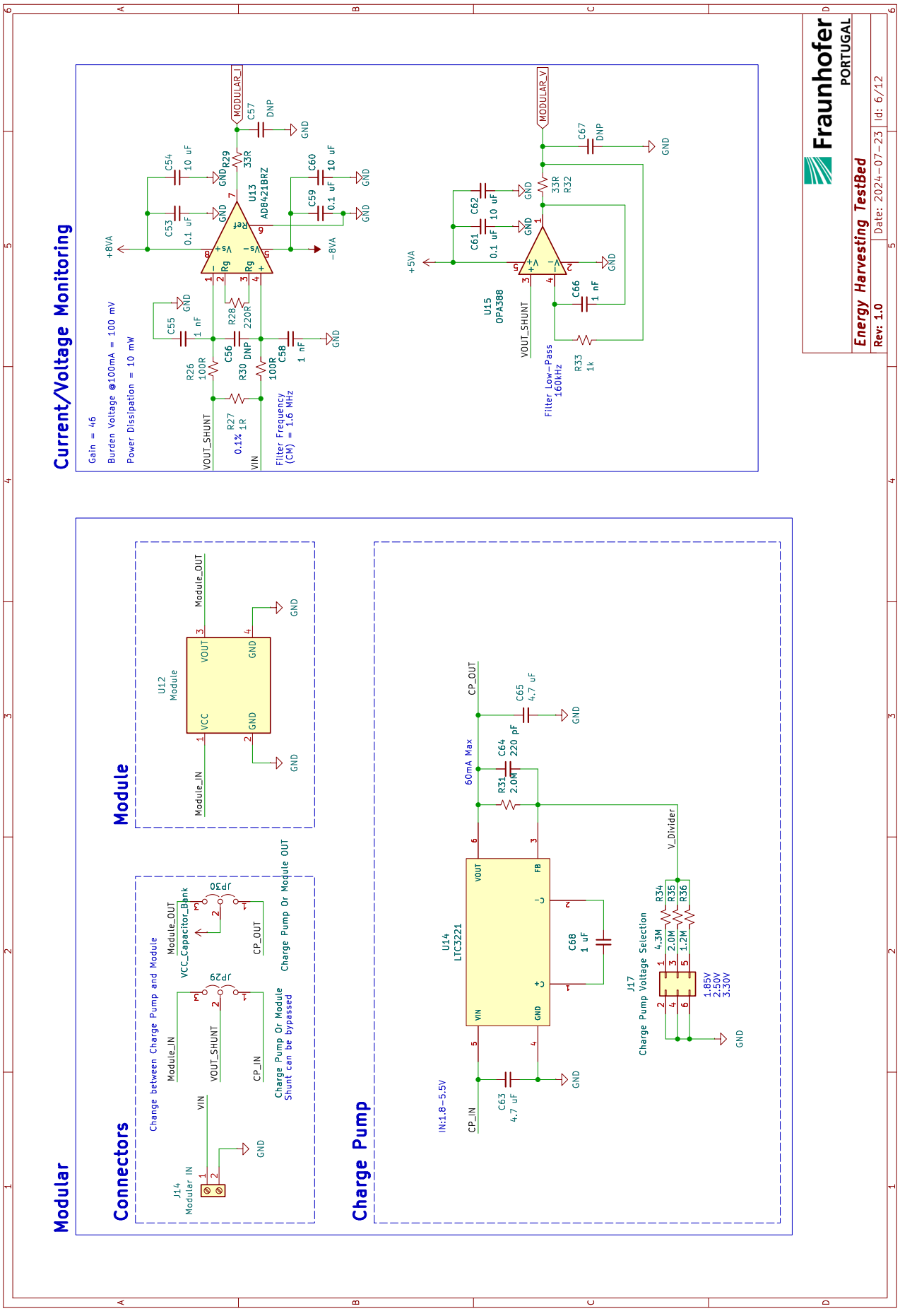
Modular
Current/Voltage Monitoring
Gain = 46
Burden Voltage @100mA = 100 mV
Power Dissipation = 10 mW
+8VA
−8VA
MODULAR_I
MODULAR_V
U13
AD8421BRZ
U15
OPA388
C54 10 uF
C53 0.1 uF
C55 1 nF
C56 DNP
C57 DNP
C58 1 nF
C59 0.1 uF
C60 10 uF
C61 0.1 uF
C62 10 uF
C66 1 nF
C67 DNP
R26 100R
R27 1R 0.1%
R28 220R
R29 33R
R30 100R
R32 33R
R33 1k
VOUT_SHUNT
VIN
Filter Frequency (CM) = 1.6 MHz
+5VA
Filter Low-Pass 160kHz
GND
Fraunhofer PORTUGAL
Energy Harvesting TestBed
Rev: 1.0
Date: 2024-07-23
Id: 6/12
Connectors
Change between Charge Pump and Module
Module_IN
VOUT_SHUNT
CP_IN
VIN
Module_OUT
VCC_Capacitor_Bank
CP_OUT
JP29
JP30
Charge Pump Or Module Shunt can be bypassed
Charge Pump Or Module OUT
J14
Modular IN
Module
U12
Module
VCC
VOUT
GND
Module_IN
Module_OUT
Charge Pump
U14
LTC3221
VIN
VOUT
FB
GND
IN:1.8-5.5V
60mA Max
C63 4.7 uF
C64 220 pF
C65 4.7 uF
C68 1 uF
R31 2.0M
J17
Charge Pump Voltage Selection
R34 4.3M
R35 2.0M
R36 1.2M
V_Divider
1.85V
2.50V
3.30V

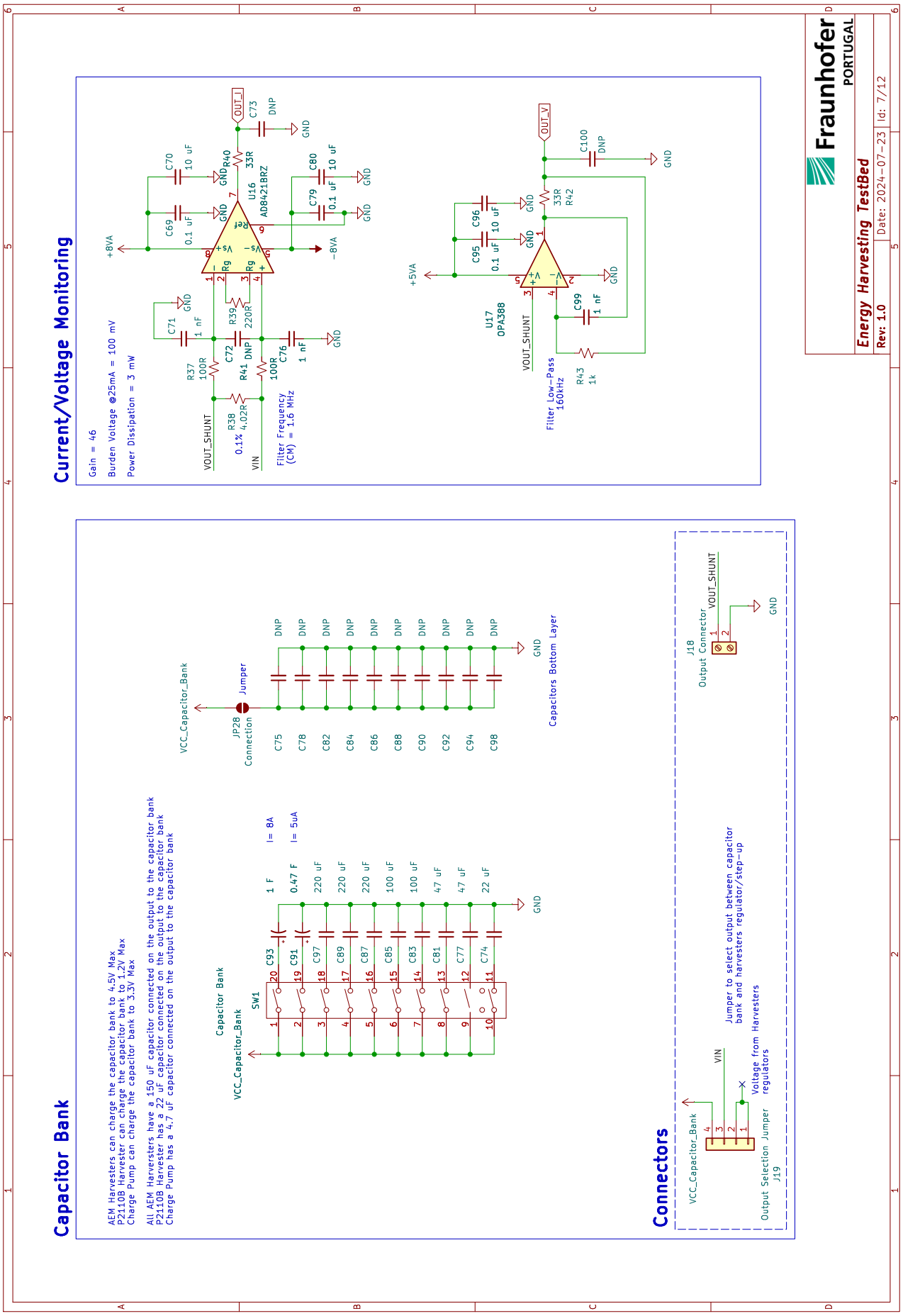
Capacitor Bank
Current/Voltage Monitoring
Connectors
Fraunhofer PORTUGAL
Energy Harvesting TestBed
Rev: 1.0
Date: 2024-07-23
Id: 7/12
AEM Harvesters can charge the capacitor bank to 4.5V Max
P2110B Harvester can charge the capacitor bank to 1.2V Max
Charge Pump can charge the capacitor bank to 3.3V Max
All AEM Harversters have a 150 uF capacitor connected on the output to the capacitor bank
P2110B Harvester has a 22 uF capacitor connected on the output to the capacitor bank
Charge Pump has a 4.7 uF capacitor connected on the output to the capacitor bank
Capacitor Bank
VCC_Capacitor_Bank
SW1
C93 1 F
C91 0.47 F
C97 220 uF
C89 220 uF
C87 220 uF
C85 100 uF
C83 100 uF
C81 47 uF
C77 47 uF
C74 22 uF
I= 8A
I= 5uA
JP28 Jumper Connection
C75 C78 C82 C84 C86 C88 C90 C92 C94 C98 DNP
Capacitors Bottom Layer
Gain = 46
Burden Voltage @25mA = 100 mV
Power Dissipation = 3 mW
+8VA
−8VA
U16 AD8421BRZ
R40 33R
C70 10 uF
C69 0.1 uF
C79 0.1 uF
C80 10 uF
C73 DNP
R37 100R
R38 4.02R 0.1%
R39 220R
R41 100R
C71 1 nF
C72 DNP
C76 1 nF
VOUT_SHUNT
VIN
Filter Frequency (CM) = 1.6 MHz
+5VA
U17 OPA388
C95 0.1 uF
C96 10 uF
C99 1 nF
R42 33R
R43 1k
C100 DNP
Filter Low-Pass 160kHz
VOUT_SHUNT
J18 Output Connector
VCC_Capacitor_Bank
VIN
J19 Output Selection Jumper
Voltage from Harvesters regulators
Jumper to select output between capacitor bank and harvesters regulator/step-up
GND

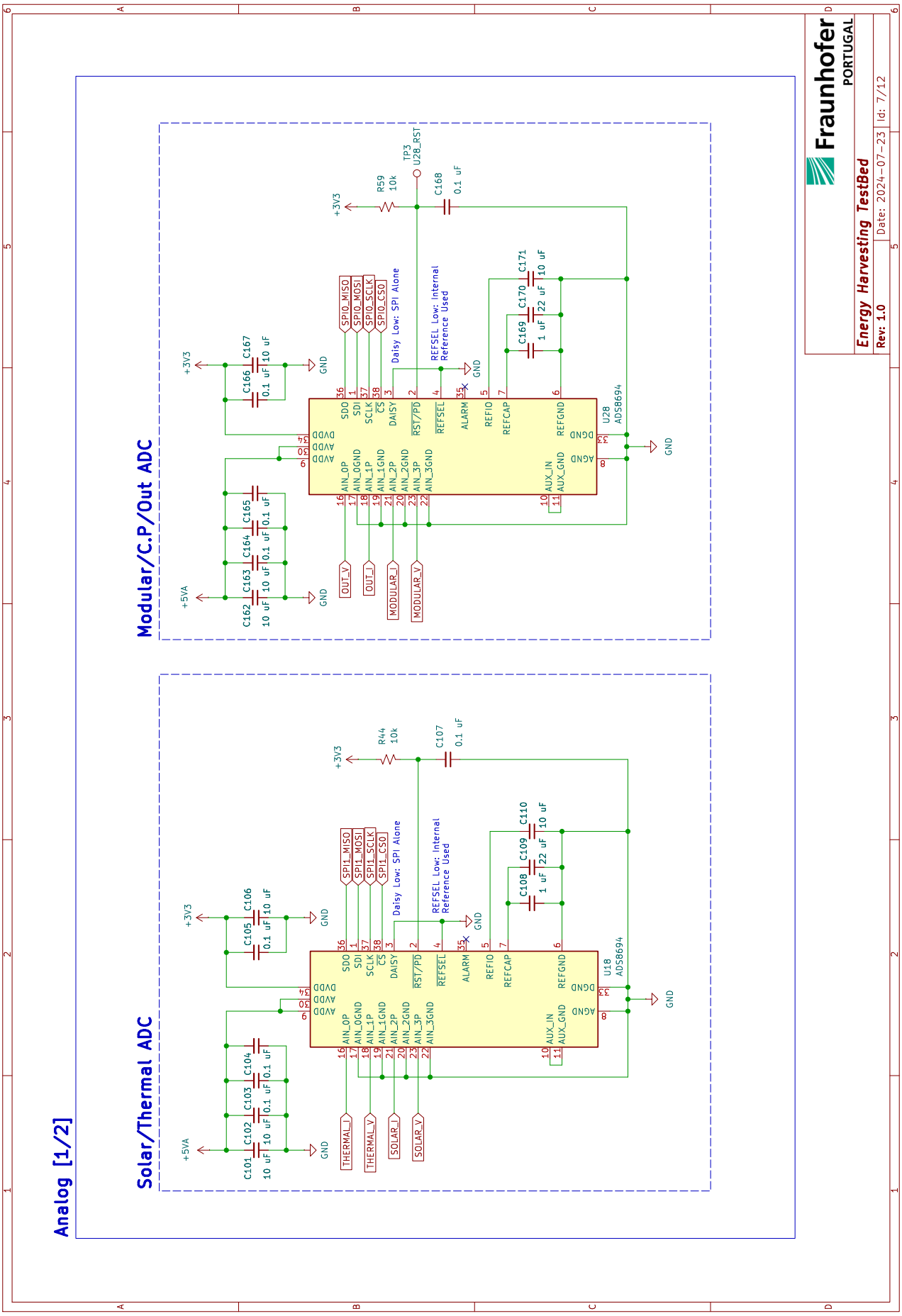
Analog [1/2]
Solar/Thermal ADC
Modular/C.P/Out ADC
Fraunhofer PORTUGAL
Energy Harvesting TestBed
Rev: 1.0
Date: 2024-07-23
Id: 7/12
U18 ADS8694
U28 ADS8694
+3V3
+5VA
GND
R44 10k
R59 10k
TP3 U28_RST
C107 0.1 uF
C168 0.1 uF
C101 10 uF
C102 10 uF
C103 0.1 uF
C104 0.1 uF
C105 0.1 uF
C106 10 uF
C108 1 uF
C109 22 uF
C110 10 uF
C162 10 uF
C163 10 uF
C164 0.1 uF
C165 0.1 uF
C166 0.1 uF
C167 10 uF
C169 1 uF
C170 22 uF
C171 10 uF
SPI1_MISO
SPI1_MOSI
SPI1_SCLK
SPI1_CS0
SPI0_MISO
SPI0_MOSI
SPI0_SCLK
SPI0_CS0
Daisy Low: SPI Alone
REFSEL Low: Internal Reference Used
THERMAL_I
THERMAL_V
SOLAR_I
SOLAR_V
OUT_V
OUT_I
MODULAR_I
MODULAR_V

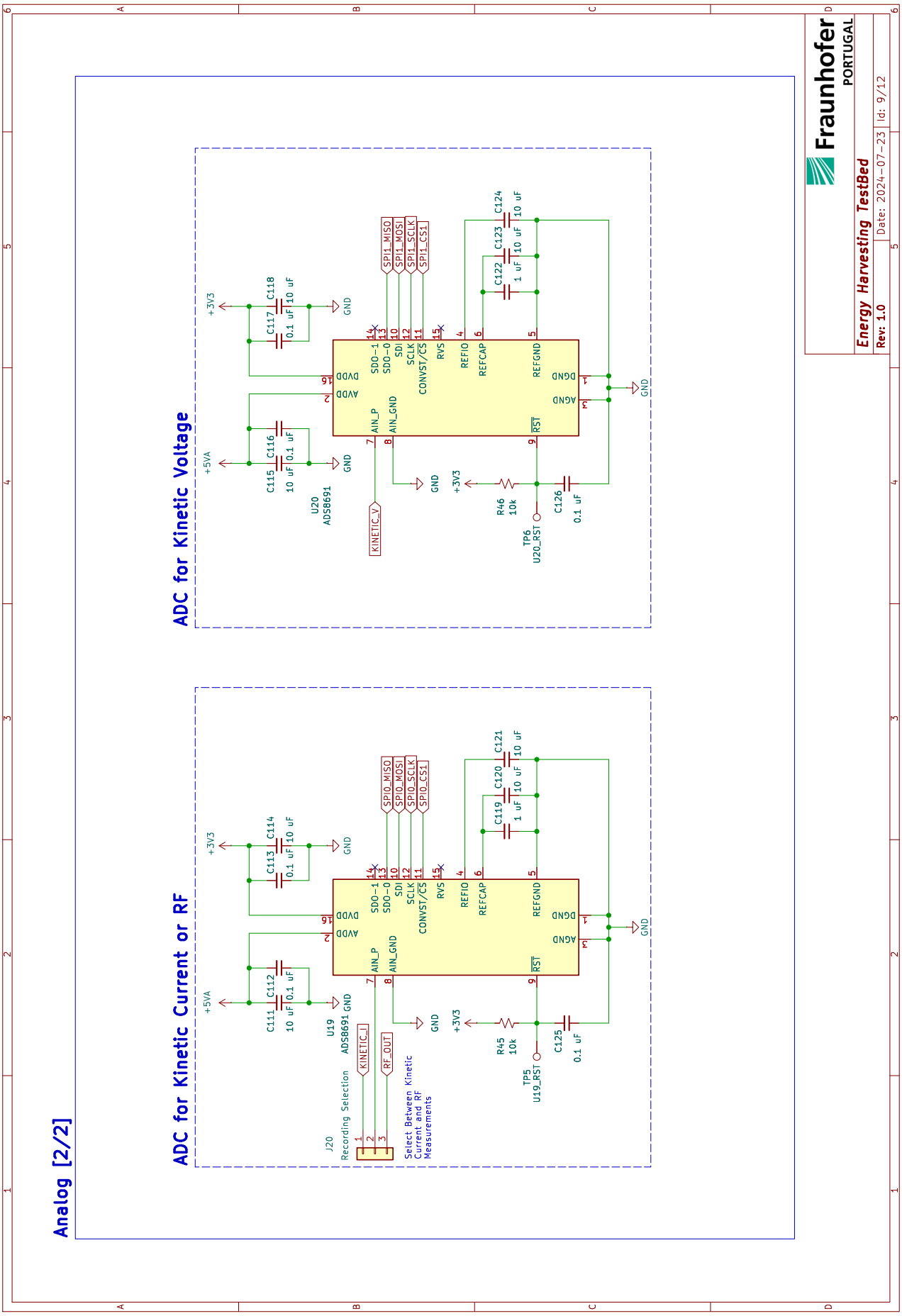
Analog [2/2]
ADC for Kinetic Current or RF
ADC for Kinetic Voltage
Fraunhofer PORTUGAL
Energy Harvesting TestBed
Rev: 1.0
Date: 2024-07-23
Id: 9/12
U19 ADS8691
U20 ADS8691
J20 Recording Selection
Select Between Kinetic Current and RF Measurements
KINETIC_I
RF_OUT
KINETIC_V
SPI0_MISO
SPI0_MOSI
SPI0_SCLK
SPI0_CS1
SPI1_MISO
SPI1_MOSI
SPI1_SCLK
SPI1_CS1
U19_RST
U20_RST
+3V3
+5VA
GND

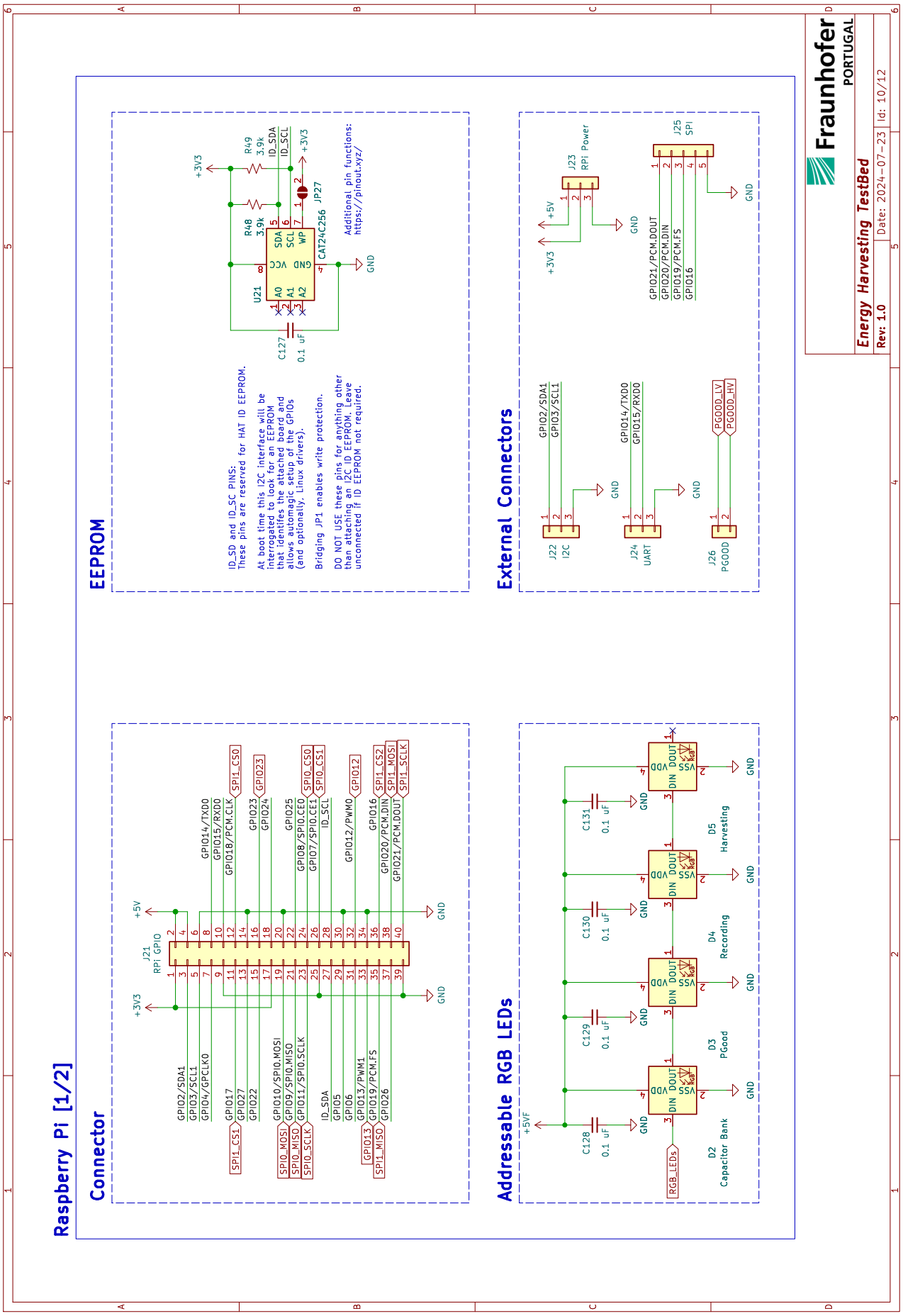
Raspberry Pi [1/2]
Connector
EEPROM
External Connectors
Addressable RGB LEDs
Fraunhofer PORTUGAL
Energy Harvesting TestBed
Rev: 1.0
Date: 2024-07-23
Id: 10/12

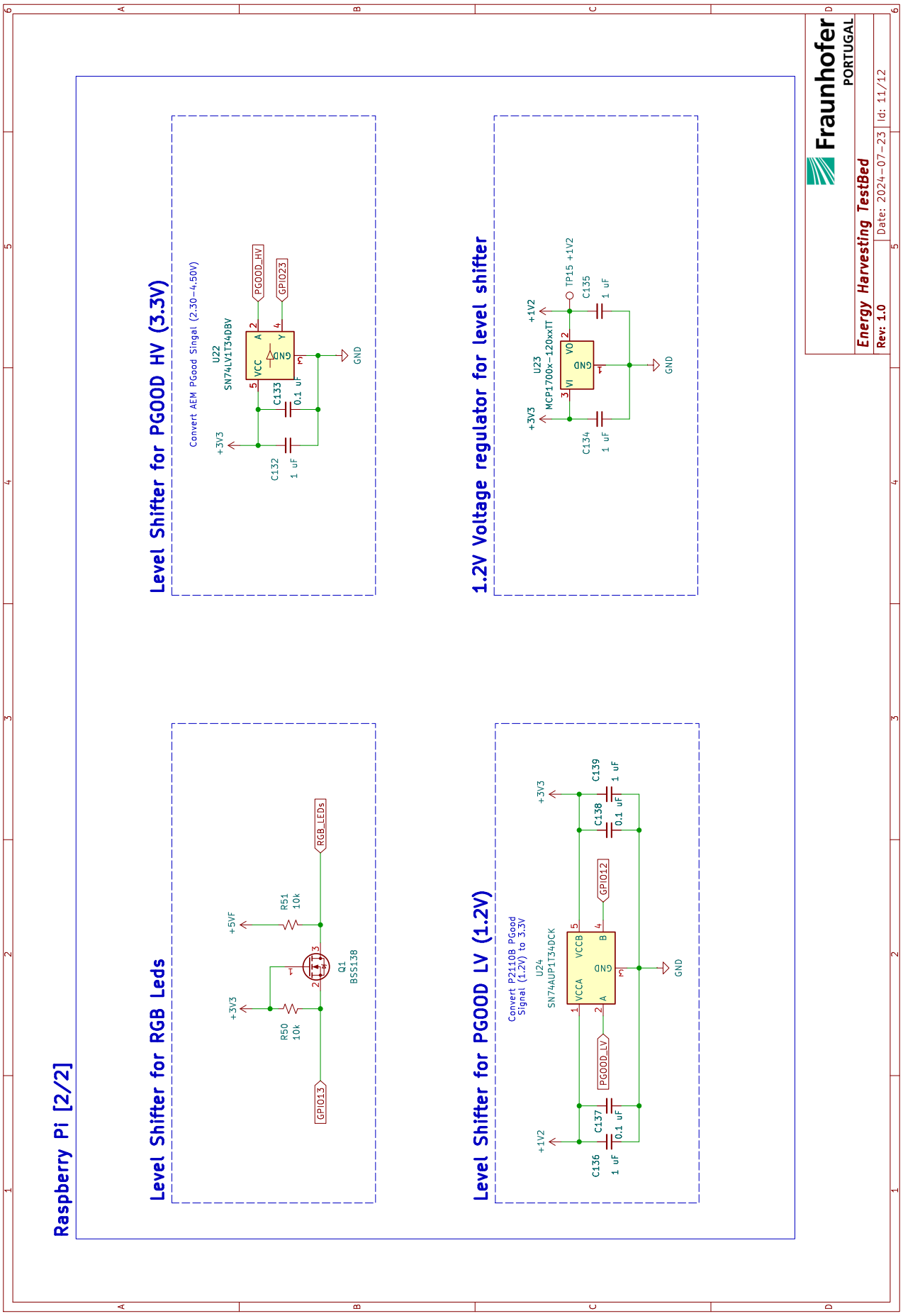
Raspberry Pi [2/2]
Level Shifter for PGOOD HV (3.3V)
Convert AEM PGood Singal (2.30-4.50V)
U22
SN74LV1T34DBV
PGOOD_HV
GPIO23
VCC
GND
C133
0.1 uF
C132
1 uF
+3V3
GND
1.2V Voltage regulator for level shifter
U23
MCP1700x-120xxTT
TP15 +1V2
C135
1 uF
C134
1 uF
+1V2
+3V3
GND
Level Shifter for RGB Leds
RGB_LEDs
R51
10k
R50
10k
Q1
BSS138
+5VF
+3V3
GPIO13
Level Shifter for PGOOD LV (1.2V)
Convert P2110B PGood
Signal (1.2V) to 3.3V
U24
SN74AUP1T34DCK
VCCA
VCCB
GND
GPIO12
PGOOD_LV
C136
1 uF
C137
0.1 uF
C138
0.1 uF
C139
1 uF
+1V2
+3V3
GND
Fraunhofer
PORTUGAL
Energy Harvesting TestBed
Rev: 1.0
Date: 2024-07-23
Id: 11/12

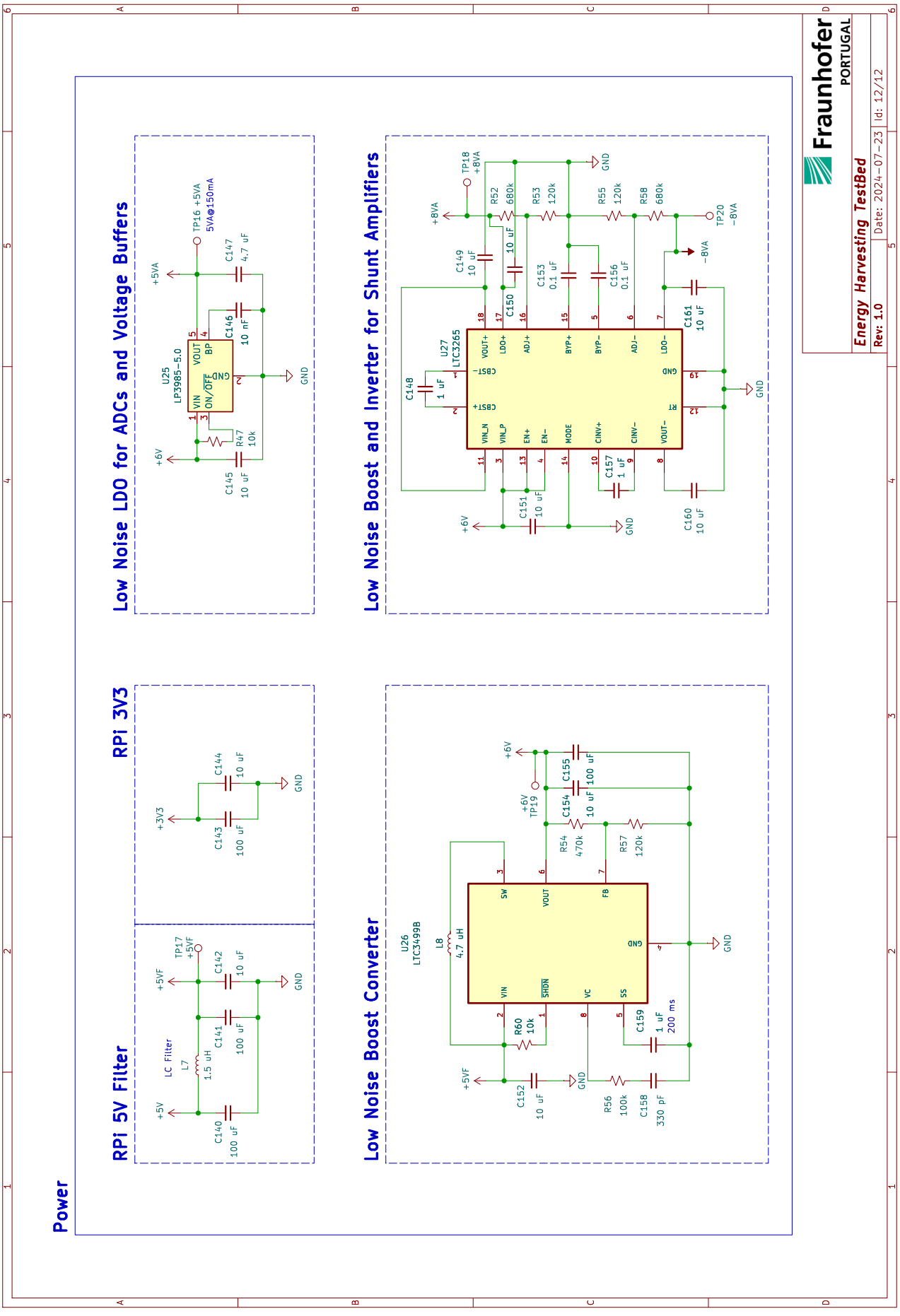
Power
Low Noise LDO for ADCs and Voltage Buffers
Low Noise Boost and Inverter for Shunt Amplifiers
RPi 3V3
RPi 5V Filter
Low Noise Boost Converter
Fraunhofer PORTUGAL
Energy Harvesting TestBed
Rev: 1.0
Date: 2024-07-23
Id: 12/12

Appendix B

Step-by-Step Current Profiling of the Riotee Platform

Source's tension and current values chosen to simulate being powered through the solar panel LL200-2.4-75 (based on the datasheet)	Step1(basic BLE, temp sensor)			Step1.1(step1+wait_cap_charged)			Step2 (BLE config and sensor read)			Step3(temp change detection)			Step4 (checkpoint + thresholds)		
	1.6V e 0.0004A			1.6V e 0.0003A			1.6V e 0.0003A			1.6V e 0.0003A			1.6V e 0.0003A		
	Average(uA)	**Max(mA)**	**Time(ms)**	**Average(uA)**	**Max(mA)**	**Time(ms)**	**Average(uA)**	**Max(mA)**	**Time(ms)**	**Average(uA)**	**Max(mA)**	**Time(ms)**	**Average(uA)**	**Max(mA)**	**Time(ms)**
	156,64	162,49	516,5	127,04	121,9	514,1	129,92	124,19	514,6	146,63	173,25	515,4	65,02	271,75	1519
	4120	80,06	14,89	3940	141,01	14,82	3820	117,32	15,39	4130	119,61	16,19	48,76	118,85	1015
	4150	128,01	14,89	3820	111,22	14,81	3770	105,13	15,46	4130	118,08	16,27	76,37	154,04	1018
	4130	102,84	14,69	3920	158,65	14,88	3730	96	15,4	4260	145,61	16,26	48,62	113,51	1015
	4110	75,51	14,8	3940	142,54	14,79	3900	162,49	15,42	4250	134,89	16,2	77,2	139,48	1018
	4280	129,54	17,1	3960	150,79	14,77	3950	164,02	15,45	4160	105,13	16,1	47,82	109,7	1015
	3950	106,65	15,56	4060	201,02	14,98	3750	99,04	15,36	4220	173,25	16,34	49,18	147,91	1015
	3920	80,82	15,72	3930	180,18	15,13	3720	94,48	15,46	4150	106,65	16,14	49,54	174,02	1015
	4170	131,83	14,83	3910	135,65	14,85	3960	154,04	15,3	4210	130,3	16,15	47,29	100,56	1015
	4120	108,17	14,82	3940	158,65	14,9	3920	158,65	15,39	4230	131,83	16,18	49,91	173,25	1016
Average	3710,664	110,592	65,38	3554,704	150,161	64,803	3464,992	127,536	65,323	3788,663	133,86	66,123	55,971	150,307	1066,1
Average without first measurement	4105,55556	104,826	15,2556	3935,55556	153,301	14,8811	3835,55556	127,908	15,4033	4193,33333	129,483	16,2033	54,9655556	136,813	1015,78
Average sleep	0,38 uA ou 0,37uA														

Figure B.1: Step-by-step current consumption of the Riotee platform, measured under supply conditions simulating the LL200-2.4-75 indoor solar panel (1.6 V, 0.3–0.4 mA). Each firmware operation step (BLE init, capacitor charge wait, sensor read, temperature detection, and checkpoint/flash write) is profiled with average, peak, and duration values.

Appendix C

Current Profiling of the IN100 Platform

	Test1-Board 2			Test2-Board 2			Test3-Board			Test4-Board		
	2V e 400KHz			1.8V e 400KHz			2V e 100KHz			1.8V e 100KHz		
	Average(mA)	**Max(mA)**	**Time(ms)**	**Average(mA)**	**Max(mA)**	**Time(ms)**	**Average(mA)**	**Max(mA)**	**Time(ms)**	**Average(mA)**	**Max(mA)**	**Time(ms)**
	0,36469	15,41	88,41	0,36619	60,72	89,34	0,40533	50,42	89,27	0,41717	322,77	91,32
	1,32	28,7	15,68	1,26	18,64	15,77	1,3	12,2	16,52	1,57	303,89	16,52
	1,35	35,82	15,68	1,68	413,97	15,75	1,32	15,15	16,5	1,29	17,06	16,54
	1,32	20,17	15,69	1,22	11,7	15,75	1,59	288,18	16,52	1,25	11,36	16,51
	1,28	11,96	15,7	1,66	405,19	15,76	1,33	19,69	16,5	1,6	334,59	16,52
	1,29	13,97	15,69	1,22	10,18	15,75	1,29	10,96	16,5	1,65	373,37	16,53
	1,37	50,93	15,7	1,27	17,05	15,76	1,33	19	16,5	1,26	10,52	16,52
	1,31	19,55	15,7	1,22	10,64	15,75	1,29	11,69	16,53	1,25	11,53	16,52
	1,36	42,38	15,69	1,22	11,26	15,75	1,59	294,45	16,51	1,25	10,95	16,56
	1,36	43,2	15,7	1,26	16,25	15,76	1,33	16,27	16,51	1,6	325,92	16,53
	1,34	38,43	15,69	1,22	11,63	15,76	1,67	363,04	16,51	1,28	16,04	16,53
Average	1,24224455	29,1382	22,30273	1,23601727	89,7482	22,44545	1,31321182	100,095	23,12455	1,31065182	158	23,32727
Average without first measurement	1,33	30,511	15,692	1,323	92,651	15,756	1,404	105,063	16,51	1,4	141,523	16,528

Figure C.1: Cycle-level current consumption of the IN100 platform under different supply voltages (1.8–2.0 V) and clock frequencies (100 kHz and 400 kHz). Results are averaged over multiple cycles (excluding the first measurement due to timer initialization) and include mean current, peak excursions, and active time. The results highlight that while average current remains relatively stable around 1.2–1.4 mA, peak currents vary significantly depending on configuration, with the 1.8 V/400 kHz case showing occasional spikes above 400 mA.

Appendix D

Antenna Simulation Figures

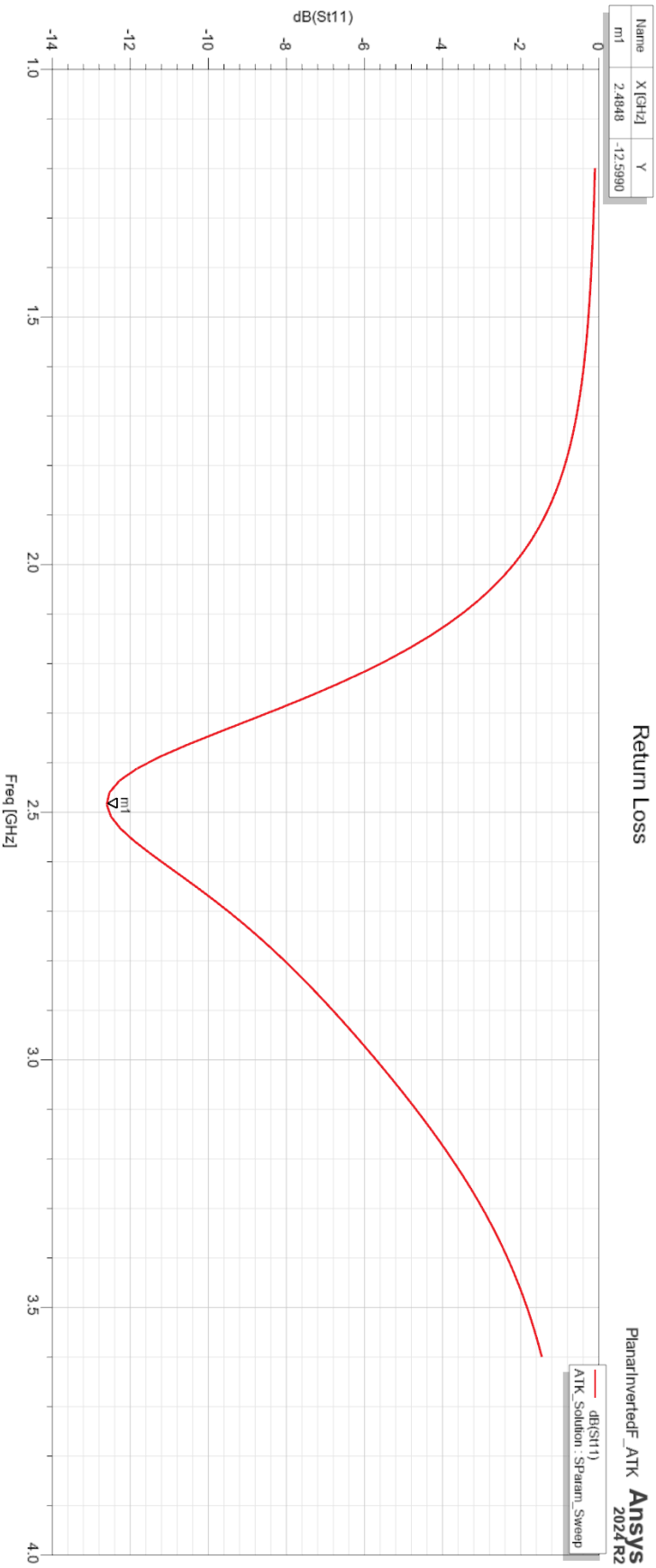

Figure D.1: Simulated return loss (S11) showing resonance near 2.48 GHz.

Name	Freq [GHz]	Ang	Mag	RX
m1	2.4848	-7.4106	0.2344	1.6018 - 0.1025i

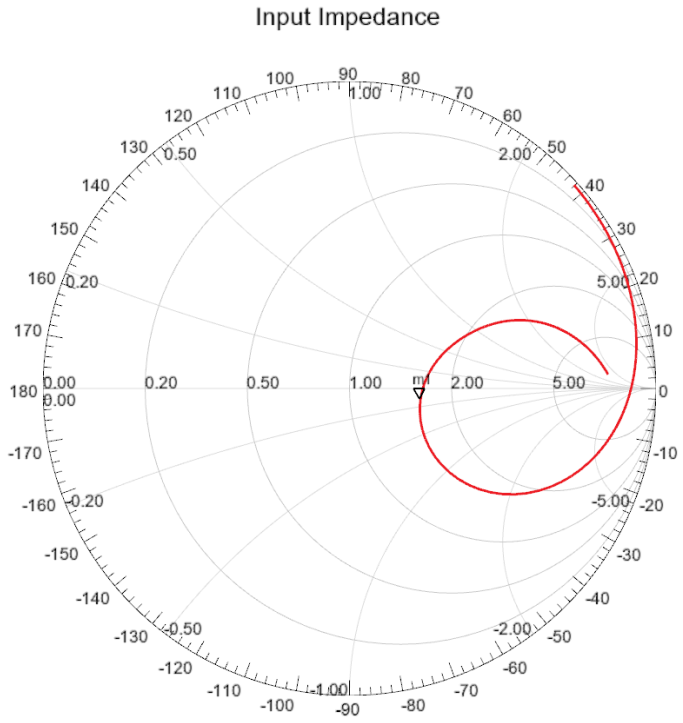

Figure D.2: Smith Chart of simulated input impedance showing impedance approaching 50 Ω at resonance.

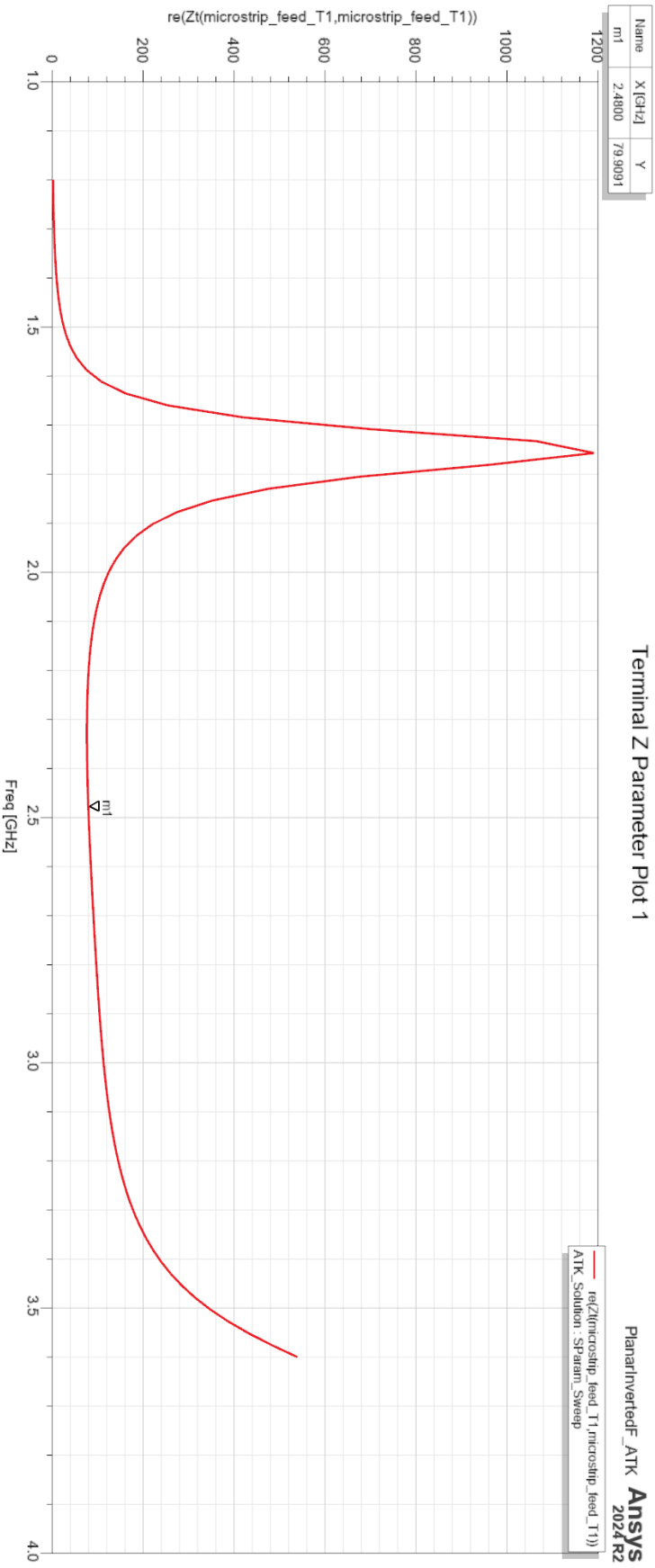

Figure D.3: Real part of the terminal Z-parameter across frequency.

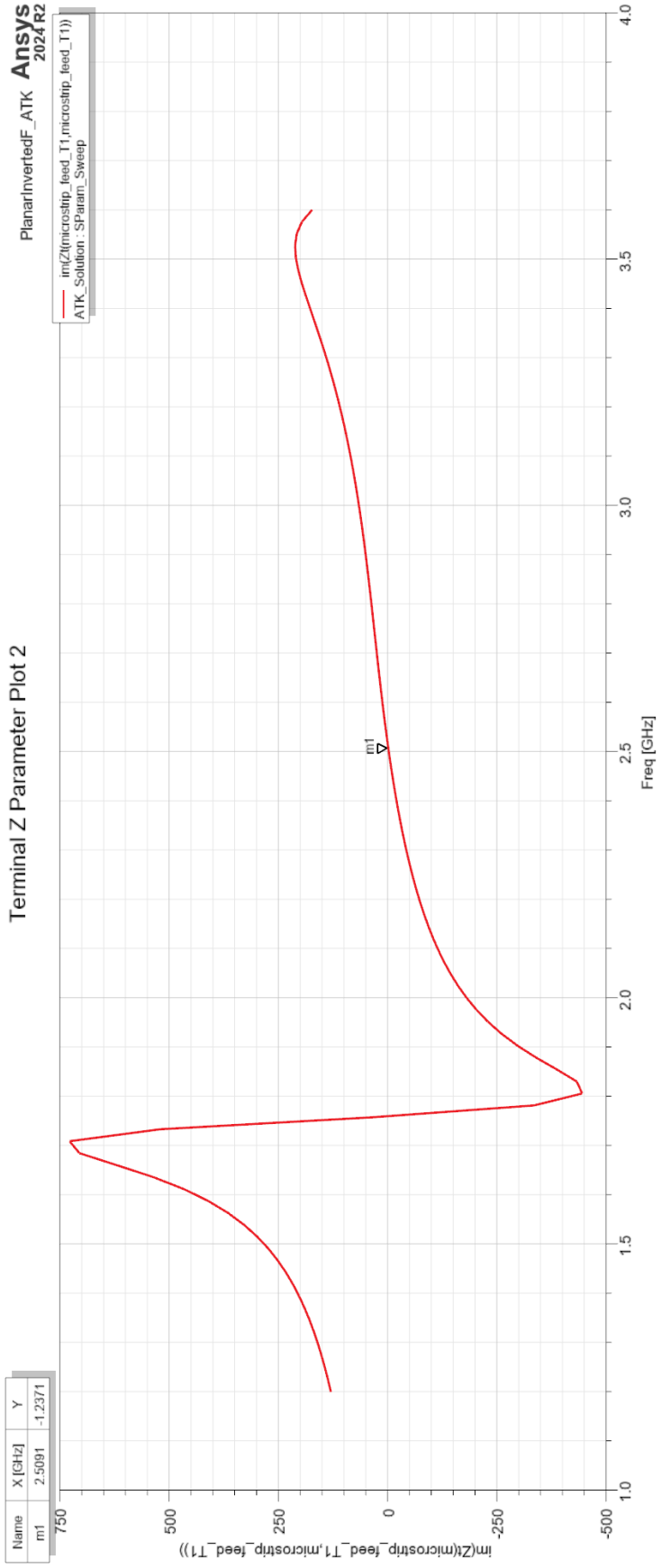

Figure D.4: Imaginary part of the terminal Z-parameter across frequency.

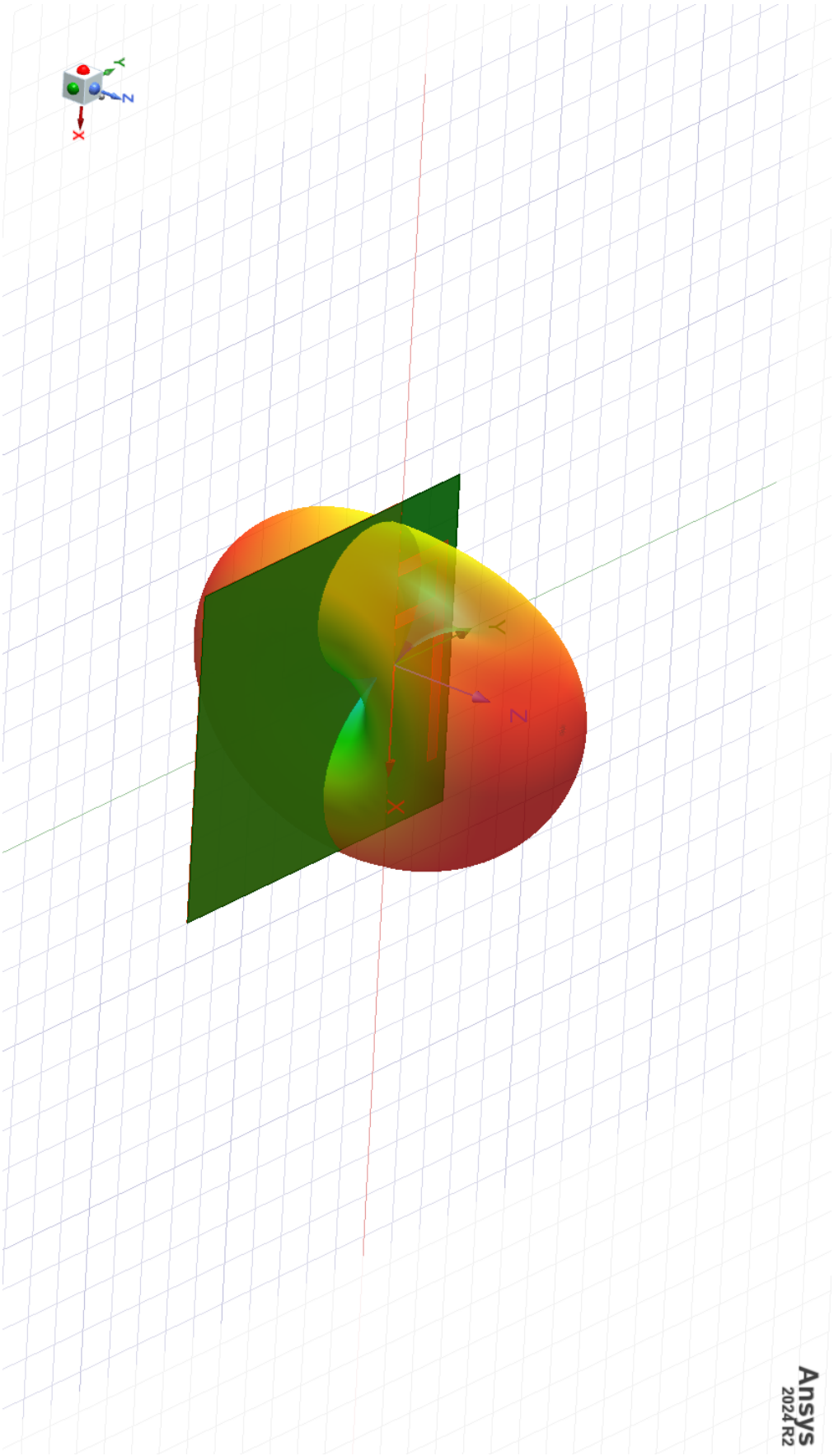

Figure D.5: Simulated 3D antenna gain pattern.

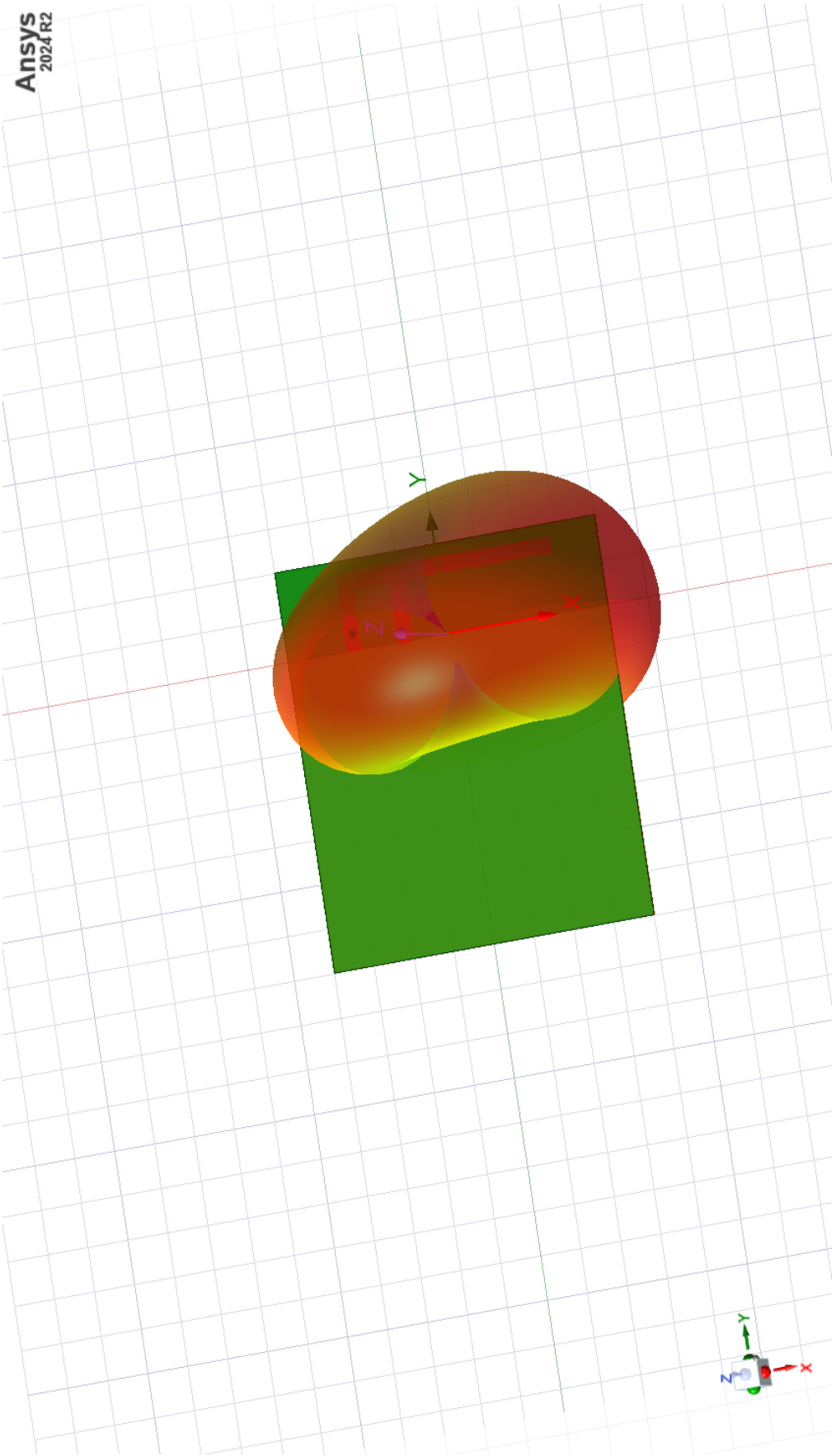

Figure D.6: Alternate 3D antenna gain view showing secondary lobes.

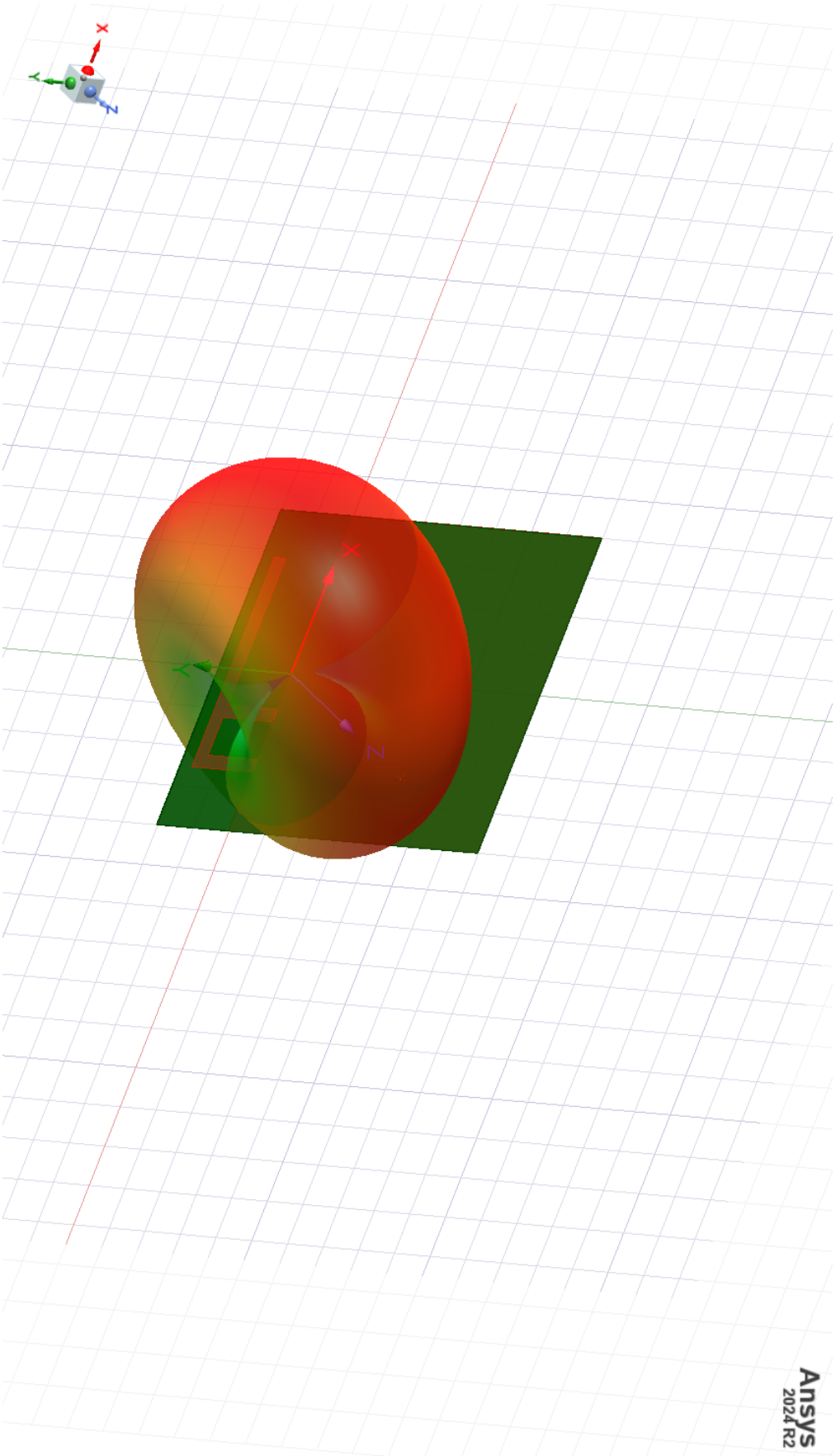

Figure D.7: Alternate 3D antenna gain perspective highlighting directional lobes.

Appendix E

Node Schematic

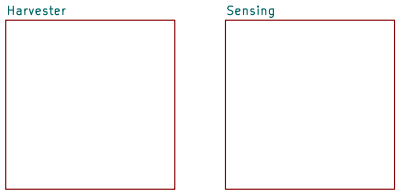

Verificar como podemos carregar os supercondensadores rapidamente.
Conector exposto ou uma porta dummy USB-C

Criar um nome para o dispositivo

Possíveis nomes:
Aethra
Helion
Caelus
Photina

Fraunhofer PORTUGAL

Batteryless Device		
Rev: 1.0	Date:	Id: 1/3

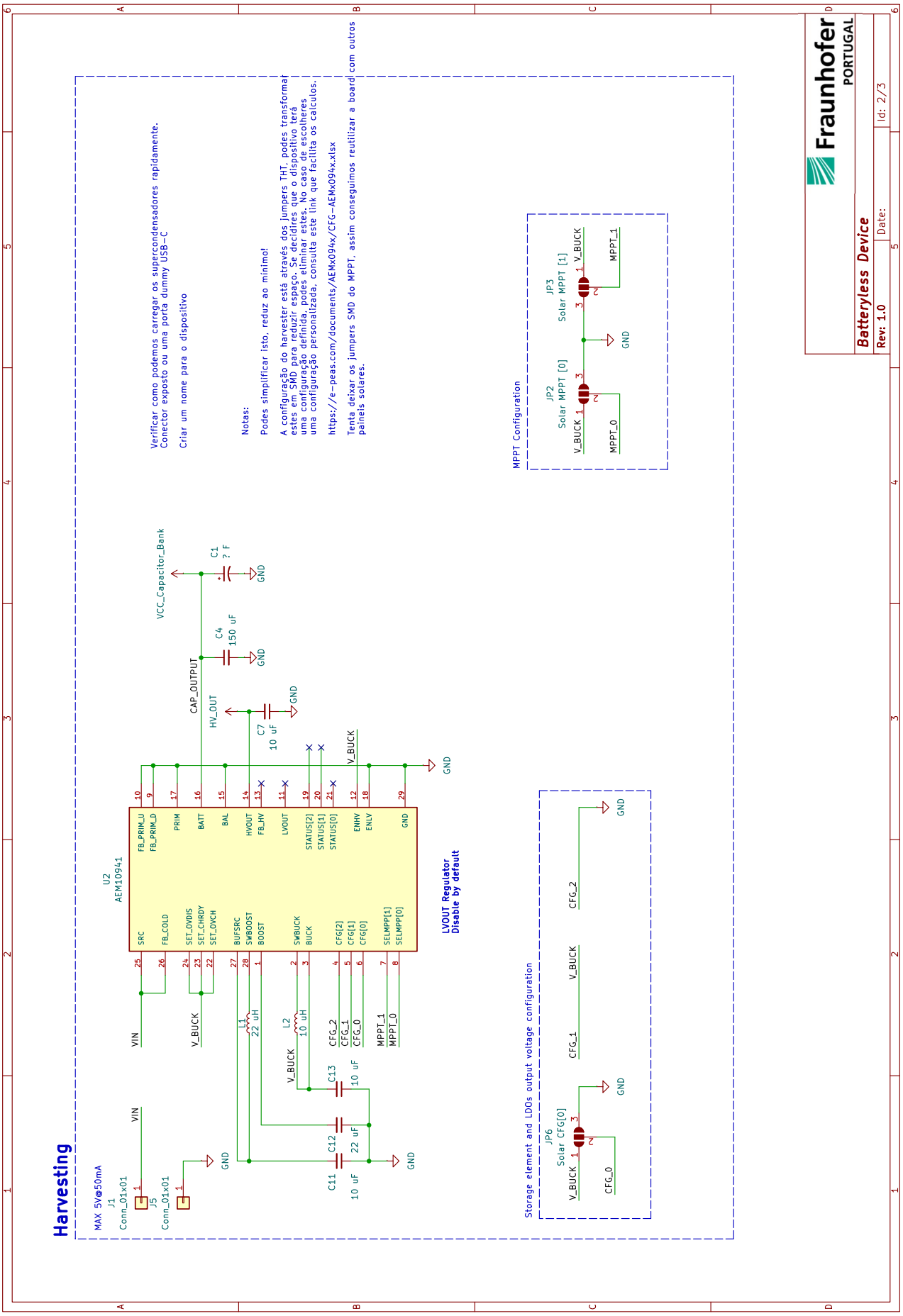
Harvesting
MAX 5V@50mA
J1
Conn_01x01
J5
Conn_01x01
VIN
GND
U2
AEM10941
SRC
FB_COLD
FB_PRIM_U
FB_PRIM_D
PRIM
BATT
BAL
HVOUT
FB_HV
LVOUT
STATUS[2]
STATUS[1]
STATUS[0]
ENHV
ENLV
GND
SET_OVDIS
SET_CHRDY
SET_OVCH
BUFSRC
SWBOOST
BOOST
SWBUCK
BUCK
CFG[2]
CFG[1]
CFG[0]
SELMPP[1]
SELMPP[0]
V_BUCK
L1
22 uH
L2
10 uH
C11
10 uF
C12
22 uF
C13
10 uF
CFG_2
CFG_1
CFG_0
MPPT_1
MPPT_0
CAP_OUTPUT
HV_OUT
C7
10 uF
C4
150 uF
C1
? F
VCC_Capacitor_Bank
LVOUT Regulator
Disable by default
Storage element and LDOs output voltage configuration
JP6
Solar CFG[0]
MPPT Configuration
JP2
Solar MPPT [0]
JP3
Solar MPPT [1]
Verificar como podemos carregar os supercondensadores rapidamente.
Conector exposto ou uma porta dummy USB-C
Criar um nome para o dispositivo
Notas:
Podes simplificar isto, reduz ao mínimo!
A configuração do harvester está através dos jumpers THT, podes transformar estes em SMD para reduzir espaço. Se decidires que o dispositivo terá uma configuração definida, podes eliminar estes. No caso de escolheres uma configuração personalizada, consulta este link que facilita os calculos.
https://e-peas.com/documents/AEMx094x/CFG-AEMx094x.xlsx
Tenta deixar os jumpers SMD do MPPT, assim conseguimos reutilizar a board com outros painéis solares.
Fraunhofer
PORTUGAL
Batteryless Device
Rev: 1.0
Date:
Id: 2/3

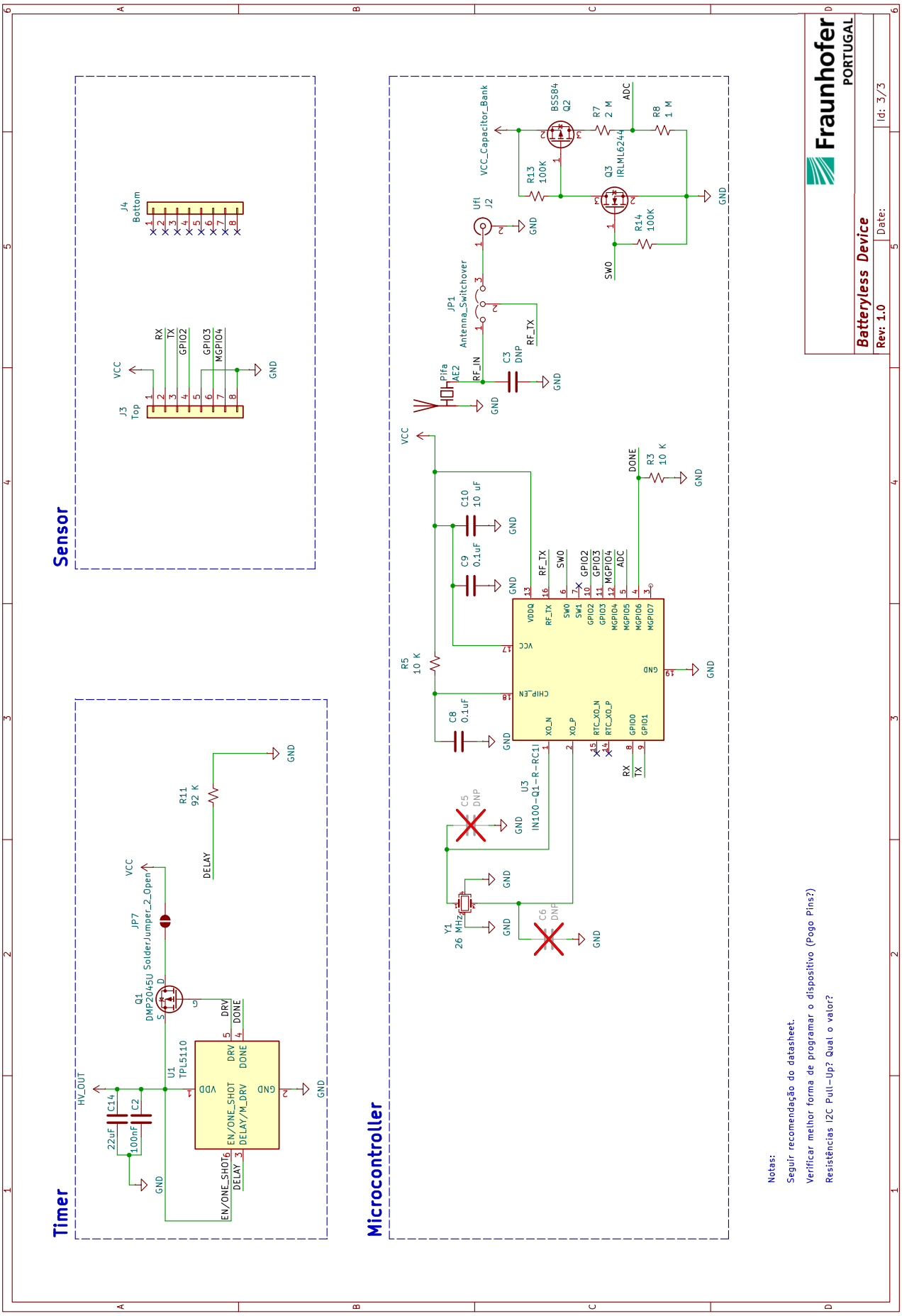
Sensor
Timer
Microcontroller
Fraunhofer PORTUGAL
Batteryless Device
Rev: 1.0
Date:
Id: 3/3
Notas:
Seguir recomendação do datasheet.
Verificar melhor forma de programar o dispositivo (Pogo Pins?)
Resistências I2C Pull-Up? Qual o valor?

Appendix F

Sensor Module Schematic

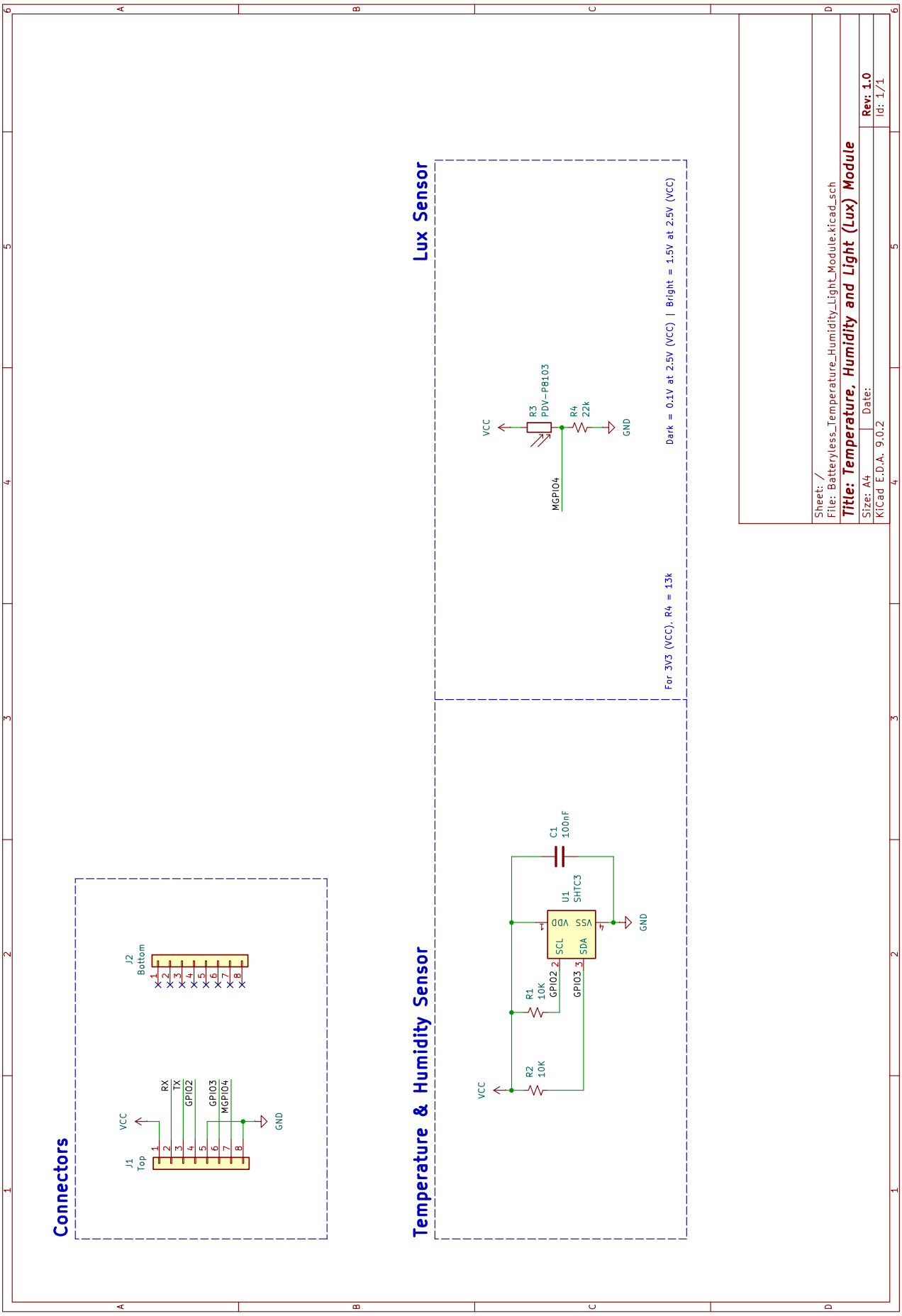
Connectors
J1
Top
VCC
RX
TX
GPIO2
GPIO3
MGPIO4
GND
J2
Bottom
Temperature & Humidity Sensor
U1
SHTC3
VDD
SCL
SDA
VSS
C1
100nF
R1
10K
R2
10K
GPIO2
GPIO3
VCC
GND
Lux Sensor
R3
PDV-P8103
R4
22k
MGPIO4
VCC
GND
Dark = 0.1V at 2.5V (VCC) | Bright = 1.5V at 2.5V (VCC)
For 3V3 (VCC), R4 = 13k
Sheet: /
File: Batteryless_Temperature_Humidity_Light_Module.kicad_sch
Title: Temperature, Humidity and Light (Lux) Module
Size: A4
Date:
Rev: 1.0
KiCad E.D.A. 9.0.2
Id: 1/1

Appendix G

RSSI Heatmap Tables

Batteryless Node with external antenna (Shunt connection with 0 ohm jumper resistor)

Advertising Random Delay	0~10ms																				
Location	Open Space (Left wall if facing rooms)			Open Space (center wall)			Open Space (corridor behind centre wall)			Room 1.11 (8m distance)			Room 1.09 (7m distance)			Room 1.12 (10m distance)			Room 1.14 (14m distance)		
TX Power (dBm)	-1	2	4	-1	2	4	-1	2	4	-1	2	4	-1	2	4	-1	2	4	-1	2	4
RSSI	-60	-65	-63	-69	-60	-55	-68	-73	-64	-73	-67	-54	-66	-53	-60	-62	-57	-57	-67	-63	-61
	-67	-64	-61	-66	-59	-52	-76	-63	-80	-66	-60	-61	-58	-71	-53	-66	-62	-62	-65	-64	-62
	-70	-60	-62	-52	-52	-65	-72	-71	-71	-69	-64	-64	-79	-59	-67	-67	-62	-55	-67	-64	-62
	-61	-62	-63	-59	-59	-56	-79	-75	-64	-65	-70	-52	-66	-69	-62	-61	-57	-59	-66	-61	-61
	-62	-66	-62	-62	-60	-52	-75	-65	-79	-63	-62	-57	-60	-61	-53	-66	-62	-64	-68	-62	-62
	-65	-59	-65	-58	-52	-60	-72	-68	-68	-72	-65	-52	-63	-54	-62	-66	-64	-60	-67	-64	-62
	-69	-62	-63	-62	-50	-50	-81	-66	-79	-65	-60	-55	-79	-80	-59	-60	-57	-65	-67	-62	-62
	-63	-73	-62	-56	-64	-68	-70	-79	-69	-64	-60	-66	-62	-69	-66	-66	-62	-56	-67	-62	-64
	-66	-64	-60	-58	-59	-58	-74	-69	-64	-68	-55	-52	-60	-55	-59	-67	-64	-60	-66	-60	-62
	-65	-72	-64	-62	-52	-51	-71	-64	-77	-65	-64	-58	-76	-81	-61	-60	-58	-65	-68	-63	-62
	-70	-60	-59	-57	-64	-54	-77	-78	-69	-69	-65	-65	-61	-55	-58	-68	-64	-53	-65	-63	-62
	-63	-63	-63	-62	-59	-51	-72	-74	-63	-66	-54	-54	-67	-53	-56	-65	-57	-60	-69	-61	-60
	-65	-59	-69	-57	-58	-55	-76	-64	-67	-65	-58	-58	-58	-66	-71	-58	-63	-65	-68	-63	-61
	-67	-62	-61	-59	-51	-52	-79	-69	-64	-68	-66	-54	-73	-53	-58	-66	-57	-55	-67	-62	-61
	-66	-74	-63	-64	-68	-64	-80	-63	-69	-65	-55	-59	-68	-75	-65	-59	-62	-59	-68	-64	-62
	-69	-61	-62	-57	-51	-53	-69	-73	-64	-71	-58	-65	-59	-62	-72	-64	-64	-63	-67	-62	-63
	-63	-62	-61	-64	-68	-51	-75	-63	-69	-65	-60	-52	-68	-54	-58	-67	-57	-61	-66	-61	-62
	-64	-62	-66	-56	-51	-65	-72	-76	-64	-66	-54	-57	-59	-53	-63	-66	-61	-63	-68	-63	-61
	-68	-61	-62	-60	-69	-52	-77	-63	-69	-64	-58	-65	-77	-74	-68	-66	-57	-54	-67	-62	-62
	-67	-61	-64	-64	-59	-52	-78	-61	-63	-65	-67	-57	-68	-60	-58	-59	-62	-61	-66	-62	-63
Average (%)	-66	-64	-63	-60	-58	-56	-75	-69	-69	-67	-61	-58	-66	-63	-61	-64	-60	-60	-67	-62	-62

Figure G.1: RSSI values for the Luxor node using an external antenna across different locations and transmission powers.

Batteryless Node with internal antenna (capacitor 2.2pF)

Advertising Random Delay	0~10ms																				
Location	Open Space (Left wall facing rooms)			Open Space (center wall)			Open Space (corridor behind centre wall)			Room 1.11 (8m distance)			Room 1.09 (7m distance)			Room 1.12 (10m distance)			Room 1.14 (14m distance)		
TX Power (dBm)	-1	2	4	-1	2	4	-1	2	4	-1	2	4	-1	2	4	-1	2	4	-1	2	4
	-69	-64	-61	-65	-63	-51	-78	-78	-76	-67	-70	-62	-72	-61	-65	-75	-68	-64	-73	-71	-66
	-69	-65	-62	-67	-63	-60	-76	-78	-74	-67	-70	-62	-70	-63	-67	-74	-68	-64	-75	-70	-67
	-70	-64	-61	-67	-63	-59	-77	-74	-74	-73	-63	-63	-66	-60	-59	-77	-66	-65	-76	-68	-68
	-66	-62	-60	-62	-58	-62	-75	-74	-73	-71	-64	-64	-71	-69	-59	-78	-66	-68	-71	-71	-68
	-67	-61	-60	-63	-57	-61	-77	-76	-70	-68	-66	-63	-72	-68	-60	-69	-67	-68	-71	-70	-67
	-67	-62	-59	-63	-56	-61	-76	-74	-71	-73	-66	-63	-71	-66	-58	-76	-67	-68	-71	-66	-69
	-67	-61	-62	-62	-56	-55	-75	-76	-73	-73	-62	-63	-73	-62	-58	-75	-66	-68	-71	-71	-67
	-69	-63	-62	-62	-55	-56	-75	-73	-72	-76	-65	-66	-76	-62	-58	-75	-69	-66	-72	-66	-68
	-70	-63	-61	-61	-61	-57	-80	-77	-73	-73	-64	-68	-73	-62	-58	-69	-69	-69	-72	-66	-66
RSSI	-69	-63	-60	-62	-61	-53	-83	-88	-74	-73	-66	-74	-72	-61	-64	-68	-69	-67	-73	-66	-68
	-67	-63	-63	-66	-61	-54	-81	-84	-73	-71	-70	-62	-70	-61	-63	-70	-67	-64	-69	-72	-67
	-68	-64	-63	-66	-59	-53	-80	-71	-77	-69	-71	-63	-69	-61	-60	-68	-68	-63	-72	-70	-69
	-68	-64	-61	-65	-58	-61	-76	-69	-80	-68	-71	-66	-65	-61	-58	-68	-70	-65	-74	-72	-68
	-70	-65	-62	-62	-59	-62	-76	-69	-80	-66	-65	-63	-68	-63	-59	-75	-68	-64	-71	-69	-67
	-68	-61	-60	-62	-55	-61	-79	-71	-69	-67	-66	-63	-65	-67	-59	-75	-70	-67	-74	-70	-68
	-67	-61	-60	-63	-56	-57	-77	-72	-69	-71	-65	-64	-66	-66	-59	-76	-67	-66	-70	-70	-68
	-66	-61	-60	-63	-56	-56	-81	-73	-69	-72	-65	-72	-68	-67	-64	-76	-67	-68	-71	-69	-67
	-66	-63	-61	-65	-65	-56	-78	-75	-70	-71	-65	-70	-66	-61	-66	-73	-66	-66	-72	-67	-69
	-70	-63	-64	-63	-63	-55	-78	-75	-70	-71	-64	-70	-69	-61	-64	-69	-68	-78	-73	-68	-65
	-70	-63	-64	-66	-66	-53	-75	-87	-71	-71	-64	-61	-69	-62	-65	-70	-67	-68	-69	-67	-65
Average (%)	-68	-63	-61	-64	-60	-57	-78	-76	-73	-71	-66	-65	-70	-63	-61	-73	-68	-67	-72	-69	-67

Figure G.2: RSSI values for the Luxor node using an internal antenna across different locations and transmission powers.

References

[1] Abracon LLC. *ADCM-S06R0S Series-Connected Supercapacitor Module Datasheet*. https://pt.mouser.com/datasheet/2/3/ADCM_S06R0S-3318057.pdf. Accessed: 2025-08-08. 2024.

[2] M. Afanasov et al. "Battery-less zero-maintenance embedded sensing at the Mithræum of Circus Maximus". In: *Proceedings of the 18th ACM Conference on Embedded Networked Sensor Systems* (2020), pp. 1–14. DOI: 10.1145/3384419.3430755.

[3] Ambient IoT Consortium. *Ambient IoT*. Accessed: 2025-08-21. 2024. URL: https://www.ambient-iot.org/.

[4] Analog Devices. *LTC3588-1 Piezoelectric Energy Harvesting Power Supply Datasheet*. https://www.analog.com/media/en/technical-documentation/data-sheets/35881fc.pdf. Accessed: 2025-03-25. 2023.

[5] ANYSOLAR Ltd. *KXOB141K06F-TR Monocrystalline Solar Cell (184.3 mW, 4.15 V)*. https://www.digikey.com/en/products/detail/anysolar-ltd/KXOB141K06F-TR/13999194. Accessed: 2025-08-21. 2025.

[6] C. A. Balanis. *Antenna Theory: Analysis and Design*. 4th. Wiley, 2016. ISBN: 978-1118642061. URL: https://ia800501.us.archive.org/30/items/AntennaTheoryAnalysisAndDesign/Antenna%20Theory%20Analysis%20and%20Design%203rd%20ed.pdf.

[7] Nagarjun Bhat et al. "ZenseTag: An RFID assisted Twin-Tag Single Antenna COTS Sensor Interface". In: *Proceedings of the 22nd ACM Conference on Embedded Networked Sensor Systems (SenSys '24)*. ACM, 2024, pp. 336–350. DOI: 10.1145/3666025.3699342. URL: https://dl.acm.org/doi/10.1145/3666025.3699342.

[8] Coherent Thermal Solutions. *TG12-4-01L Single-Stage Thermoelectric Generator Datasheet*. https://www.coherent.com/resources/datasheet/materials/single-stage-thermoelectric-generator-tg12-4-ds.pdf. Accessed: 2025-02-11. 2020.

[9] Digikey (Mouser) Technology. *GM300-126-11-12-C TEG Datasheet*. https://mm.digikey.com/Volume0/opasdata/d220001/medias/docus/3769/GM300-126-11-12-C.pdf. Accessed: 2025-02-11. 2021.

[10] e-peas S.A. *AEM10941 Ultra-Low Power Energy Management IC Datasheet*. https://e-peas.com/documents/AEM10941/DS-AEM10941.pdf. Accessed: 2025-02-10. 2024.

[11] e-peas SA. *AEM30940 Quick Start Guide (QFN28, 2.45 GHz EVK1.3)*. https://e-peas.com/wp-content/uploads/quick-start-guides/qsg-aem30940_qfn28_2450mhz_evk1-3-v1-0.pdf. Accessed: 2025-02-11. 2022.

[12] e-peas SA. *AEM30940 User Guide (QFN28, 2.45 GHz EVK1.3)*. https://e-peas.com/wp-content/uploads/user-guides/ug-aem30940_qfn28_2450mhz_evk1-3-v1-0.pdf. Accessed: 2025-02-11. 2022.

[13] O. Gall, C. Meng, and H. Bhamra. "A batteryless energy harvesting storage system for implantable medical devices demonstrated in situ". In: *Circuits, Systems, and Signal Processing* 38.5 (2019), pp. 1360–1373. DOI: 10.1007/s00034-018-0963-2.

[14] Nakul Garg, Aritrik Ghosh, and Nirupam Roy. "LiTEfoot: Ultra-low-power Localization using Ambient Cellular Signals". In: *Proceedings of the 22nd ACM Conference on Embedded Networked Sensor Systems (SenSys '24)*. ACM, 2024, pp. 381–395. DOI: 10.1145/3666025.3699356. URL: https://dl.acm.org/doi/10.1145/3666025.3699356.

[15] Diogo Gonçalves, Miguel Roque Soares, and Waldir Moreira. "LIGHTED: a Multi-energy Harvesting Testbed". In: *Proceedings of the 12th International Workshop on Energy Harvesting & Energy-Neutral Sensing Systems (ENSsys '24)*. ACM, 2024, pp. 45–50. DOI: 10.1145/3698384.3699614. URL: https://dl.acm.org/doi/10.1145/3698384.3699614.

[16] M. A. Green. *Solar Cells: Operating Principles, Technology, and System Applications*. Prentice-Hall, 1982. ISBN: 978-0138222709. URL: https://pt.scribd.com/document/706552586/Martin-a-Green-Solar-Cells-Operating-Principles-Technology-and-System-Applications-Prentice-Hall-1982#content=query:Pout,pageNum:58,indexOnPage:0,bestMatch:false.

[17] J. Hester and J. Sorber. "The future of sensing is batteryless, intermittent, and awesome". In: *Proceedings of the 15th ACM Conference on Embedded Networked Sensor Systems* (2017), pp. 1–14. DOI: 10.1145/3131672.3131674.

[18] J. Hester, A. Tinka, and P. Beraldi. "Intermittent computing systems and fault tolerance in low-power devices". In: *ACM SIGPLAN Notices* (2020). Available: https://josiahhester.com/cv/files/tics-asplos20.pdf.

[19] J. Hester et al. "Batteryless task scheduling for intermittent computing systems". In: *ACM SIGPLAN Notices* (2020). Available: https://josiahhester.com/cv/files/btks-asplos20.pdf.

[20] Robert Huntley. "Energy Harvesting Set to Accelerate IoT and IIoT Use Cases". In: *Mouser Electronics* (2025). Accessed: 2025-08-30.

[21] InPlay Inc. *IN100 NanoBeacon Ultra-Low-Power BLE Module Datasheet*. https://cdn.sparkfun.com/assets/3/d/5/5/1/IN100-Datasheet.pdf. Accessed: 2025-04-22. 2021.

[22] Jun-Yi Liu and Yu-Pei Liang. "Selective Data Protection for Energy-Efficient Deep Neural Network Inference in Intermittent IoT Systems". In: *Proceedings of the 12th International Workshop on Energy Harvesting & Energy-Neutral Sensing Systems (ENSsys '24)*. ACM, 2024, pp. 13–18. DOI: 10.1145/3698384.3699610. URL: https://dl.acm.org/doi/10.1145/3698384.3699610.

[23] Mouser Electronics. *ENS210 Environmental Sensor Datasheet*. https://www.mouser.com/datasheet/2/1081/ENS210-1984006.pdf. Accessed: 2025-04-21. 2021.

[24] NanoBeacon Tool Contributors. *NanoBeacon Configuration Files Repository*. https://github.com/NanoBeacon/config-files. Accessed: 2025-04-22. 2025.

[25] Nessie Circuits. *Riotee Modular Harvesting Node Schematics*. https://www.riotee.nessie-circuits.de/artifacts/module/latest/schematics.pdf. Accessed: 2025-03-19. 2023.

[26] Nessie Circuits. *Riotee SDK on GitHub*. https://github.com/NessieCircuits/Riotee_SDK. Accessed: 2025-03-19. 2023.

[27] Nordic Semiconductor. *nRF52840 Dongle Datasheet (PCA10059)*. https://www.farnell.com/datasheets/2624112.pdf. Accessed: 2025-06-05. 2018.

[28] B. Parida, S. Iniyan, and R. Goic. "A Review of Solar Photovoltaic Technologies". In: *Renewable and Sustainable Energy Reviews* 15.3 (2011), pp. 1625–1636. DOI: 10.1016/j.rser.2010.11.032. URL: https://doi.org/10.1016/j.rser.2010.11.032.

[29] Powercast Corporation. *P2110B RF Energy Harvester Datasheet*. https://www.powercastco.com/wp-content/uploads/2021/07/P2110B-Datasheet.pdf. Accessed: 2025-02-11. 2021.

[30] PowerFilm Solar. *LL200-2.4-75 Indoor Light Series Solar Panel Datasheet*. https://www.powerfilmsolar.com/products/electronic-component-solar-panels/indoor-light-series/ll200-24-75. Accessed: 2025-03-18. 2023.

[31] S. Priya and D. J. Inman. *Energy Harvesting Technologies*. Springer, 2009. ISBN: 978-0387764641. URL: https://download.e-bookshelf.de/download/0000/0023/79/L-G-0000002379-0002340530.pdf.

[32] Rohm Semiconductor. *BH1750FVI Light Sensor Datasheet*. https://www.yujiintl.co.jp/storage/ele/Rohm/BH1750FVI-e.pdf. Accessed: 2025-03-27. 2016.

[33] Veronica Rovelli, Andrea Maioli, and Luca Mottola. "EXTREMIS: Static Frequency Switching for Battery-less Devices". In: *Proceedings of the 12th International Workshop on Energy Harvesting & Energy-Neutral Sensing Systems (ENSsys '24)*. ACM, 2024, pp. 26–31. DOI: 10.1145/3698384.3699616. URL: https://dl.acm.org/doi/10.1145/3698384.3699616.

[34] D. M. Rowe. *CRC Handbook of Thermoelectrics*. CRC Press, 1995. ISBN: 978-0849301469. URL: https://api.pageplace.de/preview/DT0400.9780429956676_A38597256/preview-9780429956676_A38597256.pdf.

[35] Sensirion AG. *SHT4x - Humidity and Temperature Sensor Datasheet*. https://sensirion.com/media/documents/33FD6951/67EB9032/HT_DS_Datasheet_SHT4x_5.pdf. Accessed: 2025-04-21. 2022.

[36] Sensirion AG. *SHTC3 Humidity and Temperature Sensor Datasheet*. https://sensirion.com/media/documents/643F9C8E/63A5A436/Datasheet_SHTC3.pdf. Accessed: 2025-02-18. 2021.

[37] Sitong Shen, Wenbo Ding, and Chenshu Wu. "Self-Powered Visible Light Communication for Batteryless IoT via Vibration Energy Harvesting". In: *Proceedings of the 12th International Workshop on Energy Harvesting & Energy-Neutral Sensing Systems (ENSsys '24)*. ACM, 2024, pp. 19–25. DOI: 10.1145/3698384.3699611. URL: https://dl.acm.org/doi/10.1145/3698384.3699611.

[38] Weining Song et al. "TaDA: Task Decoupling Architecture for the Battery-less Internet of Things". In: *Proceedings of the 22nd ACM Conference on Embedded Networked Sensor Systems (SenSys '24)*. ACM, 2024, pp. 409–421. DOI: 10.1145/3666025.3699347. URL: https://dl.acm.org/doi/10.1145/3666025.3699347.

[39] SparkFun Electronics. *IN100 NanoBeacon Ultra-Low-Power BLE Module Datasheet*. https://cdn.sparkfun.com/assets/3/d/5/5/1/IN100-Datasheet.pdf. Accessed: 2025-04-22. 2024.

[40] Texas Instruments. *HDC2080 Digital Humidity and Temperature Sensor Datasheet*. https://www.ti.com/lit/ds/symlink/hdc2080.pdf. Accessed: 2025-04-21. 2020.

[41] Texas Instruments. *TPL5110 Nano Timer Datasheet*. https://www.ti.com/lit/ds/symlink/tpl5110.pdf. Accessed: 2025-04-03. 2020.

[42] Texas Instruments. *TPL5111 NanoTimer Datasheet*. https://www.ti.com/lit/ds/symlink/tpl5111.pdf. Accessed: 2025-04-03. 2021.

[43] United Nations. *The Sustainable Development Goals*. https://sdgs.un.org/goals. Accessed: 2024-12-26. 2015.

[44] C. R. Valenta and G. D. Durgin. "Harvesting Wireless Power: Survey of Energy-Harvester Conversion Efficiency in Far-Field Wireless Power Transfer Systems". In: *IEEE Microwave Magazine* 15.4 (2014), pp. 108–120. DOI: 10.1109/MMM.2014.2309499. URL: https://www.researchgate.net/publication/262150645_Harvesting_Wireless_Power_Survey_of_Energy-Harvester_Conversion_Efficiency_in_Far-Field_Wireless_Power_Transfer_Systems.

[45] Harrison Williams and Matthew Hicks. "A Survey of Prototyping Platforms for Intermittent Computing Research". In: *Proceedings of the 12th International Workshop on Energy Harvesting & Energy-Neutral Sensing Systems (ENSsys '24)*. ACM, 2024, pp. 7–12. DOI: 10.1145/3698384.3699612. URL: https://dl.acm.org/doi/10.1145/3698384.3699612.

[46] Chenyang Wu et al. "Attendance Tracking System using Many Battery-free Photovoltaic Bluetooth Beacon Badges". In: *Proceedings of the 12th International Workshop on Energy Harvesting & Energy-Neutral Sensing Systems (ENSsys '24)*. ACM, 2024, pp. 1–6. DOI: 10.1145/3698384.3699609. URL: https://dl.acm.org/doi/10.1145/3698384.3699609.

[47] Yijia Yang et al. "A Resilient ReRAM Crossbar-based PIM Design for SNN in Energy Harvesting Scenarios". In: *Proceedings of the 12th International Workshop on Energy Harvesting & Energy-Neutral Sensing Systems (ENSsys '24)*. ACM, 2024, pp. 32–38. DOI: 10.1145/3698384.3699615. URL: https://dl.acm.org/doi/10.1145/3698384.3699615.

[48] Eren Yildiz, Davide Cavedon, and Kasim Sinan Yildirim. "On Tracking Time with Better Resolution and Range in Batteryless Systems". In: *Proceedings of the 12th International Workshop on Energy Harvesting & Energy-Neutral Sensing Systems (ENSsys '24)*. ACM, 2024, pp. 39–44. DOI: 10.1145/3698384.3699613. URL: https://dl.acm.org/doi/10.1145/3698384.3699613.